ELECTROCHEMICAL AND MOLECULAR MODELLING STUDIES TO ASSESS THE PHOTOREACTIVE PROPERTIES OF EFAVIRENZ

By

Thethiwe Promise Mthiyane

Student number: 21007867

Submitted in fulfilment of the requirements of the degree of Master of Applied Science in Chemistry in the Faculty of Applied Sciences at the Durban University of Technology

July 2022

DECLARATION

I THETHIWE PROMISE MTHIYANE declare that the work submitted on "Electrochemical and molecular modelling studies to assess the photoreactive properties of efavirenz" is my own work which has never been represented before to any other university.

Student name: Thethiwe Promise Mthiyane

Student signature **Date:** 23/06/22.....

Supervisor: Professor K. Bisetty

Supervisor signature: **Date:** 23/06/22.....

Co-Supervisor: Dr M. A Jordaan

Co-Supervisor signature: **Date:** 23/06/22.....

Co-Supervisor: Dr G. E Uwaya

Co-Supervisor signature: **Date:** 23/06/22.....

ACKNOWLEDGEMENTS

*Words can never be enough to express my gratitude to what the **LORD JESUS CHRIST** has done for me throughout this difficult and challenging journey; thank you LORD for your comfort, wisdom, favour and mercy for me to go through this important milestone of my academic career.*

*I would like to extend my gratitude to my supervisor **Professor K. Bisetty,** from the Department of Chemistry at Durban University of Technology for his prudent guidance, patience, encouragement throughout the course of my study. Thank you so much Prof for your availability, consistence advice and for making sure that I complete this study. Thank you for guiding me as daughter.*

*I would like to extend my other gratitude to my co-supervisor **Dr M. A Jordaan** from Mangosuthu University of Technology; thank you so much for your support throughout. I would like to thank my sister, **Dr G. E**. **Uwaya,** Postdoctoral Fellow from the Department of Chemistry at Durban University of Technology for her support from all angles of this study, right from the beginning until the end. Her support was not only academic but also spiritually thank you. I would like to give thanks to my colleagues **Lyndon** and **Benni** for their friendship and support within the course of my study thank you, guys. I would also like to extend my gratitude to the laboratory staff; especially Mrs **Mavis Xhakaza** from Department of Chemistry at Durban University of Technology; **Ayanda** and **Aneswa** for their assistance and advice throughout the course of my journey. Thank you*

*I would like to give a BIG thank to my family, they have been very supportive emotionally and financially. To my father **Beatus** and **Nomusa Mthiyane** thank you mom and dad for everything. This also goes to my brothers (**Thokozani, Moki, Lindani and Sbusiso Mthiyane**) and my sisters (**Nomvula, Thuliswa** and **Busi Mthiyane**) thank you for your support throughoutt; to my life group members (Pastor **Khosi** Nyawo at DCC**; MMdeni; Mmbusi; Oneil; Bennita; Chumi** and many more) thank you for your spiritual support. My greatest gratitude also goes out to my friends (**Dudu; Sne; Tholi, Michael**) thank you guys for your support and advice.*

I would also like to thank Prof S Singh, Executive Dean FAS at DUT for financial support.

ABSTRACT

Efavirenz (EFV) is commonly used as an antiretroviral drug to treat HIV/AIDS and is known to undergo photoreactions that could be exploited for photodegradation applications. In addition, there is limited information on the photoreactivity of EFV. This work focuses on two case studies to assess the photocatalytic properties of EFV supported by experimental and molecular modelling (commonly referred to as computational chemistry).

The first case study deals with the design of an innovative electrochemical sensor for the detection of EFV, using titanium dioxide nanoparticles (TiO_2-NPs) doped on glassy carbon electrode (GCE) with nafion as an anchor agent (GCE/TiO_2-NPs-nafion). TiO_2-NPs were synthesized using *Eucalyptus globulus* leaf extract and characterized using Fourier transform infrared spectroscopy (FTIR), ultraviolet-visible spectroscopy (UV-vis), scanning electron microscopy (SEM), transmission electron microscopy (TEM), X-ray diffraction (XRD), and energy-dispersive spectroscopy (EDS). The electrochemical and sensing properties of the developed sensor for EFV were assessed using cyclic voltammetry (CV), electrochemical impedance spectroscopy (EIS), differential pulse voltammetry (DPV) and chronoamperometry. The oxidation peak current response for EFV on the GCE/TiO_2-NPs-nafion electrode was greater compared to the bare and modified GCE/TiO_2-NPs electrodes. A linear dynamic range of 4.5 to 18.7 µM with a 0.01 µM limit of detection was recorded on the electrode using DPV. The electrochemical sensor demonstrated good selectivity as well as practicability for the detection of EFV drugs with excellent recoveries ranging from 92.0-103.9%. The density functional theory (DFT)-based quantum chemical modelling was used to establish the chemical reactivity for EFV, suggesting the benzoxazine ring as the active site. Monte Carlo (MC) simulations revealed a strong electrostatic interaction on the GCE/TiO_2-NPs-nafion-EFV (substrate-adsorbate) system. The results showed good agreement between the MC computed adsorption energies and the experimental CV results for EFV. The stronger adsorption energy of nafion onto the GCE/TiO_2-NPs substrate contributed to the catalytic role in the signal amplification sensing of EFV.

The second case study deals with the assessment of the photocatalytic degradation of EFV in combination with green synthesized TiO_2-NPs. The photocatalytic activity of TiO_2-NPs was examined by the degradation of EFV in an aqueous medium and a maximum degradation efficiency of 91.77% was observed at a reaction time of 5 h. In addition, the electronic spectra

of the EFV complex bound to single TiO_2-NPs in a gas- and solution-phase were investigated using time-dependent density functional theory (TD-DFT) calculations. The calculated spectra obtained in this work were benchmarked against the gas-phase photodecomposition of the EFV- TiO_2-NPs complex using UV-vis spectrophotometry.

Overall, the results show that the biosynthesized TiO_2-NPs have the potential for sensing pharmaceutical applications and their degradation. The results provide an effective way to explore the design of new 2D materials for the sensing of EFV, which is highly significant in the field of medicinal and materials chemistry.

Keywords: Electrochemical sensor, photodegradation, Efavirenz, Titanium dioxide, Monte Carlo, density functional theory

PUBLICATIONS UNDER REVIEW

Khethiwe Mthiyane, Gloria. Ebube. Uwaya, Maryam Amra Jordaan, Suvardhan Kanchi and Krishna Bisetty. “Insights into the design of an enzyme free sustainable sensing platform for efavirenz”. *Catalysts* **2022**. Under Review: Submitted 17 June 2022.

Table of Contents

DECLARATION ..... **i**

ACKNOWLEDGEMENTS ..... **ii**

ABSTRACT ..... **iii**

PUBLICATIONS UNDER REVIEW ..... **v**

LIST OF FIGURES ..... **ix**

LIST OF TABLES ..... **xii**

LIST OF ABBREVIATIONS ..... **xiii**

CHAPTER ONE: INTRODUCTION **1**

1.1 EFAVIRENZ AS ANTIRETROVIRAL DRUG **1**

1.2 PROBLEM STATEMENT **3**

1.3 AIM AND OBJECTIVES **4**

1.3.1 Aim **4**

1.3.2 Objectives **4**

1.4 THESIS OUTLINES **5**

CHAPTER TWO: LITERATURE REVIEW **6**

2.1 EFAVIRENZ **6**

2.2 METHODS OF DETECTION FOR EFV **7**

2.2.1 Chromatographic and spectroscopic methods **7**

2.2.2 Electrochemical methods **7**

2.3 ELECTROCHEMICAL SENSORS **8**

2.4 NANOMATERIALS **10**

2.4.1 Classification of nanomaterials **11**

2.4.2 Application of nanomaterials **11**

2.4.3 titanium dioxide nanoparticles (TiO_2-NPs) **12**

2.4.4 Nafion **15**

2.5 SYNTHESIS OF NANOPARTICLES 17

2.5.1 Chemical synthesis methods 17

2.5.2 Biological synthesis method 20

CHAPTER THREE: THEORETICAL PRINCIPLES 23

3.1 EXPERIMENTAL CHARACTERISATION TECHNIQUES 23

3.1.1 Fourier transform infrared (FTIR) 23

3.1.2 UV- Visible (UV-vis) spectrophotometry 24

3.1.3 Transmission emission microscopy (TEM) 25

3.1.4 Scanning electron microscopy (SEM) 25

3.1.5 Energy-dispersive x-ray spectroscopy 25

3.1.6 X-ray diffraction (XRD) 26

3.1.7 Cyclic voltammetry (CV) 27

3.1.8 Differential pulse voltammetry (DPV) 28

3.1.9 Electrochemical impedance spectroscopy (EIS) 29

3.1.10 Chronoamperometry 30

3.2 COMPUTATIONAL CHEMISTRY 31

3.2.1 Density Functional Theory Methods (DFT) 32

3.2.2 Time Dependent Density Functional Theory (TD-DFT) 34

3.2.3 Monte Carlo (MC) simulations 34

CHAPTER FOUR: MATERIALS AND METHODS 36

4.1 EXPERIMENTAL SECTION 36

4.1.1 Materials and methods 36

4.1.2 Instrumentation 36

4.1.3 Preparation of plant extract 36

4.1.4 Synthesis of titanium (IV) oxide nanoparticles 37

4.1.5 Electrode pre-treatment and modification 37

4.1.6 Preparation of electrolyte solution 38

4.1.7 Preparation of EFV stock solution and sub-solution **38**

4.1.8 Real sample preparation and analysis **39**

4.1.9 Characterization of TiO_2-NPs **39**

4.1.10 Electrochemical studies **39**

4.1.11 Electrochemical properties of EFV **39**

4.1.12 photodegradation of EFV **40**

4.2 COMPUTATIONAL SECTION **40**

4.2.1 Model building **40**

4.2.2 Density functional theory (DFT) calculations **40**

4.2.3 Monte Carlo (MC) simulations **41**

CHAPTER FIVE: RESULTS AND DISCUSSION **42**

5.1 CASE STUDY I **42**

DESIGN OF A SENSING PLATFORM FOR EFAVIRENZ **42**

5.1.1 Experimental section **42**

5.1.2 Computational section **57**

5.1.3 Conclusion **61**

5.2 CASE STUDY II **62**

THE PHOTOCATALYTIC DEGRADATION OF EFV **62**

5.2.1 Experimental section **62**

5.2.2 Computational section **66**

5.2.3 Conclusion **73**

CHAPTER SIX: CONCLUDING REMARKS AND RECOMMENDATIONS **74**

6.1 CONCLUDING REMARKS **74**

6.2 RECOMMENDATIONS FOR FUTURE WORK **75**

REFERENCES **76**

LIST OF FIGURES

Figure 2.1: 3D structure of efavirenz drawn using materials Studio (Biovia 2016) 6

Figure 2.2: Schematic illustration of an electrochemical sensor set-up (Nnamchi and Obayi 2018; Lalmalsawmi, Tiwari and Kim 2020) 9

Figure 2.3: Type of nanomaterial (0D, 1D, 2D and 3D) (Ali 2020) 11

Figure 2.4: 3D representation of the polymorphs of TiO_2-NPs (a) anatase (b) rutile and (c) brookite (Biovia 2016). 13

Figure 3.1: Schematic illustration of a modern FTIR spectrophotometer (Rauch et al. 2021) 23

Figure 3.2: Schematic illustration of UV-visible spectroscopy 24

Figure 3.3: Schematic illustration of the X-ray diffractometer 26

Figure 3.4: Typical CV showing important peak parameter 27

Figure 3.5: Typical CV for reversible, quasi-reversible and irreversible voltammogram. 28

Figure 3.6: Typical Differential pulse voltammogram 29

Figure 3.7: Typical staircase (Vilasó-Cadre *et al.* 2020) 29

Figure 3.8: Shows a simple Randle's equivalent circuit for an electrochemical cell (Randviir and Banks 2013) 30

Figure 3.9: Chronoamperometry output signal (Lee 2014) 31

Figure 3.10: Step-by-step diagram of MC simulations 35

Figure 4.1: Synthesis of titanium (IV) oxide nanoparticles 37

Figure 5.1: FTIR spectra for green synthesized TiO_2-NPs 42

Figure 5.2: UV–vis spectra of (A) Extract and (B) TiO_2-NPs 43

Figure 5.3: SEM image of green synthesized TiO_2-NPs 44

Figure 5.4: XRD pattern of green synthesized TiO_2-NPs 45

Figure 5.5: EDS image of green synthesized TiO_2-NPs 45

Figure 5.6: TEM image for green synthesized TiO_2-NPs 46

Figure 5.7: CVs obtained in (A) 0.1 M PBS and (B) in 0.1 M PBS at pH 7 containing 5 mM of $[Fe(CN)_6]^{3-/4-}$ at 25 mV/s scan rate 47

Figure 5.8: (A) Nyquist plots in 5 mM redox probe at the unmodified and modified electrodes, (B) Electrical equivalent circuit for the electrodes ([R(Q[RW)]). 48

Figure 5.9: (A) Cyclic voltammograms in 5 mM [Fe $(CN)_6]^{3-/4-}$ solution at various scan rate (25–200 mV/s) on GCE/TiO_2-NPs-nafion electrode. linear plots of (B) *I*p versus $v^{1/2}$ (C) log Ip versus log v (D) Ip versus scan rate versus and (E) Ep versus log of v. 50

Figure 5.10: (A) Cyclic voltammograms in 0.1 M PBS at pH ranging from 5 – 8.5 containing 47.6 µM EFV and (B) in PBS only on at GCE/TiO_2-NPs-nafion at 25 mV/s 51

Figure 5.11: Cyclic voltammograms at 25 mV/s obtained at the bare and modified GCEs in 0.1 M PBS at pH 7 containing 47.6 µM EFV 52

Figure 5.12: (A) Nyquist plots obtained at the bare and modified GCEs in 0.1 M PBS at pH 7 containing 47.6 µM EFV. (B) is the equivalent circuit-[R(RQ)] for the electrodes. 53

Figure 5.13: (A) GCE/TiO_2-NPs-nafion response to increasing EFV concentrations measured by DPV. (B) Linear plot of Ipa against concentrations (4.54 – 18.7 µM) in PBS. 54

Figure 5.14: (A) The simultaneous determination of 47.6 µM EFV, AA and UA on GCE/TiO_2-NPs-nafion by DPV, (B) Chronoamperometric curve of GCE/TiO_2-NPs-nafion in pH 7 PBS containing EFV, AA and UA 56

Figure 5.15: The repeatability of GCE/TiO_2-NPs-nafion towards 47.6 µM EFV 57

Figure 5.16: Frontier molecular orbitals on optimized molecular structure of EFV computed at B3LYP/6-311+G 58

Figure 5.17: System conformations for (A) GCE/TiO_2-NPs-EFV and (B) GCE/TiO_2-NPs-nafion-EFV together with their respective distribution field maps (C) and (D) in a periodic cell 60

Figure 5.18: UV–vis spectra of (A) TiO_2-NPs (B) EFV in methanol 62

Figure 5.19: Tauc's plot for EFV, TiO_2-NPs and EFV-TiO_2-NPs 64

Figure 5.20: (A) UV–vis spectra interaction of EFV-TiO_2-NPs and (B) degradation efficiency of EFV-TiO_2-NPs. 65

Figure 5.21: Calculated TD-DFT UV Spectra (A) and (B) DOS for EFV in gas phase; Calculated TD-DFT UV Spectra (C) and (D) DOS for EFV in methanol 66

Figure 5.22: Calculated TD-DFT UV Spectra (A) and (B) DOS for EFV-TiO_2-NPs in gas phase; Calculated TD-DFT UV Spectra (C) and (D) DOS for EFV-TiO_2-NPs in methanol 67

Figure 5.23: The geometry optimized EFV-TiO_2-NPs computed at B3LYP/6-31+G* level of theory (red, green, dark blue, pale blue, white, and grey, denotes the oxygen, chlorine, nitrogen, fluorine, hydrogen and carbon respectively). 68

Figure 5.24: The atomic orbital compositions of the frontier molecular of the Interaction of EFV and TiO_2-NPs at B3LYP/6-31+G* level of theory 69

Figure 5.25: Calculated UV spectra for (A) EFV and (B) EFV-TiO_2-NPs in methanol using TD-DFT/B3LYP/6-31G* basis set. The inset shows the HOMO-LUMO plots at the calculated wavelengths. 70

Figure 5.26: Calculated Density of States (DOS) for (A) EFV and (B) EFV-TiO_2-NPs in methanol using TD-DFT/B3LYP/6-31G* basis set. 72

LIST OF TABLES

Table 2.1: TiO_2-NPs based sensors summarize 14

Table 2.2: Application of nafion in electrochemical sensors 16

Table 2.3: Application of non-nafion electrochemical sensors 16

Table 2.4: Different methods or plants used for the synthesis of TiO_2-NPs 20

Table 5.1: Summary of CV parameters recorded for the bare and modified electrodes in 5 mM Fe $(CN)_6]^{3-/4-}$ 47

Table 5.2: EIS data obtained on different electrodes in 5 mM [Fe $(CN)_6]^{3-/4-}$ solution at +0.2 V fixed potential. 49

Table 5.3: Impedance data obtained for electrodes in 47.6 µM EFV at a fixed potential of 1.2 V (vs Ag/AgCl, standard KCl). Results are represented in parenthesis percentage errors of the data fitting. 53

Table 5.4: Comparison with other sensors 55

Table 5.5: Recovery and RSD of EFV on GCE/TiO_2-NPs-nafion in Cipla EFV sample 55

Table 5.6: Calculated adsorption energy for the adsorbate-substrate systems 59

Table 5.7: Calculated adsorption wavelengths for (a) EFV gas; (c) EFV methanol using TD-DFT/B3LYP/6-31G* basis set 73

Table 5.8: Calculated adsorption wavelengths for (a) EFV-TiO_2-NPs gas; (c) EFV-TiO_2-NPs methanol using TD-DFT/B3LYP/6-31G* basis set 73

LIST OF ABBREVIATIONS

ARV	Antiretroviral
AIDs	Immunodeficiency
B3LYP	Becke-3-parameter exchange-correlation functional; LEE; Yang, and Parr
CV	Cyclic voltammetry
CE	Counter electrode
DPV	Differential pulse voltammetry
DTF	Density functional theory
EFV	Efavirenz
EIS	Electrochemical impedance spectroscopy
EDS	Energy – dispersive spectroscopy
FTIR	Fourier transform infrared
NVP	Nevirapine
NMs	Nanomaterials
NPs	Nanoparticles
WE	Working electrode
RE	Reference electrode
LOD	Limit of detection
SEM	Scanning electron microscope
XRD	X-ray diffraction
WHO	World health organization
TEM	Transmission emission microscopy
TD-DFT	Time dependent Density functional theory
MC	Monte Carlo simulations

CHAPTER ONE: INTRODUCTION

This chapter presents a brief overview of antiretroviral (ARV) drugs with emphasis on the pharmaceutical compound, efavirenz (EFV) used in drug monitoring. This is followed by the aims, objectives, and thesis outline.

1.1 EFAVIRENZ AS ANTIRETROVIRAL DRUG

Antiretroviral (ARV) drugs are essential for the treatment of acquired immunodeficiency syndrome known as (AIDs) (Eggleton and Nagalli 2020). In 2020, public health reported that 33 million people have been affected by HIV-AIDs (Simon *et al.* 2020). Antiretroviral drugs used against viral infections caused by HIV-AIDs and hepatitis are still in demand for drug monitoring. Efavirenz (EFV) is of great importance among ARVs due to its therapeutic properties and contemporary use in the fight against AIDs and hepatitis in combination with other anti-HIV-AIDs products (Tittikpina *et al.* 2020).

EFV is a cost-effective option for first-line antiretroviral therapy (ART) (Masenga *et al.* 2021) that plays a crucial role in HIV treatment strategies (Tittikpina *et al.* 2020). EFV has been shown in a recent study to be cytotoxic against cancer cells, with the potential to be repurposed as an anticancer agent (Hecht *et al.* 2013). The combination of EFV with other drugs of abuse for recreational purposes triggers toxicity (Thapliyal *et al.* 2015). EFV is also known to undergo photoreactions that could be exploited for use in photocatalytic degradation. For instance, a validation method using HPLC, and UV light was developed for the determination of degraded substance in efavirenz. The results were observed between 320 nm and 400 nm (Hamrapurkar *et al.* 2010). In addition pH rate profile and degradation kinetics of efavirenz and identification of hydrolysis product were developed using liquid chromatography photo diode array-mass spectrometry (LC-PDA-MS) for bulk sample of efavirenz (Gadkari *et al.* 2010). However, there is limited information on the photocatalytic reactivity of EFV. Therefore, the development of a reliable and cost-effective analytical tool for qualitative and quantitative measurement of EFV in pharmaceutical products with a fast response time is crucial. Currently, various analytical assays including chromatographic (Dogan-Topal, Ozkan and Uslu 2007; Lakshmi Sailaja *et al.* 2007; Notari *et al.* 2008; Martin *et al.* 2009; Kim *et al.* 2011; Srivastava *et al.* 2013; Tamilselvi *et al.* 2018; dos Santos Martins *et al.* 2019; Masenga

et al. 2021), spectrophotometric methods (Slabiak *et al.* 2018; Tittikpina *et al.* 2020), and electrophoresis (Zanolli Filho *et al.* 2011; Guichard *et al.* 2021) have expanded in the development of EFV. However, these techniques are costly, require long time for experimental measurements, sample pre-treatment, instrumentation optimisation, and skilled analysts (Thapliyal *et al.* 2015; Hareesha *et al.* 2021). These limitations can be overcome at least in part with the use of electrochemical assays. Electrochemical methods including voltammetry, impedance metrics have attracted the attention in the field of drug analysis due to their rapid detection, low cost, and high sensitivity without requiring tedious extraction or pre-treatment procedures. However, very few reports are available on the electrochemical methods for the analysis of the EFV on fabricated electrodes/sensors (Dogan-Topal, Uslu and Ozkan 2009; Castro *et al.* 2011; Thapliyal *et al.* 2015; Raj *et al.* 2017). Current trends in the application of electroanalytical chemistry for the detection and degradation of pharmaceuticals involve the use of nanostructured materials to modify the electrodes' surfaces, resulting in significant signal amplification, and enhancing the sensitivity, stability and selectivity of the synthesized sensors/biosensors. These enhancements are attributed to the critical role of the nanomaterials, which can create the effect of synchronization between the catalytic activity, electrical conductivity, and biocompatibility based on accelerating the signal transduction (Jeong *et al.* 2021).

Different Semiconducting metal oxides nanoparticles such as copper (II) oxide CuO, titanium dioxide (TiO_2), zinc oxide (ZnO), iron oxide (Fe_2O_3) and tungsten oxide (WO_3) have vast application in thin films transistors transparent electrode (Zaleska-Medynska 2018), gas sensitive layers of the sensors for industrial processes (Martins *et al.* 2018; Sharma and Sharma 2022). CuO have found application in sensing of glucose with acceptable stability and sensitivity owing to their precise surface area and good electrochemical activity (Asrami *et al.* 2018). ZnO possesses an interesting properties such as high electrical conductivity and chemical steadiness, and are cost effective (Shetti *et al.* 2019a). Fe_3O_4 is also an idea choice for semiconductor oxide that has been used for glucose oxidation (Shetti *et al.* 2019a). WO_3 are rarely used but a promising additive for (TiO_2-NPs) since its photochemical property with regards to visible light is reduced. (He *et al.* 2002). Some of the drawbacks are the need of high temperature for their operability (Yang *et al.* 2019b). In addition more understanding is required for cytotoxic effect and corresponding mechanisms for their safe application (Stankic *et al.* 2016). Among many semiconductors, titanium dioxide (TiO_2-NPs) turns out to be the

most attractive and promising semiconductor due to their unique properties. TiO_2-NPs are the most extensive metal oxide nanomaterials employed in the modification of electrodes because of their high surface area, thermal stability, low toxicity and a wide band gap (Oliveira and Morais 2018; Shetti et al. 2018; Tarahomi et al. 2018). TiO_2-NPs are also widely employed as photocatalysts due to their band gap energy which enhances the photocatalytic properties. The photocatalytic activity of TiO_2-NPs has been estimated by the degradation of organic pollutants (Chen *et al.* 2020), pesticides (Akbari Shorgoli and Shokri 2017) and heavy metals (Sethy et al. 2020). In addition, there is a growing application of computational modelling tools such as quantum mechanics and molecular mechanics or force field.

Density functional theory (DFT) is the most used method because it employs different functional types that involve exchange and correlation for either accessible or close shell. Moreover, it mainly helps us to calculate the electronic and vibrational properties, while Monte Carlo simulations provide a better understanding of molecular interactions of biomolecules with surfaces via atomic and molecular levels imitating experimental procedures. Unlike molecular dynamics simulations, Monte Carlo simulations do not need resolving the Newton's equation of motion. This allows for the generated trial configurations within statistical mechanics. Furthermore, Monte Carlo simulation are generally easily compared to other techniques. (Ramachandran, Deepa and Namboori 2008).

1.2 PROBLEM STATEMENT

Antiretroviral treatment is limited by the high cost and limitations that are accompanied by resources, which makes it difficult for patients to obtain treatment. Thus, drug monitoring is very important for the identification and prevention of the unnecessary switching to more expensive ARV regimens (Hugen *et al.* 2002). Furthermore, there is a need to combine antiretroviral drug monitoring methods that are sensitive and efficient for detection, which is an important treatment for HIV type 1. The current qualitative and quantitative analysis of EFV require long analysis time, purification steps and elaborate extraction, which are expensive and therefore limit their application in routine laboratories. Hence, it is imperative that alternative methods be investigated, based on the incorporation of nanomaterials, which provide a more user-friendly option with an improved signal amplification strategy. Additionally, despite the importance of EFV drugs, improper disposal of unused and expired EFV drugs can result in the contamination of the soil and aquatic environments. According to (Schoeman, Dlamini and Okonkwo 2017), ARV drugs including EFV and nevirapine (NVP) are emerging contaminants

which can be environmentally persistent due to their poor solubility in water. Thus, posing a potential risk to human health. Exposure to EFV can result in neuropsychiatric disorders (Nwogu *et al.* 2021) depending on the source, dose and length of exposure. Therefore, monitoring the stability of EFV residues in water is imperative. Previous studies have reported an increase in nanomaterials usage for many social, economic and industrial benefits (Maurer-Jones *et al.* 2013). Currently, researchers such as (Wu *et al.* 2019; Zhu *et al.* 2019) reported that nanomaterials are effective and are of utmost importance to science and technology.

Hence, this study focuses on the design of a novel electrochemical sensor for the detection of EFV and to study its photodegradation properties based on the interaction of EFV with TiO_2-NPs in aqueous media supported by computational methods. The electrochemical behaviour of EFV on the fabricated electrode was studied using CV for qualitative purposes, EIS used to probe the interfacial properties of the fabricated electrode and DPV for quantitative analysis.

1.3 AIM AND OBJECTIVES

1.3.1 AIM

The aim of this study is to develop a cost-effective electrochemical sensor for the detection of EFV and to evaluate its photocatalytic degradation under UV radiation using TiO_2-NPs supported by computational modelling.

1.3.2 OBJECTIVES

- To synthesize TiO_2-NPs using Eucalyptus *globulus* leaf extract and to characterize it using FTIR, UV-vis, XRD, SEM, EDS and TEM.
- To fabricate the electrochemical sensor using the synthesized TiO_2-NPs through modification of the working electrode with nafion as an anchor agent (GCE/ TiO_2-NPs-nafion).
- To measure the electrocatalytic performance of the fabricated electrodes towards EFV using CV, EIS and DPV.
- To study the photodegradation properties of EFV in combination with TiO_2-NPs under UV light.

- To perform computer experiments using MC simulations to predict the adsorption sites and to assess the intermolecular interactions of the fabricated electrode surfaces.

- To validate the spectroscopic properties obtained experimentally by TD-DFT calculations.

1.4 THESIS OUTLINES

Chapter 1 provides an overview of ARV drugs with emphasis on EFV in drug monitoring.

Chapter 2 discusses the literature review of EFV and an insightful understanding of previous analytical instruments used for the detection of EFV. Additionally, electrochemical applications in the detection of EFV are also discussed.

Chapter 3 outlines the theoretical principles used for both the experimental and computational procedures and provides a brief overview of the analytical instruments used followed by the theoretical principles associated with DFT calculations and MC simulations.

Chapter 4 describes the materials and methods used for the experimental and computational work used in this study.

Chapter 5 deals with the results obtained from the two case studies, based on the design and characterization of the electrochemical sensor and the photocatalytic effect of TiO_2-NPs on EFV.

Chapter 6 provides a summary, the conclusions and recommendations of this work

CHAPTER TWO: LITERATURE REVIEW

This chapter describes the literature review of efavirenz (EFV). This section further includes an insightful understanding of previous analytical instruments used as well as electrochemical detection applications for the detection of EFV.

2.1 EFAVIRENZ

Efavirenz is chemically described as (S)-6-chloro-4-(cyclopropylethynyl)-1,4-dihydro-4-(trifluoromethyl)-2H-3,1-benzoxazin-2-one with a molecular mass of 315.68 and empirical formula of $C_{14}H_9ClF_3NO_2$. The 3D structure of EFV is presented in Figure 2.1. EFV is a white to slightly pink crystalline powder, practically insoluble in water (<10 ug/ml), with a melting point ranging from 136-141 ^oC and a weak acid with pKa of 10.2 (Manns *et al.* 2005).

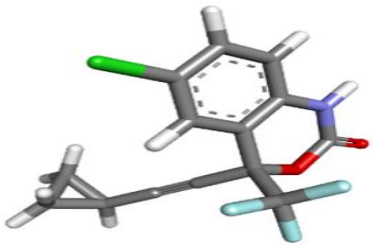

Figure 2.1: 3D structure of efavirenz drawn using materials Studio (Biovia 2016)

Efavirenz is one of the most recommended first-line antiretroviral combination therapies for the management of HIV in patients either infected with only HIV or co-infected with tuberculosis (Leary *et al.* 2013);(Rifkin-Graboi *et al.* 2013). Efavirenz provides a low risk of treatment and is available in small sizes. Recently, the world health organisation (WHO) recommended EFV as the preferred fine non-nucleoside reverse transcriptase inhibitor (NNRTIs), under the treatment of 2.0 initiative (Falzon *et al.* 2011; Organization 2019). Another review that analysed trial data comparing nevirapine (NVP) and EFV, concluded that EFV has a superior virological efficacy to NVP (Tang, Hull and Rothenberg 2012). In general, EFV appears to be better tolerated and has much less risk than NVP. Clinical evidence has shown EFV to be superior to NVP since it presents fewer adverse events and less risk of resistance (Turneaure *et al.* 2003).

2.2 METHODS OF DETECTION FOR EFV

2.2.1 CHROMATOGRAPHIC AND SPECTROSCOPIC METHODS

The current various analytical essays including chromatography (Dogan-Topal, Ozkan and Uslu 2007; Lakshmi Sailaja *et al.* 2007; Notari *et al.* 2008; Martin *et al.* 2009; Kim *et al.* 2011; Srivastava *et al.* 2013; Tamilselvi *et al.* 2018; dos Santos Martins *et al.* 2019; Masenga *et al.* 2021), spectrophotometry (Slabiak *et al.* 2018; Tittikpina *et al.* 2020), and electrophoresis (Zanolli Filho *et al.* 2011; Guichard *et al.* 2021) have been utilized for the detection of EFV. Chromatographic analysis has been used for the determination of efavirenz in human plasma, covering different phases of analytical research. However, it has limitations, such as being time-consuming during the separation of compounds with sophisticated processes, which results in high detection times (Ramachandran *et al.* 2006; More *et al.* 2013).

Capillary zone electrophoresis (CZE) is another powerful, economical and eco-friendly that has been used for the detection of EFV in tablets and human serum (Pereira, Micke and Tavares 2005) (Guichard *et al.* 2021). Nevertheless, CZE suffers from low sensitivity which provides real limitations (Guichard *et al.* 2021)**.**

The spectrophotometric is a conventional and inexpensive technique that has been used for the determination of efavirenz in plasma, however, it is less sensitive (Slabiak 2016; Tosin et al. 2016)

The limitations of the conventional assays (chromatographic, spectrophotometric and electrophoresis) could be resolved by introducing electrochemical methods as sensors.

2.2.2 ELECTROCHEMICAL METHODS

Electrochemical methods such as voltammetry (cyclic, square wave and differential pulse voltammetry) and potentiometry (electrochemical impedance spectroscopy) on chemical or biosensors have been prominently used in the field of drug analysis (Kaya *et al.* 2021) due to their rapid detection. However, very few reports are available on the electroanalytical methods for the analysis of the EFV (Dogan-Topal, Uslu and Ozkan 2009; Castro *et al.* 2011; Thapliyal *et al.* 2015; Raj *et al.* 2017) on fabricated electrodes (designed sensors).

Dogan-Topal et al. (2009) investigated the electrochemical behaviour using differential pulse voltammetry and quantified the EFV in commercial tablets at dsDNA modified disposable pencil graphite electrode. In another study, researchers (Aguiar Castro *et al.* 2011; Arnaldo Aguiar *et al.* 2011) developed a DPV procedure at the mercury film electrode to measure the concentration of EFV. Thapliyal and co-workers (2015), reported the nanocomposites of nickel oxide-zirconia ($NiO–ZrO_2$) synthesis and characterization using; TEM, SEM, EDS and XRD. GCE for the estimation of EFV, based on $NiO\text{-}ZrO_2$ using CV. The preparation of the nanoparticle-compounds of $NiO\text{-}ZrO_2$ was challenging and time-intensive and required high-energy mechanical milling for periods greater than 10 h. In addition, the nature of the $NiO\text{-}ZrO_2$ nanoparticles was also affected during milling. To overcome these challenges Raj and co-workers (2017), established a rapid one-pot synthesis method and the synthesized nanoparticles were used as an electrode modifier for the EFV sensor, with a detection limit similar to that reported by Thapliyal (2015). The analysis was carried out using electrochemical techniques to study the behaviour of EFV. The established work by Raj (2017) was based on an electrochemically reduced graphene oxide (ErGO) attached with platinum nanoparticles and nafion hybrid nanocomposite (ErGO-Pt-nafion) at the surface of edge plane pyrolytic graphite (EPPG). This experiment demonstrated significant electrocatalytic activity towards the oxidation of EFV at the developed sensor, and further revealed a linear relationship over the range of concentrations.

2.3 ELECTROCHEMICAL SENSORS

Electrochemical sensors detect information linked to the reaction between an electrolyte and an analyte (electrochemical reaction) into an applicable electric signal (qualitative and quantitative) corresponding to the concentration of the analyte using electrodes (Shetti *et al.* 2019b; Dhinakaran *et al.* 2020; Mustafa *et al.* 2021). The main component of electrochemical sensors are the transducer which is the working electrode (the reaction site of the sensor), and the chemical recognition element (receptor) (Shetti *et al.* 2019b; Mustafa *et al.* 2021). The transducer converts the energy into a discernible analytical signal and the receptor converts the chemical information into a form of energy (Madhura, Devi and Ramaraj 2021). Electrochemical sensors have the advantages of fast analysis, superior sensitivity and selectivity with simple instrumentation, (analysis with a small volume of sample) and low cost over conventional assays (Hussain and Keçili 2019; Madhura, Devi and Ramaraj 2021).

In a simple setup as presented in Figure 2.2 for the illustration of an electrochemical sensor which consists of a sensing or working electrode (WE), counter-electrode (CE), reference electrode (RE) in an electrochemical cell comprising an electrolyte, the potentiostat and the monitor (computer). The working electrode is the most important component of an electrochemical cell; it is used as a sensing electrode which senses the concentration of the analyte (Putra *et al.* 2019). The counter electrode which is also called an auxiliary electrode is considered to be an electrode which is used to enclose the current in the electrochemical cell (Zhang *et al.* 2014). Whilst the reference electrode provides a standard for electrochemical measurements, the potential of the reference electrode is not perturbed by the current being drawn from the cell which gives excellent control over the potential of the working electrode (Raccichini, Amores and Hinds 2019). The potentiostat drives the electrode, and the monitor which displays the electric signal.

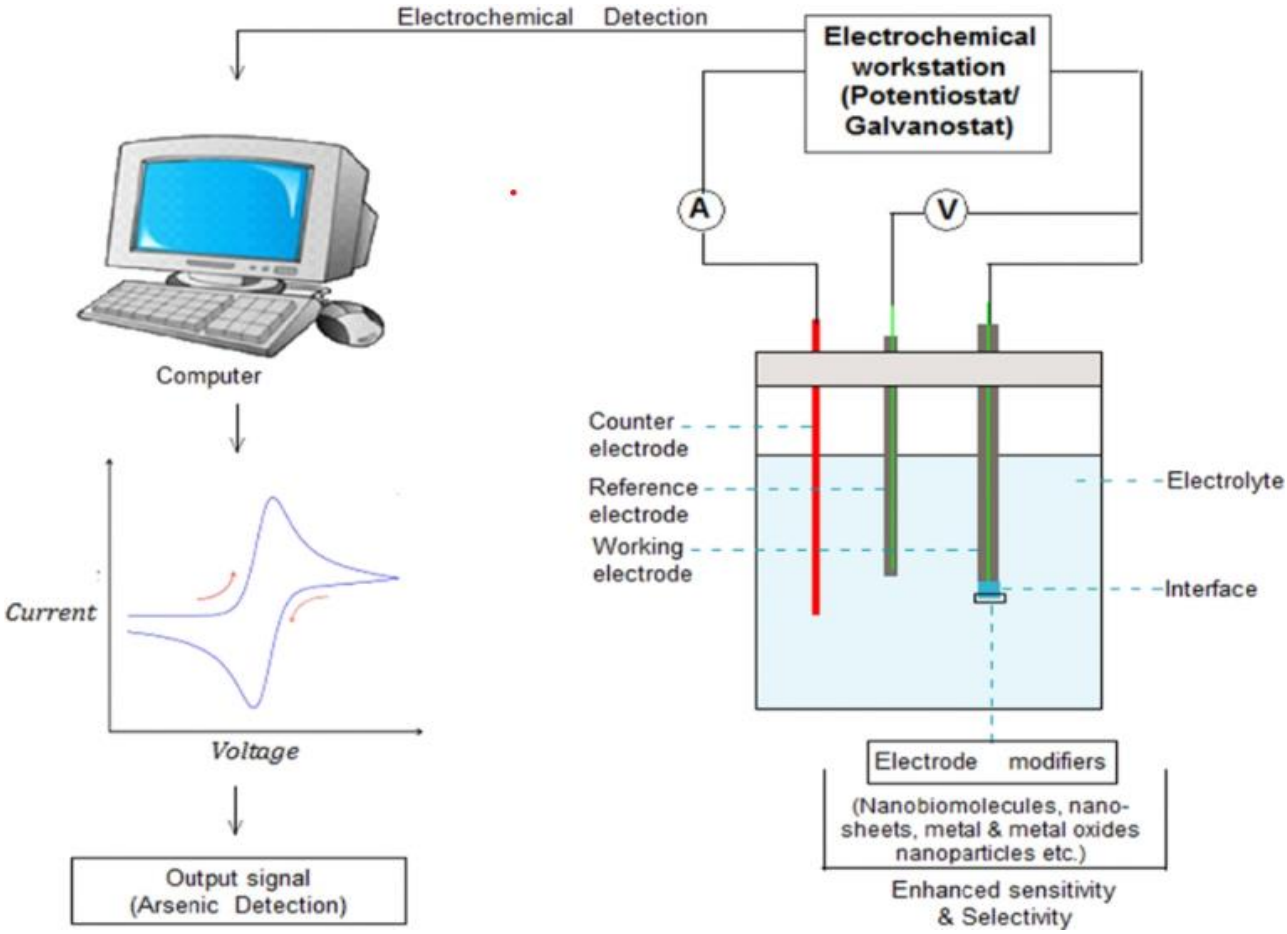

Figure 2.2: Schematic illustration of an electrochemical sensor set-up (Nnamchi and Obayi 2018; Lalmalsawmi, Tiwari and Kim 2020)

The behaviour of electrochemical sensors is enhanced by modification of the working electrode surface with nanomaterials such as metal nanoparticles, metal oxide nanoparticles and carbon-based materials, polymers, and metal-organic frameworks (Lalmalsawmi, Tiwari and Kim 2020; Milani and Sowwan 2020; Keçili and Denizli 2021; Xu 2021). These improvements are ascribed to the role of nanomaterials, which can produce the effect of synchronization between the catalytic activity, electrical conductivity, and biocompatibility based on accelerating the signal transduction (Jeong *et al.* 2021; Keçili and Denizli 2021).

2.4 NANOMATERIALS

Nanomaterials (NMs) are considered to be materials with at least one exterior dimension and an interior structure that measures one external dimension and an internal structure that measures between one to 100 nm (Yang *et al.* 2019a). Nanomaterials are grouped into different classes based on their attributes, shape or sizes. The application of nanomaterials ranges from electronic, medicine, sensors, fuel and solar cells to catalysts (Marzbani, Afrouzi and Omidvar 2015). There are different types of nanomaterials such as carbon-based, inorganic-based, organic-based or composite-based nanomaterials (Kanniyappan, SaravanaKumar and Muthukumaran 2017).

The most commonly used are carbon-based nanomaterials which contain carbon and are created from the laser ablation, arc, discharge and chemical vapour deposition method (Shende *et al.* 2021). Normally they occur as hollow tubes, ellipsoids and spheres which include fullerenes, carbon nanotubes, carbon black graphene and carbon ions (Kshetri *et al.* 2020).

Inorganic-based hybrid nanomaterials are composed of organic materials and inorganic materials; this nanomaterial is comprised of the metal and metal oxide nanoparticles, such as silver (Ag), iron oxide (Fe_3O_4), titanium dioxide (TiO_2-NPs), copper oxide (CuO), and zinc oxide (ZnO) (Długosz *et al.* 2021).

Organic-based nanomaterials are non-covalent with weak interactions for the patterns and designs of molecules, which serve to convert organic nanomaterials into desired structures such as lipids or polymeric, dendrimers, micelles, liposomes and polymers compounds (Jeevanandam *et al.* 2018).

Composite nanomaterials are based on multi-phase NPs where one phase is accompanied by a nanoscale dimension, which combines NPs with other NPs or combines NPs with enormous or

bulk type materials such as hybrid nanofibers or more complicated structures such as metal-organic frameworks (Jeevanandam *et al.* 2018). Normally the composite can be any combination of carbon-based NMs with any form of metal or organic-based NMs with any form of metal, ceramic, or polymer bulk materials.

2.4.1 CLASSIFICATION OF NANOMATERIALS

Nanomaterials can be categorised according to size, shape, composition and aggregation (Yadav, Mandal and Dubey 2020). Some nanomaterials can be zero dimension (0D), whereas the rest of the dimensions are measured within the nanoscale one dimension (1D), two dimension (2D) and three dimension (3D) as shown in Figure 2.3. The 1D and 2D are outside the nanoscale where, the 2D exhibits a plate-like shape, while the 3D materials are unrestrained to the nanoscale in any dimension. This can contain bulk powder dispersions of nanoparticles, bundles of nanowires and nanotubes as well as multi nanolayers (Tripathi 2019; Hu *et al.* 2021). The morphology of nanomaterials combines the characteristics of their size, shape and spinel structure, which could be classified as flat, spherical, hexagonal, irregular and helical (Cheng *et al.* 2020).

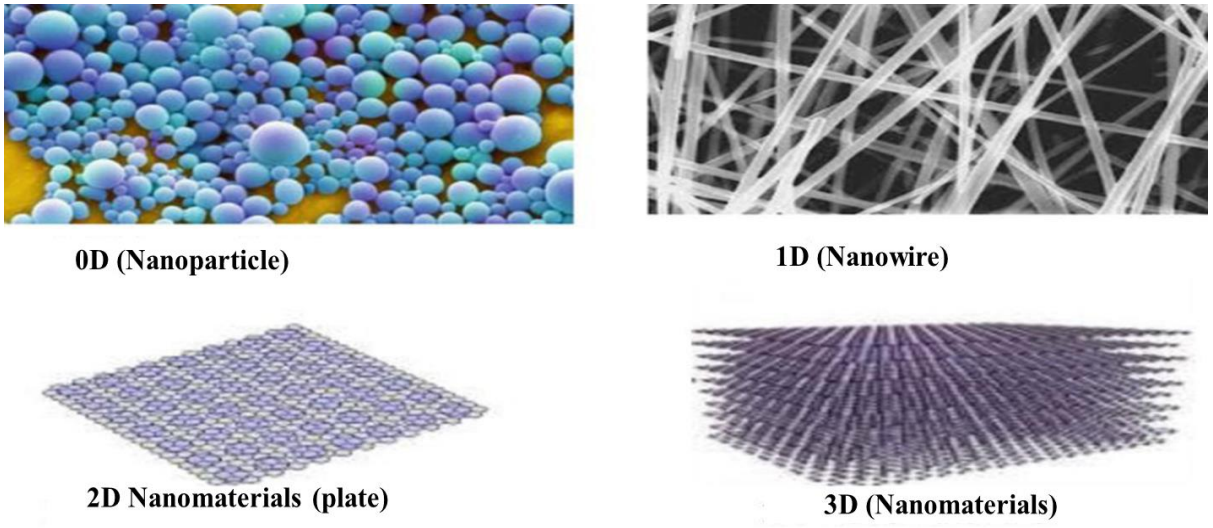

Figure 2.3: Type of nanomaterial (0D, 1D, 2D and 3D) (Ali 2020)

2.4.2 APPLICATION OF NANOMATERIALS

There are different applications of nanomaterials ranging from the chemical industry, optics, solar hydrogen, fuel cells, batteries, sensors, pharmaceuticals to the cosmetic industry (Ali

2020). In pharmaceutical and medicine nanomaterials are widely used for accurate and safer imaging of diseased tissues and novel forms of therapeutics (Chen *et al.* 2013; Sharma and Hussain 2020). The application of nanomaterials within the pharmaceutical field is claimed to be a safer method for drug delivery and efficacy as well as bioavailability (Ahmed *et al.* 2021).

Different attempts have been used for the synthesis, characterization and modification of metal oxide semiconductors such as WO_3, CuO, Fe_2O_3, ZnO and TiO_2 with applications to chemical sensing (Zappa *et al.* 2017), gas sensor (Tyagi *et al.* 2022), fabric (as anti-bacterial agents) fabric (Dastjerdi and Montazer 2010), and biomedical (Applerot *et al.* 2012). Literature reports the use of WO_3 in photocatalytic and photo electrocatalytic activity under visible light owing to its broad range of energy band gap values (Eg) 2.6–3.3 eV and 2.7– 2.8 eV optical transition of indirect type (Gillet *et al.* 2003). However, WO_3 is seldomly used since, its photochemical properties reduce recombination and visible light activity (Hepel and Luo 2001). Copper oxide (CuO) is a p-type semiconductor that is mainly applied in solar cell and organic photo oxidation. Although they can used as a semiconductor, but they are more difficult to use (Hepel and Luo 2001; Izaki *et al.* 2007). Iron oxide (Fe_2O_3) is another example of visible light active semiconductor oxide with energy band gap of approximately 2.2 eV (Li *et al.* 2021). Fe_2O_3 have a reasonable chemical stability, and does not photo corrode, however the location of valence and conduction bands resist the OH radical and hydrogen production, hence making it ineffective for the photocatalytic application in organic oxidation (Saeidi *et al.* 2020). Just like TiO_2, ZnO can be prepared in a variety of forms and structure. ZnO is the common alternative semiconductor particularly for the use of photocatalysis with similar energy band gap of Eg 3.3 eV, low cost, and non-toxicity, but it is known to photo-corrode (Saeidi *et al.* 2020).

2.4.3 TITANIUM DIOXIDE NANOPARTICLES (TiO_2-NPs)

Titanium dioxide (TiO_2-NPs) is one of the well-considered metal oxide nanoparticles because of its attractive electronic surface and catalytic properties. TiO_2-NPs occur in three polymorphs, namely anatase, and brookite and rutile as shown in Figure 2.4. Among these three, tetragonal crystallographic anatase and rutile with a band gap of 3.2 and 3.0 eV respectively (Nabi, Raza and Tahir 2020) are the most common. While brookite has an orthorhombic crystal structure with a band gap of 3.0 to 3.6 eV (Khare *et al.* 2011; Honarmand *et al.* 2019). Although anatase and rutile are well recognized, brookite and anatase phases are considered to be thermodynamically more stable than rutile structures under heat treatment at temperatures exceeding ~ 600°C (Medvids *et al.* 2021). Brookite is often unnoticed due to

reduced photo-reactivity when prepared it is usually prepared as a composite of anatase-brookite (Lu *et al.* 2011).

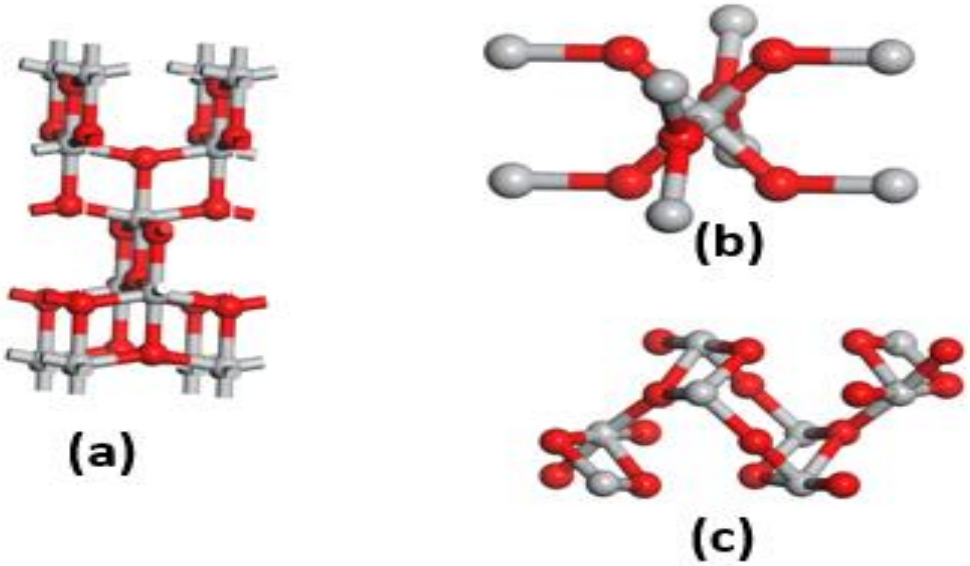

Figure 2.4: 3D representation of the polymorphs of TiO_2-NPs (a) anatase (b) rutile and (c) brookite (Biovia 2016).

2.4.3.1 Application of titanium oxide nanoparticles in electrochemical sensors

Several applications such as gas sensors and solar energy have used TiO_2-NPs because of their photocatalytic activities (Pathakoti *et al.* 2013; Verma *et al.* 2021). TiO_2-NPs are known for their biocompatibility, low toxicity, high surface area, thermal stability and a wide band gap which makes them popular in sensor applications (Oliveira and Morais 2018; Shetti *et al.* 2018; Tarahomi *et al.* 2018). Table 2.1 shows the application of TiO_2-NPs in electrochemical sensors.

Table 2.1: TiO_2-NPs based sensors summarize

Electrodes	Methods	Analyte	LODs (nm)	Reference
Glassy carbon	DPV	Vitamin B	0.05	(Revin and John 2012)
Carbon paste	DPV	Vitamin B	0. 7	(Nezamzadeh-Ejhieh and Pouladsaz 2014)
Glassy carbon	SWV	Vitamin B	8.4	(Gribat *et al.* 2017)
Carbon paste	DPV	Buzepide methiodide	8.2	(Kalanur, Seetharamappa and Prashanth 2010)
Gold	LSV	Hydrazine	3.0	(Aslışen and Koçak 2022)
Gold	LSV	Nitrite	10.0	(Aslışen and Koçak 2022)

2.4.3.2 Application of titanium oxide nanoparticles in photocatalysis

Across all metal oxides, TiO_2-NPs are the most remarkable metal oxides because of their photocatalytic, antimicrobial, and antibacterial effective applications which make them superior to others. In fact, TiO_2-NPs polymorphs are suitable for applications in photocatalysis (Ji *et al.* 2017; Chen *et al.* 2021). Review papers highlighted the photocatalytic activity of TiO_2-Nps focusing on the photocatalytic process reaction, mechanisms and applications (Xu *et al.* 2018a).

According to Paumo and co-workers, anatase is considered to be more active than the rutile form regarding photocatalytic properties (Paumo *et al.* 2021). TiO_2-NPs has been used in photocatalytic studies of organic pollutants effectively in wastewater treatment (Im, Kim and Lee 2008; Mondal and Sharma 2016). In another study synthesized TiO_2-NPs were used for the photocatalytic activity of propene oxidation with variable hydrochloric acid (Cano-Casanova *et al.* 2018). Propene has been selected as a representative substance for volatile organic compounds such as petrochemical plants (Cano-Casanova *et al.* 2018). In 2020, Le and co-workers investigated the effect of chemical structure degradation of organic dyes using TiO_2-NPs particles (Le *et al.* 2020). Recently Aravind and the team investigated the photodegradation of methylene blue dye using both green synthesized TiO_2-NPs and chemically synthesized TiO_2-NPs (Aravind, Amalanathan and Mary 2021).

The sensitivity of electrochemical sensor is affected by surface modification technique, electrochemical transduction mechanism and choice of the recognition receptor molecules. The most common strategy way to enhance the sensors performance is to chemically modify the surface of working electrode. Metal oxides (Elhag 2017), carbon nanotubes (Zaporotskova *et al.* 2016) and polymers (Lanzalaco and Molina 2020) have been frequently used to modify the sensors electrode. Nafion with it hydrophobicity property has been used as an electrode modifier for sensor electrode fabrication, enhancing the stability of graphene modified electrode due to its excellent film foaming ability (Wu *et al.* 2013). Electrochemical sensor of Biotin using nafion also shows the importance of using nafion on the modified electrode, where the selectivity and sensitivity of nafion forms a stable layer on the surface of Boron Doped Diamond electrode (BDD) for sensitive detection of Biotin (Buzid *et al.* 2018).

2.4.4 NAFION

Nafion is a sulfonated tetrafluoroethylene-based fluoropolymer-copolymer (Zhao *et al.* 2021). Nafion has been considerably used as an electrode modifier, because of its outstanding antifouling capacity, high permeability to cations and strong adsorption ability (Nigović, Marušić and Jurić 2011). In another study, nafion has been used as a proton exchange membrane in polymer electrolyte fuel cells, particularly for low-temperature hydrogen-oxygen fuel cells (Singh *et al.* 2016). Table 2.2 represents the application of nafion in an electrochemical sensor.

Table 2.2: Application of nafion in electrochemical sensors

Electrode	Analyte	Detection Method	Detection Limit	Sensitivity	Linear range	Interference	References
AG-nf-GC	DA	DPV	0.33	-	0.5-3.5	Acetaminophen	(Kim, Lee and Piao 2017)
GQD-nf-GC	DA	DPV	0.0045	-	0.005-100	AA, Au glucose, NaCl, $Ca(NO_3)_3$, $ZnSO_4$,$mgCl_2$	(Pang *et al.* 2016)
G-nf-GC	DA	LSV	1.0	7.695 $A\mu m^{-1}$	0.1-1.1	AA, UA	(Yusoff *et al.* 2015b)
G-nf-GC	AA	SWV	748	-	4000-10.00	DA, UA	(Gong, Wang and Yang 2017)
SsDNA-G-nf-GC	HIV-1 gene	EIS	2.3x10-8	-	1.0 $x10^{-7}$-0.001	-	(Yusoff *et al.* 2015a; Gong, Wang and Yang 2017)
G-nf-GC	NO	SWV	11.61	62µA Mm^{-1}	50-450	DA, AA	(Yusoff *et al.* 2015a)
nf-ERGO-GC	Bilirubin	SWV	0.84	-	2-20	UA, AA	(Aslıhan Avan, Aydar and Filik 2015)
MB-SGO-nf-GC	H_2O_2	Amperometric	1.5	0.19 µA M cm^{-2}	10-100	-	(Chen, Sun and Hou 2016)
Gox-Rgo-nf film	Glucose	Amperometric	170	3.8µA Mm^{-1} cm^{-2}	2000-20.000	AA, UA	(Choi *et al.* 2011)

AG-nf, Activated graphene-nafion; Gox, glucose oxidase; GQDs-nf, graphene quantum dots-nafion; HIV, human virus; LSV, immunodeficiency linear sweep voltammetry; mb-SGO-nf, myoglobin-sulfonated graphene oxide-nafion; nf-ERGO, nafion-electrochemically reduced graphene oxide; NO, nitric oxide; ssDNA-G-nf, single-stranded deoxyribose nucleic acid-graphene-nafion.

Table 2.3: Application of non-nafion electrochemical sensors

Electrode	Analyte	Detection Method	Detection Limit	Sensitivity	Linear range	Interference	References
N-GR/GCE	DA	DPV	0.25	-	0.5-170	UA	(Wang and Dai 2015)
rGo-CDs/GCE	DA	DPV	0.0015	-	0.01-450	AA, Au	(Sheng *et al.* 2012)
TiO_2-GR/GCE	DA	DPV	5-200		2.00	AA	(Fan *et al.* 2011)

N-GR, Nitrogen graphene; rGo-CDs,reduced graphene caarbon dot ; TiO_2, titanium dioxide.

2.5 SYNTHESIS OF NANOPARTICLES

The synthesis of NPs using the chemical method, which is divided into two categories: top-down and bottom-up approaches, has evolved over the past few years (Sorbiun *et al.* 2018), while the biological methods involve the use of different parts of plant extracts, and micro-organisms including algae, bacteria and fungi (Kamaruzaman *et al.* 2022).

2.5.1 CHEMICAL SYNTHESIS METHODS

2.5.1.1 Down chemical method of synthesis

This method entails the decomposition of the starting material into smaller nanosized structures (Agarwal and Brem 2017). For example, the most common techniques are lithographic techniques (i.e., UV, electron or ion beam, scanning probe, laser-beam processing, and mechanical techniques (i.e., machining, grinding, and polishing).

(a) Mechanical milling. Unlike many of the methods, mechanical attrition produces its nanostructures not by cluster assembly but by the structural decomposition of coarse-grained structures because of plastic deformation. In a mechanical milling medium, a high-energy mill comprises a powder charge, typically a blend of elements (Jeevanandam, Chan and Danquah 2016; Korni and Khalil 2017; Jeevanandam *et al.* 2022). Different kinds of ball milling can be used for the synthesis of nanomaterials in which balls influence the powder charge (Koch and Whittenberger 1996). Magnesium or copper-based nano alloys, have been synthesized with high yields, including the synthesis of different kinds of aluminium (Yadav, Yadav and Singh 2012).

(b) Physical vapour deposition (PVD): PVD is a technique that can be used to produce thin films and coatings. PVD is a process, where the material goes from a condensed phase to a vapour phase and then back to a thin film condensed phase. The more familiar processes: sputtering and evaporation are explained below (Moarrefzadeh and Branch 2012).

In sputtering synthesis, atoms are bombarded with ions and driven out until they encounter a substrate of their choice from which they wish to strike.

Sputtering is in thin films, nanostructures, coating and different materials such as metallic oxides, nitride, and carbide films (Ohta et al. 2018; López-Acosta et al. 2019). The sputtering can be used for the deposition of oxides and nitrides, as reactive sputtering (Rane et al. 2018).

The greatest advantage of using this technique is to ensure the purity of the NPs and a narrow size distribution while producing a high surface area (Vasudev, Thakur and Bansal 2016).

Evaporation processes are used in processing industries including food, pharmaceuticals, chemicals, and pulp and paper mills. The objective is to produce concentrated final products in the food industry (fruit juices and pastes, jams, condensed milk, etc.) or concentrated streams that can be further processed to produce crystallised products by crystallisation or powder products by drying (Hussein *et al.* 2020).

(c) Laser ablation is a technique that uses light amplification by stimulated emission of radiation (LASER) as a source of energy to remove the solid target (Padmanabhan 2019). This is a method for producing different kinds of nanoparticles including semiconductor quantum dots, carbon nanotubes, nanowires, and core shell nanoparticles. The laser parameters such as wavelength, pulse repetition rate, pulse width and pulse energy, and environmental parameters such as a vacuum, and a controlled gas or a liquid atmosphere are employed to produce a laser ablation technique (Gentile *et al.* 2021). Nanoparticles (NPs) generated by laser ablation are found to possess high purity of targeted ambient media without contamination from the reactor; however, it becomes hard to monitor their size distribution, agglomeration, and crystal structure control (Kim *et al.* 2017; Sadrolhosseini *et al.* 2019).

d) Thermal decomposition: Among the various techniques used for the synthesis of NPs. Thermal decomposition (TD) is a novel method that can be used to produce stable monodispersed particles such as copper NPs (Aminuzzaman *et al.* 2018). They are rapidly used in developed research areas, due to their fast responses, and cleaner and more economical processes. The synthesis could be achieved by using monodispersed metal nanoparticles (Sharifi, Steinacker and Saghafian 2016). The advantage of the TD method is the crystalline structure and size distribution are usually very high (Betancourt-Galindo *et al.* 2014).

2.5.1.2 Bottom-up chemical method of synthesis

The bottom-up approach exploits the chemical properties of the molecules to cause them to self-assemble into some useful conformation. Examples include sol-gel, solvothermal, hydrothermal, micro-emulsion and chemical precipitation (Saiduzzaman 2019; Myrovali 2020).

(a) Sol-gel method: This is a wet chemistry method which produces both glassy and ceramic materials, this method is generated to produce various kinds of high-quality metal oxides. Nanomaterials are normally produced using the sol-gel method by completing several steps, including hydrolysis, poly-condensation, drying, and heating (Peng *et al.* 2021). The first step is the hydrolysis of the metal oxide, taking place in either water or alcohol to form a sol. The next step takes place in the solvent viscosity to form porous structures such as hydroxo-(M–OH–M) or oxo-(M–O–M) bridges, resulting in metal–hydroxo- or metal–oxo-polymer formation in solution (Bhavani and Wani 2021). During this step, the distance between the colloidal particles increases while, porosity decreases and the distance between the colloidal particles increases. In the last step, the drying step, water and organic solvents are removed from the gel. Lastly, calcination is performed to achieve NPs (Parashar, Shukla and Singh 2020).

(b) Hydrothermal/solvothermal: Synthesis carried out using hydrothermal or solvothermal method can be achieved through a chemical reaction in an aqueous solution with a boiling point above that of water (100 ^{0}C) (Keskin *et al.* 2014). This technique is more applicable to different kinds of NPs, (Ishimoto *et al.* 2017). The method is generally based on heating both precursor and solvent at high temperatures in a closed system. The increase in temperature and the adjustment of the precursor allows the system to generate the desired nanomaterial. According to (Majidi *et al.* 2020) the most important parameter is the temperature, which should be high in order to develop well-structured nanoparticles. The solvent choice is also crucial. Moreover, there are other important factors to be considered, such as composition, concentration of the reactant and ratio of solvent to reducing agent.

(c) Precipitation method

The chemical precipitation is one of the promising methods for developing nano catalysts, since its permits the complete precipitation of metal ions (Li *et al.* 2018). Normally the precipitation method involves the removal of metal ions from the aqueous solution (Li *et al.* 2018). Allowing the precipitate to settle and then discarded from the solution using the filtration method (Chen *et al.* 2018).

Nevertheless, chemical synthesis is costly and regarded as unsafe for both humans and the environment (Pantidos and Horsfall 2014; Joshi and Adhikari 2019).

2.5.2 BIOLOGICAL SYNTHESIS METHOD

Biological synthesis is a green chemistry approach that deals with procedures without or with a minimum negative impact on human health and the environment (Joshi and Adhikari 2019). The most advantageous approach when it comes to biological synthesis is that they are stable in contrast to physical and chemical methods. In their involvement, they are more sustainable and more effective than the physical and chemical methods (Singh *et al.* 2017). (Adelere and Lateef 2016) describe the construction of metallic from agro waste, enzymes, and pigments from biological synthesis.

(a) Synthesis of NPs by plant extract:

Synthesis of NPs by plant extract is the most frequently used method because plants are suitable to fulfil the high demand for NPs with applications in environmental and biomedical fields. Different literature reports on the synthesis of metal/metal oxide nanoparticles such as gold (AuNPs), silver (AgNPs), palladium (PdNPs), copper (CuNPs), iron (FeNPs) (Guan et al. 2022); Fe_2O_3 (Devi et al. 2019) and TiO_2-NPs (Verma et al. 2022) have reported using different plant extracts including leaves, flowers, seed, fruits, stem and root. Table 2.3 show different methods used for the synthesis of TiO_2-NPs.

Table 2.4: Different methods or plants used for the synthesis of TiO_2-NPs

Sr. N	NPs	Plant used	References
1	TiO_2-NPs	Cassia fistula	(Swathi et al. 2019)
2	TiO_2-NPs	Nyctanthes Arbor-Tristis leaves	(Sundrarajan and Gowri 2011)
3	TiO_2-NPs	Psidium guajava	(Santhoshkumar et al. 2014)
4	TiO_2-NPs	Jasmine flower	(Aravind, Amalanathan and Mary 2021)
5	TiO_2-NPs	Syzgium cumini	(Thakur, Kumar and Kumar 2019; Sethy *et al.* 2020)
6	TiO_2-NPs	Azadirachta indica	(Thakur, Kumar and Kumar 2019; Sethy *et al.* 2020)
7	TiO_2-NPs	Black pepper (piper nigrum)	(Bhullar, Goyal and Gupta 2021)
8	TiO_2-NPs	Coriander Coriandrum sativum	(Bhullar, Goyal and Gupta 2021)
9	TiO_2-NPs	Clove syzguim aromatium	(Amanulla and Sundaram 2019)
10	TiO_2-NPs	Orange peel	(Amanulla and Sundaram 2019)

In green synthesis involving the use of plant, the leaves are washed rigorously with tap water, rinsed using distilled water to remove the impurities making that sure no residue is left thereafter dried in the oven or under sunlight or pulverized and boiled for some minutes. The mixture is then filtered and used in the synthesis of nanoparticles with a precursor. Research has documented that plants hold active phytochemicals with reducing, capping and stabilizing agents in the synthesis of nanoparticles (Vijayaraghavan and Ashokkumar 2017; Aslam, Abdullah and Rafatullah 2021).

(b) The use of fungi in the synthesis of nanoparticles (NPs)

The synthesis of NPs using fungi can be done, by the binding of polymers and metabolites to particular polypeptides (Adebayo *et al.* 2021). Fungi can easily be scaled up even in solid substrates from the fermentation technique, which is an important attribute of using them in nanoparticles (Adebayo *et al.* 2021). The use of fungi in nanoparticles are preferred since the well-binding and intracellular metal properties make it ideal for nano-biotechnological applications.

(c) Bacteria in the synthesis of nanoparticles

Biogenic sources such as fungi and bacteria are preferred not only for their ability to produce higher cytotoxicity for enzymes converting ionic forms into their nanoforms but also for their convenience in cultivating and regulating the size and morphology of synthesized nanoparticles (Lahiri *et al.* 2021). Nanoparticles can also be produced by biosynthesis using bacteria. Many types of nanoparticles have been synthesized using living and non-living bacteria (Reverberi *et al.* 2017; Allam *et al.* 2019).

(d) Algae in synthesis of nanoparticles

Algae are aquatic filamentous photosynthetic organisms that collapse from a planet. They are classified into two groups: microalgae (microscopic) and macroalgae (macroscopic). They play an important role in the field of medicine, pharmaceutical, aquaculture as well as cosmetic applications (Fon Sing *et al.* 2013; Jacob *et al.* 2021). Reports of algae have been observed on the synthesis of silver nanoparticles using *Ulva fasciata* extract as a reducing agent (LewisOscar *et al.* 2016). Recently, metallic nanoparticles have been synthetized using different algae such as chlorophyceae and phaeophyceae (diatoms and euglenoids) (LewisOscar *et al.* 2016; Sharma *et al.* 2016; Mal *et al.* 2021).

(e) Microbial synthesis, is one of the important techniques being used to produce NPs since physical and chemical synthesis are costly and utilize chemicals during the synthesis (Paul and Sinha 2014). While these methods are used in most applications, the use of toxic chemicals during the synthesis is still a major concern. Microbial synthesis is a rich biodiversity of microbes, which uses simple microbial cultivation, under cellular, biochemical, and molecular mechanisms.

Microbial synthesis of NPs can be achieved by micro-organisms, which are intracellular or extracellular, based on the location of NPs formation (Manivasagan, Nam and Oh 2016; Siddiquah *et al.* 2018). Many unicellular and multicellular organisms, such as bacteria (prokaryotes), fungi (eukaryotes) and viruses, produce either intracellular or extracellular inorganic materials (Thakkar, Mhatre and Parikh 2010). The development of these inorganic materials can be manipulated based on their shape and size by controlling the culture parameter.

CHAPTER THREE: THEORETICAL PRINCIPLES

This chapter outlines the theoretical principles that were used for both the experimental and computational procedures. A brief overview of the analytical instruments used followed by theoretical principles associated with Density Functional Theory (DFT), Time-Dependent Density Functional Theory (TD-DFT) and Monte Carlo (MC) simulations.

3.1 EXPERIMENTAL CHARACTERISATION TECHNIQUES

3.1.1 FOURIER TRANSFORM INFRARED (FTIR)

FTIR is a fast, simple powerful and versatile analytical technique that can identify biomolecules for capping, reduction, and stabilization for qualitative analysis of both organic and inorganic compounds (Cheeseman *et al.* 2021). The basic principle involves the absorption of light at a particular frequency, which is directly related to atom-atom vibrational energies in a molecule. The fingerprint region appears when infrared radiation passes through a sample, resulting in the absorption of the infrared radiation (Gilbert 2017). A typical schematic diagram of a modern FTIR spectrometer is presented in Figure 3.1.

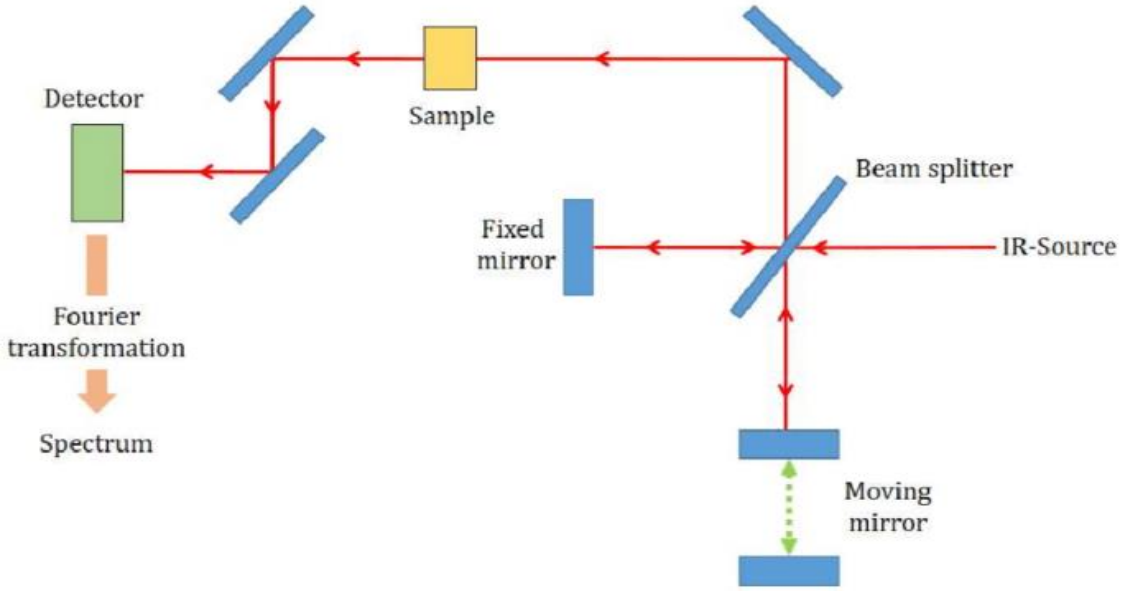

Figure 3.1: Schematic illustration of a modern FTIR spectrophotometer (Griffiths and James 2007)

3.1.2 UV- VISIBLE (UV-VIS) SPECTROPHOTOMETRY

UV-vis is a simple, sensitive, precise and accurate method to determine different samples. This technique measures both quantitative and qualitative analysis by measuring the absorbance of ultraviolet or visible light by a sample (Theophanides 2012; Rajeshkumar and Bharath 2017). The UV-vis spectrophotometry principle is based on the measurement of wavelength and intensity of ultraviolet and visible light absorbed by the sample as a function of the sample (Pratiwi and Nandiyanto 2022). The UV radiation corresponds to a wavelength of 180-380 nm, while the visible (visible light) corresponds to a wavelength of 380-780 nm (Yanenko, Shevchenko and Golovchanska 2018). Figure 3.2 shows a UV-vis spectrophotometry, where light is directed onto diffracting grating which divides the incoming light into component colours of different wavelengths.

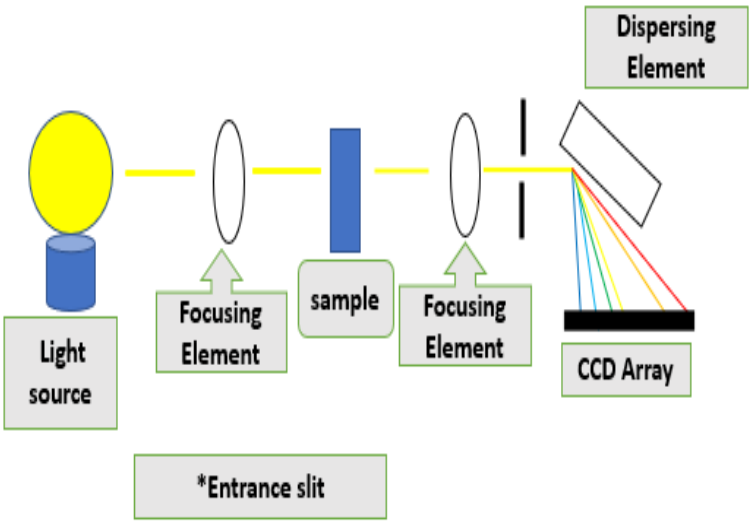

Figure 3.2: Schematic illustration of UV-visible spectroscopy

In general, the basic principle of UV-visible spectroscopy involves light which is either reflected or transmitted through the sample. Once the light is obtained from the sample it enters through entrance slit of a monochromator, where it is separated into different wavelengths using a dispersing element. The light is then focused onto a charge couple device (CCD). The modern derivation of the Beers Lambert law combines the two laws and correlates the absorbance of both the concentration and thickness of the material. The absorbance recorded is related to Beer's Law, based on the equation 3.1 below:

$$\boldsymbol{A = \varepsilon bc} \qquad 3.1$$

which states that the absorbance (A) is related to incident intensity (I_o), transmitted light (I) the concentration of liquid sample c and path length of the sample (b) and molar absorptivity (ε) (Sommer 2012).

3.1.3 TRANSMISSION EMISSION MICROSCOPY (TEM)

TEM is a powerful electron microscope technique that uses a beam of electrons to focus on a specimen, resulting in highly magnified and detailed images of a specimen. This technique focuses on obtaining information on the morphology of the sample (Shen *et al.* 2008; Venkateshaiah *et al.* 2020). The working principle of TEM is similar to the light microscope, however, the difference is that the microscope uses light rays to produce images, whereas TEM uses a beam of electrons on the specimen to produce images. In TEM a collimated beam of electrons passes through a sample and interacts and then the high energy can either be scattered or backscattered after interaction with the sample (Chaba 2018). Interaction of the electrons are transmitted through the sample to form an image. Furthermore, this technique allows for the generation of diffraction patterns of materials, therefore crystallography can be determined (Eggeman 2019) and can provide, dark or bright images that can produce precise particle size information at a nanoscale level (Calzolai, Gilliland and Rossi 2012; Eggeman 2019).

3.1.4 SCANNING ELECTRON MICROSCOPY (SEM)

The scanning electron microscopy provides structural information about the morphology of a sample at a nanoscale level (Khan *et al.* 2017). The principle is based on the initial electrons which are released from the source thereby providing energy to atomic electrons of the specimen, which can be further released as a secondary electron and thus an image is produced (Kwiecińska, Pusz and Valentine 2019). This technique has been used in the field of science for research, quality control and failure analysis such as nanotubes, nanofibers (Rennhofer and Zanghellini 2021), nano emulsions, solid lipid nanoparticles, and nanostructures (Saupe, Gordon and Rades 2006; Wu *et al.* 2021).

3.1.5 ENERGY-DISPERSIVE X-RAY SPECTROSCOPY

Energy-dispersive-X-ray spectroscopy can also be called EDs, EDX or EDXA; this technique is capable of resolving the elemental composition of an analyte. It works by permitting the

capacity of high energy electromagnetic radiation (X-ray) to core electrons from an atom. The principle is also called Moseley's Law which describes a direct correlation between the frequency of light and the atomic number (Dunlap 2018).

3.1.6 X-RAY DIFFRACTION (XRD)

XRD is one of the most extensive methods used for phase identification in crystalline materials (Cicchi, Cordero and Giomi 2011). The principle of XRD is based on constructive interference of monochromatic X-rays and crystalline samples (Hany 2022). Typically, XRD provides information regarding the crystalline structure, nature of the phase, lattice parameters and grain size of nanoparticle. The broadening of the most intense peak of an XRD measurement for a specific sample (Dhungana *et al.* 2018) the crystalline phase (D) is evaluated using the Scherrer equation (Eq 3.1). XRD uses an X-ray source of Cu α-radiation beam with excitation wavelength for analysis. In addition, XRD can be utilized to determine the charge distribution of crystalline materials such as nanomaterials. A typical schematic illustration of XRD is given in Figure 3.3, where the X-ray diffraction pattern generated from the crystalline material provides a unique fingerprint of crystals present in the sample.

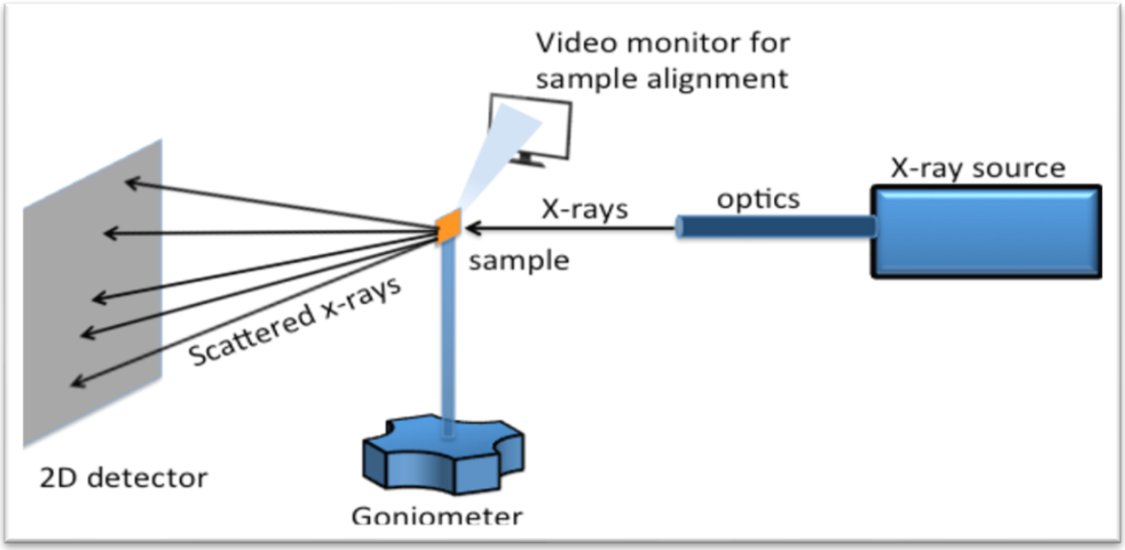

Figure 3.3: Schematic illustration of the X-ray diffractometer

The crystalline phase (D) is obtained by using the Scherrer equation

$$D = \frac{K\lambda}{\beta\, Cos\theta} \qquad 3.2$$

The corresponding equation 3.2 based on D, k, λ, β and θ correspond to particle size (nm), crystallized form factor (0.94), wavelength (0.154 nm), full width at half maximum (in radian) and angle of diffraction respectively.

3.1.7 CYCLIC VOLTAMMETRY (CV)

CV is one of the most used electrochemical methods in electrochemistry, it can provide both quantitative and qualitative analysis with a fast and reliable characterization tool. CV provides information to elucidate the kinetics of electron transfer, chemical reaction, thermodynamics and stability of reaction products (Wang and Jiao 2000; Gu *et al.* 2017). CV is based on the principle of linear sweep voltammetry that is used to measure the current while the potential is swept linearly as a function of time (Kim *et al.* 2020).

The curve obtained is called cyclic voltammogram as presented in Figure 3.4. Important key parameters measured in CV include the anodic and cathodic peak current (Ipa, Ipc) and the anodic and cathodic peak potentials (Epa, Epc). Furthermore, peak-to-peak separation (ΔE_p), ratio of anodic and cathodic peak current (I_{pa}:I_{pc}), active surface area (A), oxidation and reduction peak potential (Epa and Epc) and peak currents recorded at the electrodes can also be determined (Nnamchi and Obayi 2018).

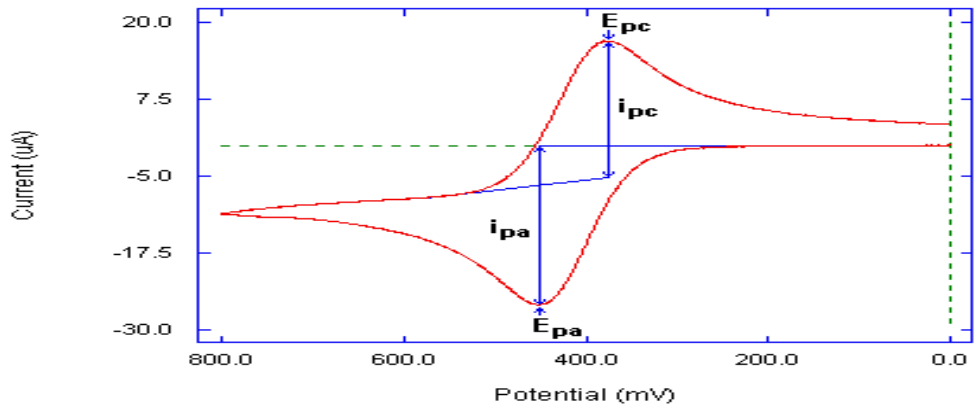

Figure 3.4: Typical CV showing important peak parameter

Equation 3.3 describes the CV voltammogram of a reversible process known as the Randle-Sevcik equation, with the planar electrodes and the peak current generated by reversible oxidation or reduction of an electrochemically active species.

$$\text{lp} = 2.686 \times 10^5 n^{3/2} A C D^{1/2} V^{1/2} \qquad 3.3$$

where Ip is peak current, A is the area of the electrode (cm^2), D is the diffusion coefficient (cm^2/s), C_o is the concentration mol cm^{-3} and v is scan rate potential Vs^{-1}.

The different types of cyclic voltammogram, namely reversible, quasi reversible and irreversible are illustrated in Figure 3.5. An electrochemically reversible/irreversible system is one where the electron transfer rate is sufficiently fast that equilibrium is achieved in a short time scale and maintained as the potential is varied. In other external systems with relatively slow electrode kinetics is classed as irreversible. In this case, equilibrium is not attained on the timescale of the experiment and a significant overpotential must be applied to drive the reaction; the system displaying intermediate electrode kinetics are termed quasi reversible (Batchelor-McAuley *et al.* 2008; Del Ángel-Gómez *et al.* 2022).

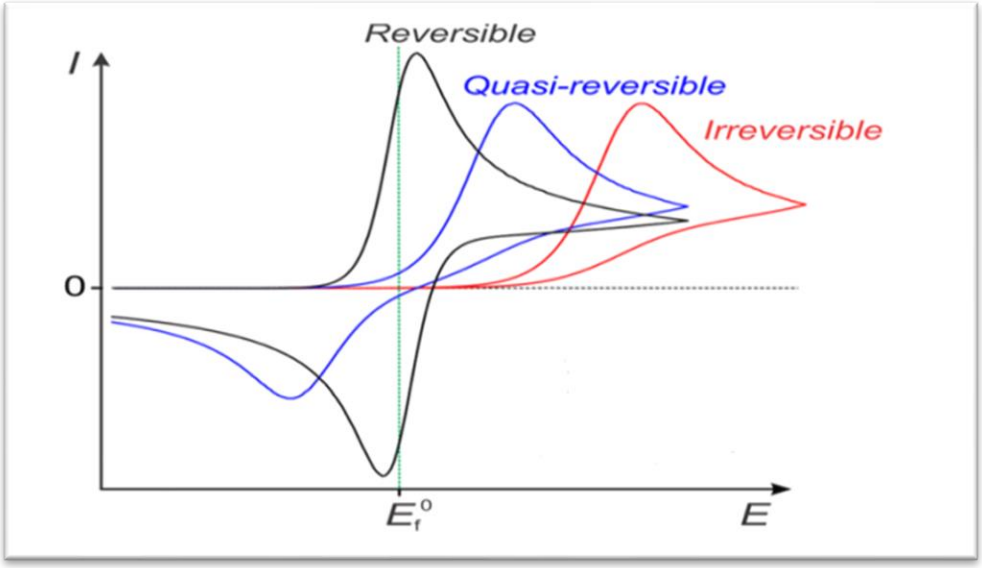

Figure 3.5: Typical CV for reversible, quasi-reversible and irreversible voltammogram.

3.1.8 DIFFERENTIAL PULSE VOLTAMMETRY (DPV)

DPV is used as quantitative chemical analysis to study the mechanisms, kinetics, thermodynamics of chemical reactions and to derive a linear sweep voltammetry with a series of voltage pulses, which are superimposed on the potential linear sweep (Mukhopadhyay and Nag ; Laborda, Bolea and Jimenez-Lamana 2014; Karimi *et al.* 2022). In DPV, the current is

measured in two points, the first point is measured before the application of the pulse and the second point is at end of the pulse as shown in Figure 3.6 (Scholz 2015).

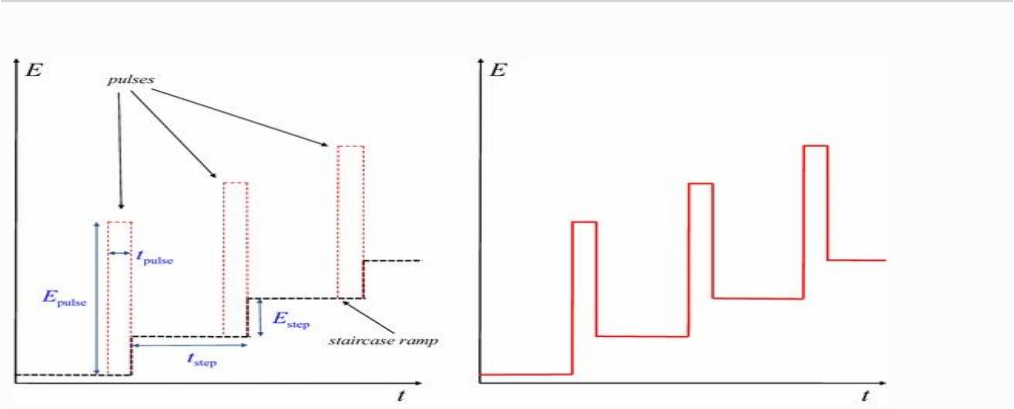

Figure 3.6: Typical Differential pulse voltammogram

It is generally the same as normal pulse voltammetry (NPV) in that its potential is also scanned with a series of pulses, with NPV being appropriate for both reversible and irreversible systems, producing high sensitivity (Northrop and Cole 2018). The voltammogram is a staircase-shaped signal and increases through the direction of potential Figure 3.7. DPV differs from NPV because here each potential pulse is fixed between (10-100 mV).

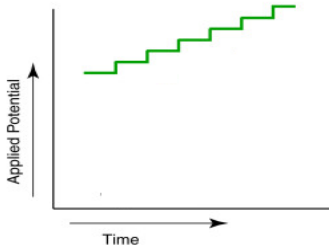

Figure 3.7: Typical staircase (Vilasó-Cadre *et al.* 2020)

In a staircase-shaped signal, the potential sweep is a series of steps and the current is measured at the end of each potential change.

3.1.9 ELECTROCHEMICAL IMPEDANCE SPECTROSCOPY (EIS)

EIS can be used to investigate the behaviour of the electrode surface or electrolyte material and they are useful in characterizing the conductivity and nanostructured surface area of nanomaterials (Shervedani and Lasia 1999; Torabi, Shervedani and Amini 2021). It can be employed for other studies including corrosion and electrodeposition. A sinusoidal ac voltage

probe is applied and the current response is determined (Randviir and Banks 2013). The impedance is produced when the redox reaction takes place, while the latter dc-based impedance and its electrical properties are generated by a double layer capacitance. The ac signal is scanned over a wide range of frequencies (100 000 - 0.1 Hz) to generate an impedance spectrum. Figure 3.8 shows a Nyquist plot, which provides an insight into the dynamics of the system. R_{ct} is inversely proportional to the rate of electron transfer arising from mass transfer limitations, while R_s is primarily from the electrolyte resistance and is useful in conductivity sensors, with all these components connected to the charge transfer resistance (Barua and Paul 2020). Warburg (*W*) represented by the semi-infinite straight line and assigned to the diffusion pathway of the electrodes, and constant phase element accordingly.

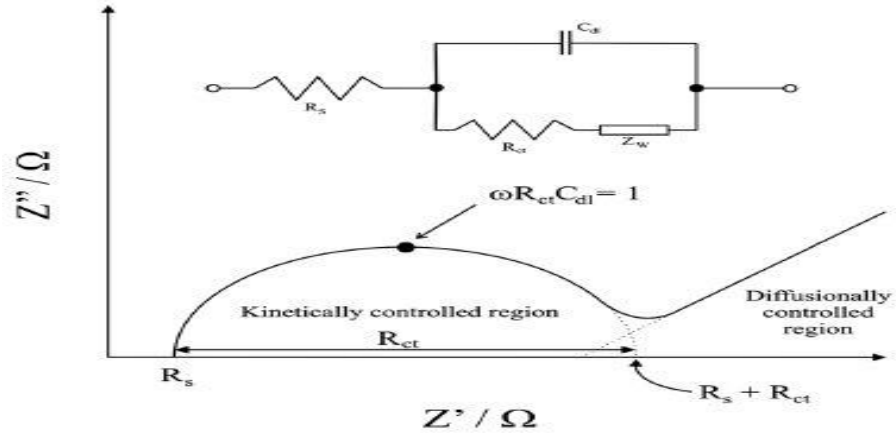

Figure 3.8: Shows a simple Randle's equivalent circuit for an electrochemical cell (Randviir and Banks 2013)

3.1.10 CHRONOAMPEROMETRY

Chronoamperometry is a time-dependent technique in which square wave potential is applied to the working electrode; in this principle, the current of the electrode is measured as a function of time (Guy and Walker 2016). Basically, chronoamperometry deals with the study of the variation of current response with time under potentiostat control (de Kruijff *et al.* 2019), normally in many experiments where the concentration of an electrode active analyte is not expected to change. The potential at the beginning value E_1 at which no faradic process is taking place to final value E_2. Figure 3.9 shows the electron transfer occurring sufficiently high over the potential.

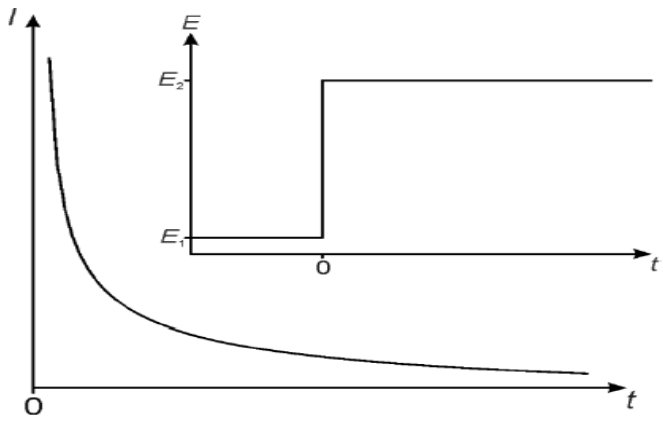

Figure 3.9: Chronoamperometry output signal (Lee 2014)

For the electrode where linear diffusion dominates, the diffusion limited current (I_d) over a practical timescale is calculated according to equation 3.3.

$$\boldsymbol{id = \frac{nFACD^{1/2}}{\pi^{1/2}t^{1/2}}} \qquad 3.3$$

Where n is the number of electrons transferred per molecule, F is the Faraday constant, A is the area of the electrode, D is the diffusion coefficient, t is the corresponding time with respect to the current and C is the concentration of the redox species in solution.

3.2 COMPUTATIONAL CHEMISTRY

Computational chemistry plays a major role in the field of chemistry by incorporating efficient computer programs to solve chemistry problems. It is used to calculate the geometrical structures and properties of molecules, groups of molecules and solids. The main function of computational chemistry is to complement the experimental results, producing a more accurate result. Modelling can be used for chemical reactivity, the energy of the molecule and transition state, molecular geometry and physical properties of the substance. It can be used in some cases to predict the chemical phenomena and it is widely used in the design of new drugs and materials. Computational methods, including quantum mechanics and molecular mechanics/force field methods, with relevant and enough parameters, can provide information that is comparable and complementary to that obtained from experimental studies.

3.2.1 DENSITY FUNCTIONAL THEORY METHODS (DFT)

Density functional theory (DFT) methods are used to determine molecular electronic structures, even though many of the most common functionals use parameters derived from empirical data, or more complex calculations (Landers, Gor and Neimark 2013). The total energy in DFT is expressed in terms of the total one-electron density rather than the wave function. (Jain, Shin and Persson 2016) described the behaviour of electrons using DFT calculations based on the Schrödinger equation. In this type of calculation, there is an approximate Hamiltonian and an approximate expression for the total electron density. The basic idea for the DFT theory is due to Hohenberg and Kohn (1960) who formulated the Hartree Fock (HF) theory. Similar to the HF orbitals, DFT methods can be very accurate with low computational costs. The quality of a given result can be determined by comparing it with the experimental results obtained in similar systems. The basis for DFT methods is that the electron density determines the ground state electronic energy, there is a complete relationship between the electron density of a system and the energy (Yang 1991).

While some DFT methods are parameterized, for example, the generalized gradient approximation (GGA) methods with the Becke, Lee, Yang and Parr (BLYP) functional, ab initio methods are based on first principles, namely, the computations are derived solely from the laws of quantum mechanics. Generally, DFT methods are computationally less intensive than ab initio methods while producing comparable results in terms of quality.

Fiolhais *et al*. (2003) used DFT for calculating the properties of solid state physics and molecules. According to Lundqvist and March (2013), Hohenberg and Kohn (1964) and Kohn and Sham (1965) established papers based on the information for calculating the properties of solid state physics and molecules for replacing many body wave functions by one-electron orbitals (Hohenberg and Kohn 1964; Kohn and Sham 1965).

The first theorem explains the electron density that has a significant influence on the external potential. The second theorem was for several positive definite trial densities such as (rt), namely, $\int \rho t\ (\mathbf{r}) d\mathbf{r}$=N then E $[\rho t] \geq E_o$. This can provide direct proof of the above-mentioned theorem; where the first theorem was lengthened with a degenerated state (Levy 2010; Dreizler and da Providência 2013).

Based on Hohenberg and Kohn's first theorem, it can be noted that trial density establishes a sole trial of the Hamiltonian and therefore, the wave function can be expressed as (Ψ);

$E[\rho t]=\langle \psi t|H|\psi t\rangle \geq E_o$, which is derived from the Schrödinger equation on the variational theorem $E[\rho t]=\langle \psi t|H|\psi t\rangle \geq E_o$. this equation is from the first theorem of Hohenberg and Kohn used to define the trial density of Hamiltonian and the wave function to be (Ψ); $E[\rho t]=\langle \psi t|H|\psi t\rangle \geq E_o$. Equation 3.4 illustrate variational theorem derived from the Schrödinger. This formula restrains the DFT to discover on the ground state level particularly. Little addition permits the variation with regards to the excited state which can be assured intersecting with the ground state.

$$\boldsymbol{\delta\left[E[\rho]-\mu\left(\int \rho\,(r)dr-N\right)\right]=0} \qquad 3.4$$

Ground state level can be accomplished using wave function, these theorems set the basic equation of DFT (Friston, Harrison and Penny 2003).

The original DFT theorem is applied for observing the electronic energy on the ground-state level of a molecule. Kohn and Sham formulated an approach analogous to the Hartree-Fock (HF) method in terms of structure (Zhang *et al.* 2005)

The B3LYP basis sets

Hybrid functions are groups of approximations to the exchange-correlation energy function used in DFT, it can absorb a portion of the exact exchange from Hartree-Fock theory with the rest of the exchange energy from other sources, such as *ab initio* or empirical methods. The energy is expressed in terms of the Kohn-Sham orbital, apart from the density. One of the most commonly used methods is the B3LYP; B3 represents the Becke 3 parameter and LYP represents Lee-Yang-Parr. The B3LYP commonly combines the conventional GGA functionals with Hartree-Fock. (Sousa, Fernandes and Ramos 2007).

The main purpose of the B3LYP basis sets is to introduce the hybrid nature of solids or molecules in a mathematical model with different approximations (Becke-1988 (B88), Lee-Yang-Parr 1988 (LYP88), and Vosko, Wilks, Nusair 1980 (VWN80) all belonging to the group of B3LYP hybrid functionals. There are great advantages to using hybrid functionals, such as significant enhancement over GGA and in many molecular property determinations. However, the disadvantage of using B3LYP in solid state or in materials containing metals includes poor

accuracy owing to the calculation of the exchange portion within a plane wave basic set (Sousa, Fernandes and Ramos 2007).

3.2.2 TIME DEPENDENT DENSITY FUNCTIONAL THEORY (TD-DFT)

TD-DFT is a continuation of density functional theory, it shows how the time dependent wave function is equivalent to the dependent wave function. The difference between the two is that TD-DFT uses time-dependent potentials as a magnetic field. According to Marques and the team, TD-DFT can be used to quantify the excited state properties as well as excitation energies and UV-vis spectra (Marques and Gross 2004). The theorem for DT-DFT is based on Hoheburg-Kohn's time dependent theorem. Hence, the Runge gross theorem is actually based on the relation between the time dependent external potential with an electron density of the n(r,t), resulting in the external potential V_{ext} (r,t) and V_{et}(r,t) as shown in equation 3.5.

$$\boldsymbol{\upsilon KS\,(r,t) = \upsilon ext\,(r,t) + \upsilon HARTREE\,(r,t) + \upsilon xc\,(r,t)} \qquad \mathbf{3.5}$$

The time-dependent equation for Kohn Sham is used to approximate $V_{xc.}$ Many reports have successfully used TD-DFT to study the optical properties of complexes, showing a good comparison between experimental and calculated results.

Schrodinger's equation can be used to calculate the external potential, energy and properties as a function of time-dependent electron density. The theorem used to calculate the energy and electron density accurately is given by the following equation 3.6

$$\boldsymbol{n(r,t) = \Sigma|\varphi i(r,t)|i^2} \qquad \mathbf{3.6}$$

3.2.3 MONTE CARLO (MC) SIMULATIONS

MC simulation methods have increasingly become an effective tool for mimicking the experimental work, with computational analysis for complex nonlinear systems to provide more accurate results and predict their interactions (Honerkamp and Weese 1990). It has become one of the most popular techniques for fluid modelling at an atomic level since it provides accurate results regarding the experimental results. Furthermore, MC can improve the understanding at a molecular level (Kalinichev and Kirkpatrick 2007; Raychaudhuri 2008). MC does not require solving any of Newton's equations of motion, no dynamic information can be gathered from traditional MC simulations. Unlike MD simulations, they are free from

the restrictions of solving Newton's equations of motion, this allows them to generate trial configuration with satisfying results. The MC approach has statistical components and can be out carried using the Material Studio program (Biovia 2016). Basically, these modules calculate electronic properties based on quantum mechanics and are composed of the following three parts:

(i) General configuration

(ii) Traditional metropolis

(iii) Optimization devices.

When the calculation is done, the results are weighed by Boltzmann distribution to yield validated results as shown in Figure 3.10. The MC simulation can be carried out using the following steps.

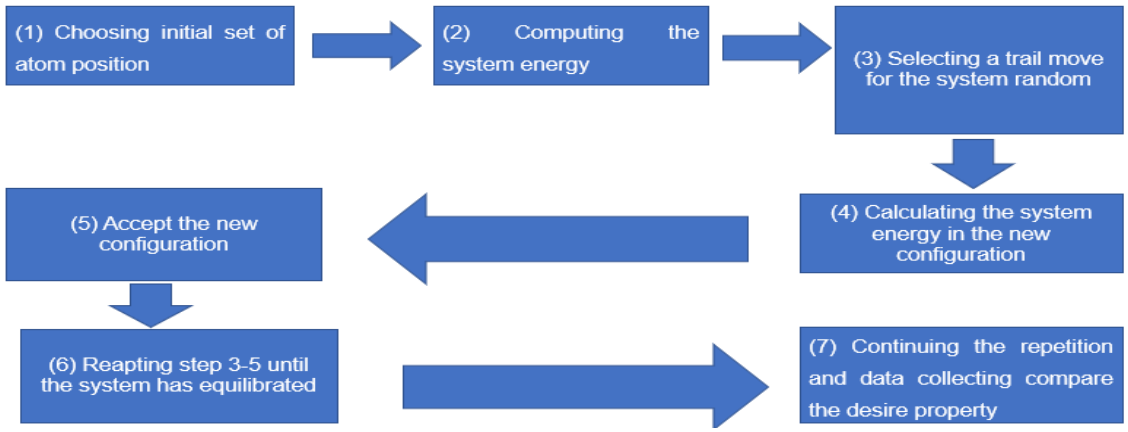

Figure 3.10: Step-by-step diagram of MC simulations

The method has a unique process, whereby the sampling methods of configuration spaces resulting from the first configuration generate a new configuration by randomly selecting a molecule, then changing and rotating the molecule in order to generate several internal structures.

CHAPTER FOUR: MATERIALS AND METHODS

This chapter describes the materials and methods used for the experimental and computational work implemented in this study.

4.1 EXPERIMENTAL SECTION

4.1.1 MATERIALS AND METHODS

All analytical grade reagents were used for this study. Sodium phosphate dibasic (Na_2HPO_4) and sodium dihydrogen phosphate dihydrate ($NaH_2PO_4.2H_2O$) were obtained from Capital Lab Supplies (Durban, SA). Nitrogen gas of 99.9% purity was obtained from AFROX (Durban, SA). Alumina powder ≤ 3µm was supplied by Metrohm (Durban, SA). N N-dimethyl formamide (DMF), methanol 99.9% were supplied from the lab, Efavirenz (EFV) reference standard and titanium tetraisopropoxide (TTIP) and nafion (5% wt) were supplied by Sigma-Aldrich. All reagents and samples were prepared with de-ionized water.

4.1.2 INSTRUMENTATION

Electrochemical experiments were conducted using Metrohm Auto lab potentiostat PGSTAT 302 with 663A Computrace, controlled by NOVA 2.1.4e in a three-electrode system. The system comprises the working (glassy carbon), reference (silver/silver chloride saturated 3 M potassium chloride), and counter (platinum) electrode in a supporting electrolyte (Phosphate buffer). Measurements were carried out by application of CV, EIS and DPV. The morphologies and characterization were obtained from (FTIR), (UV-vis), (XRD (SEM), and (TEM).

4.1.3 PREPARATION OF PLANT EXTRACT

Synthesis of TiO_2-NPs was carried out using Harvested *Eucalyptus globulus* leaves from the Eastern Cape. The extract from the plant leaves has been used in applications as a stabilizing or reducing agent (Sharma, Kanchi and Bisetty 2019). Leaves were washed with tap water, rinsed using deionised water, dried in the oven for 2 h at 50 °C and ground to powder. 25 g of the dried ground leaf was transferred into a beaker containing deionised water (250 mL). The solution was heated while stirring at 50 °C for 30 min, then cooled and filtered.

4.1.4 SYNTHESIS OF TITANIUM (IV) OXIDE NANOPARTICLES

TiO_2-NPs were synthesized using titanium tetra-isopropoxide (TTIP) (0.1 M, 50 mL). Leaf extract (20 mL) was added dropwise to the above solution of TTIP. The leaf extract plays the role of a stabilizing or reducing agent in the synthesis of TiO_2-NPs (Sharma, Kanchi and Bisetty 2019).The mixture was stirred for 3 h at room temperature which resulted in a white precipitate as presented in Figure 4.1. The change of colour from white precipitate to yellowish-grey confirms the formation of TiO_2-NPs. The formed TiO_2-NPs were separated by centrifugation of the mixture at 5000 rpm for 20 min and washed with deionised water (DW) to remove impurities and then dried in the oven overnight at 100 °C. It was then calcined in a muffle furnace at 500 °C for 3 h (Ahmad, Jaiswal and Soni 2020).

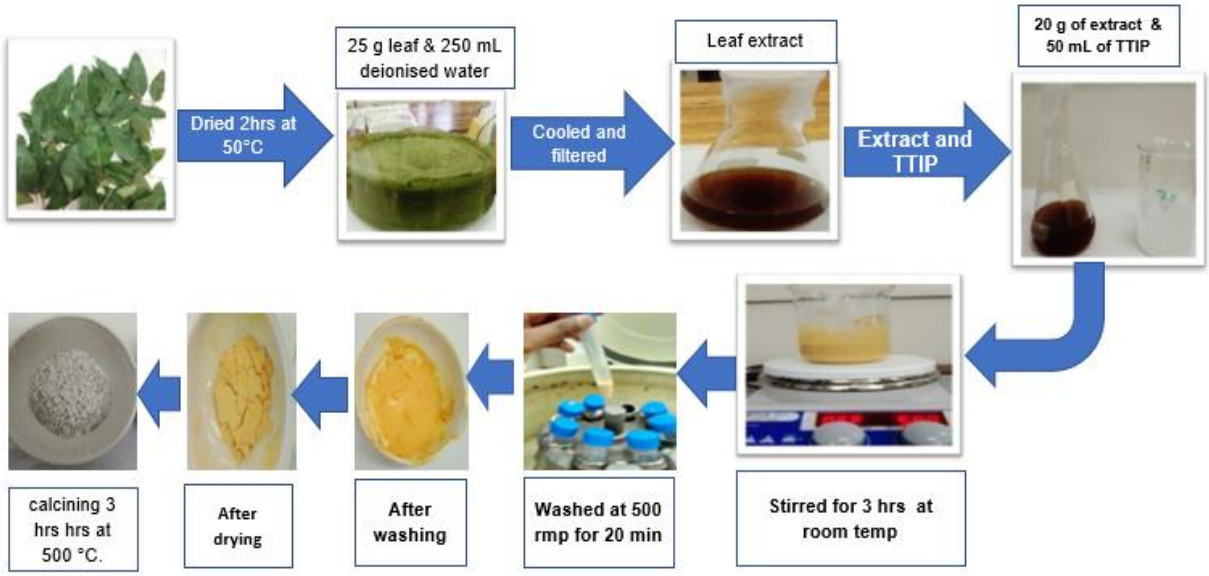

Figure 4.1: Synthesis of titanium (IV) oxide nanoparticles

4.1.5 ELECTRODE PRE-TREATMENT AND MODIFICATION

Glassy carbon electrode was cleaned by a micro cloth pad containing an alumina nano powder slurry for polishing the electrode. The electrode was rinsed with a DW, kept in 50% methanol for a minute, rinsed again with a DW to remove residues of alumina nano powder and to obtain a mirror like surface, kept in 50% HNO_3 for 50 s and finally rinsed with DW and dried in the oven at 40 °C for 2 min. GCE was modified using a drop-drying method. A nanoparticle modified glassy carbon electrode (GCE/TiO_2-NPs) was prepared by weighing TiO_2-NPs (3 mg) into a glass vial followed by the addition of 300 µL of DMF, the mixture was stirred on a hot

plate for approximately 10 min for complete homogenization. Approximately 2.0 µL of the resulting paste was dropped onto a bare GCE and oven-dried at 50 °C for a minute to yield working electrodes GCE/TiO_2-NPs. The modified electrode was allowed to cool at room temperature, thereafter 20 µL of 0.5% nafion was deposited on the modified electrode and allowed to dry at room temperature, yielding GCE/TiO_2-NPs-nafion electrode. Scheme 1 illustrates the design of the sensor for EFV detection.

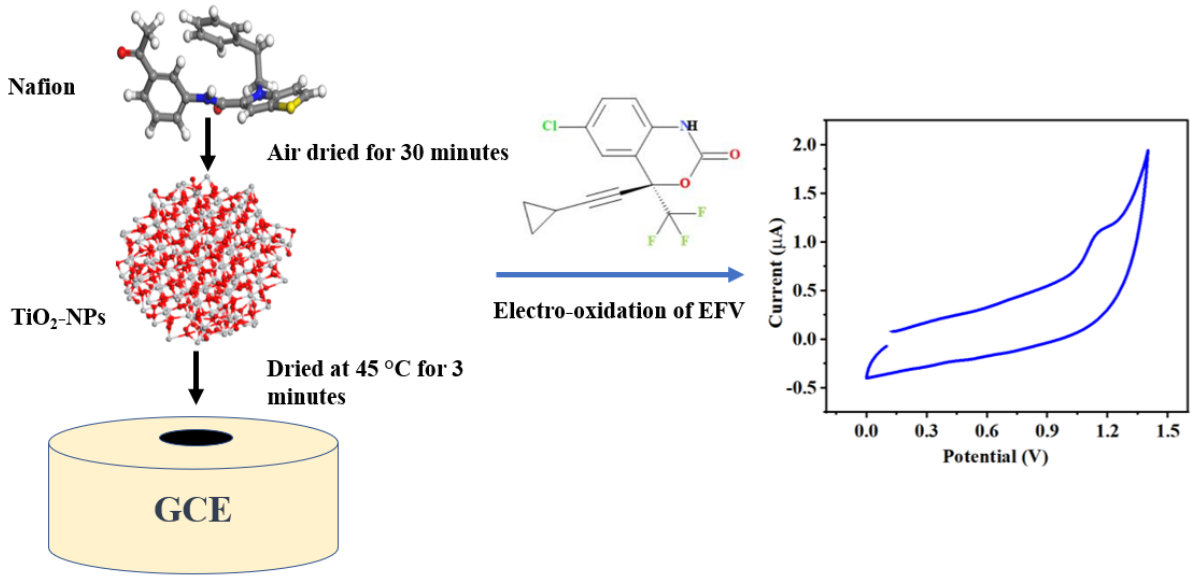

Scheme 1: Diagram illustration of electrode modification for EFV detection

4.1.6 PREPARATION OF ELECTROLYTE SOLUTION

A supporting electrolyte of 0.1M PBS buffer was prepared by mixing an equal amount of sodium phosphate monobasic (Na_2HPO_4:99%) and sodium phosphate dibasic (NaH_2PO_4:99%) at pH 7.02. mixture with potassium ferrocyanide $[Fe(CN)_6]^{3-/4-}$.

4.1.7 PREPARATION OF EFV STOCK SOLUTION AND SUB-SOLUTION.

An EFV stock solution of 1 mM was prepared using 0.0078 g and dissolved in 25 mL pure methanol, wrapped in an aluminum foil and kept in the refrigerator prior to analysis. Working solutions for the CV, EIS, DPV and chronoamperometry measurements were prepared from the stock solution by appropriate dilution of a known amount of stock solution. It was covered with foil and stored in a refrigerator.

4.1.8 REAL SAMPLE PREPARATION AND ANALYSIS

Real samples were prepared using a commercially available EFV (Cipla) tablet. The tablet (1.3120 g) was pulverized into a fine homogenous powder using a mortar and pestle. 10 mg of EFV ground tablet was dissolved in a 10 mL volumetric flask containing methanol and made up to mark with methanol. The mixture was sonicated for complete homogenisation and thereafter filtered to remove particulates. An electrolytic cell containing 10 mL of PBS was used for a 1 mL sample spiked with different concentrations of EFV standard and analysed employing DPV. The recovery of analytes in the sample was estimated from a constructed calibration graph.

4.1.9 CHARACTERIZATION OF TiO_2-NPS

The morphology of TiO_2-NPs was examined on a field emission scanning electron microscopy (FESEM), using the Tescan MIRA SEM, while the energy-dispersive X-ray spectra (EDX) was obtained employing the Thermo Fisher Nova NanoSEM, with an Oxford X-max 20 mm^2 detector and INCA software. The optical property and crystallinity of the synthesized nanomaterial were investigated using Fourier transform infrared spectroscopy (FTIR), ultraviolet-visible spectrophotometry (UV-vis), X-ray diffraction (XRD), scanning electron microscopy (SEM), and transmission electron microscopy (TEM). 5 mM of $[Fe(CN)_6]^{3-/4-}$ probe solution prepared in a 0.1M of PBS at pH 7 was used for electrochemical characterization of synthesized TiO_2-NPs as well as TiO_2-NPs-nafion using cyclic voltammetry (CV), and electrochemical impedance spectroscopy (EIS).

4.1.10 ELECTROCHEMICAL STUDIES

Metrohm Auto lab potentiostat PGSTAT 302 with 663A Computrace in a three-electrode system was used to conduct experimental procedures. The system comprises the bare and modified working glassy carbon (GCE, GCE/TiO_2-NPs and GCE/TiO_2-NPs-nafion), reference (silver/silver chloride saturated 3 M potassium chloride), and counter platinum electrodes in supporting electrolyte. Measurements were carried out by application of CV, EIS, DPV and CA using bare and a modified glassy carbon electrode (GCE).

4.1.11 ELECTROCHEMICAL PROPERTIES OF EFV

The electrocatalytic properties of the bare and modified electrode towards 4.7×10^{-2} mM EFV were investigated using CV at 25 mV/s within potential windows of -0.2 to 1.4 V. EIS

measurement 1.2 V was carried out between a frequency range of 100 kHz and 0.1 Hz at constant potential of 1.2 V for detection EFV and 0.2 V for electrochemical characterization in a 5 mM $[Fe(CN)_6]^{3-/4-}$ solution. Quantitative detection of EFV was conducted using DPV with control conditions of 0.005 V step potential, 0.025 V modulation amplitude and modulation time of 0.05 s. Selectivity study of GCE/TiO_2-NPs-nafion towards EFV in the presence of interfering species was investigated using CA.

4.1.12 PHOTODEGRADATION OF EFV

Stock solution was prepared from 0.0078 g of efavirenz (EFV) and diluted in a 25 mL of pure methanol, while (1.0 g/mL) of TiO_2-NPs was used. EFV and TiO_2-NPs were mixed in a 250 mL beaker with ratio of (1:1). The mixture was left in the dark under magnetic stirring in order to establish adsorption-desorption equilibrium (Brooms *et al.* 2018) (Aravind, Amalanathan and Mary 2021). An aliquot of the sample was withdrawn hourly from 0-5 h, the sample was filtered using Whatman filter paper to remove the impurities. The photodegradation was recorded using UV–visible irradiation.

4.2 COMPUTATIONAL SECTION

4.2.1 MODEL BUILDING

The 3D molecular structures for EFV and nafion were retrieved from the PubChem database, while the construction of the nanostructures to mimic glassy carbon electrodes were constructed from Materials Studio (MS) software package developed by BIOVIA (Biovia 2016) performed with the Forcite module used geometry optimization of all 3D model structures. The Forcite code was implemented to observe the low energy configuration of the EFV molecule, along with the 'ultrafine' quality of the COMPASS force field.

4.2.2 DENSITY FUNCTIONAL THEORY (DFT) CALCULATIONS

In order to understand the chemical reactivity of EFV from its electronic properties (HOMO-LUMO frontier orbitals), DFT calculations were used to perform the geometry optimization and frequency analysis of EFV, using the B3LYP density functional (Lee, Yang and Parr 1988; Becke 1993) and the 6-311+G basis set using the Gaussian 09 package (G.W.T. M. J. Frisch 2016).

4.2.3 MONTE CARLO (MC) SIMULATIONS

The atomistic interactions between the substrate and the adsorbate were studied using the Adsorption Locator (AL) module in the MS program on the layers of assembly set at 298 K, and this was done to understand the molecular interactions at an atomic level. With the forcefield method, AL was utilized as a preparation and screening tool to produce a ranking of the energies for each created configuration, indicating the preferable adsorption sites. Because the adsorbate can be adsorbed at several places on the GCE/TiO_2-NPs surface, the AL module was utilized to determine the optimal adsorption site on the surface with the lowest energy. The lowest adsorption energy conformers for GCE/TiO_2-NPs-EFV and GCE/TiO_2-NPs-nafion-EFV were separately optimized using the Forcite module to attain a stable conformation.

CHAPTER FIVE: RESULTS AND DISCUSSION

This chapter deals with the outcome of the two case studies involved in this research.

5.1 CASE STUDY I

DESIGN OF A SENSING PLATFORM FOR EFAVIRENZ

5.1.1 EXPERIMENTAL SECTION

5.1.1.1 Spectroscopic and morphological characterization

The FTIR spectrum of TiO_2-NPs is presented in Figure 5.1. The result exhibited significant peaks at 453 and 832 cm^{-1} corresponding to Ti-O stretching vibrational bands, and Ti-O-Ti bridge stretching mode accordingly. The peaks at 1215, 1734, 2313 and 3765 cm^{-1} were assigned to the C-O stretch of the carboxylic group, C=O of the carbonyl group, C-H group which demonstrate the reduction of titanium ions (Ti^{4+}) of the starting material, and O-H stretching mode of hydroxyl group respectively. The successful synthesis of TiO_2-NP is confirmed by the vibrational band at 453 cm^{-1} which is close to the previous report (493, 450 cm^{-1}) in literature (Justh et al. 2017; Sethy et al. 2020).

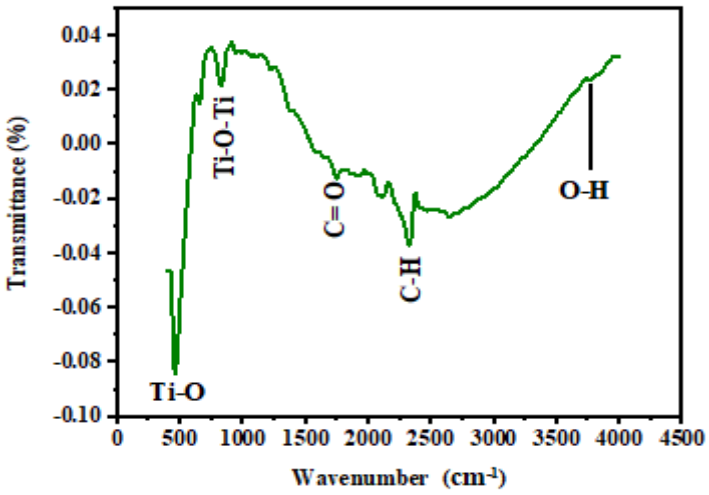

Figure 5.1: FTIR spectra for green synthesized TiO_2-NPs

Figures 5.2 A and B show the UV-vis spectra of *Eucalyptus globulus* leaf extract and synthesized TiO_2-NPs with absorption bands noticed at 360 and 365 nm respectively. The observed band for TiO_2-NPs is close to the band (356) reported in the literature (Sethy *et al.* 2020). The slight shift in vibration to a higher wavelength suggest the occurrence of interaction between the leaf extract and TTIP in the synthesis of TiO_2-NPs.

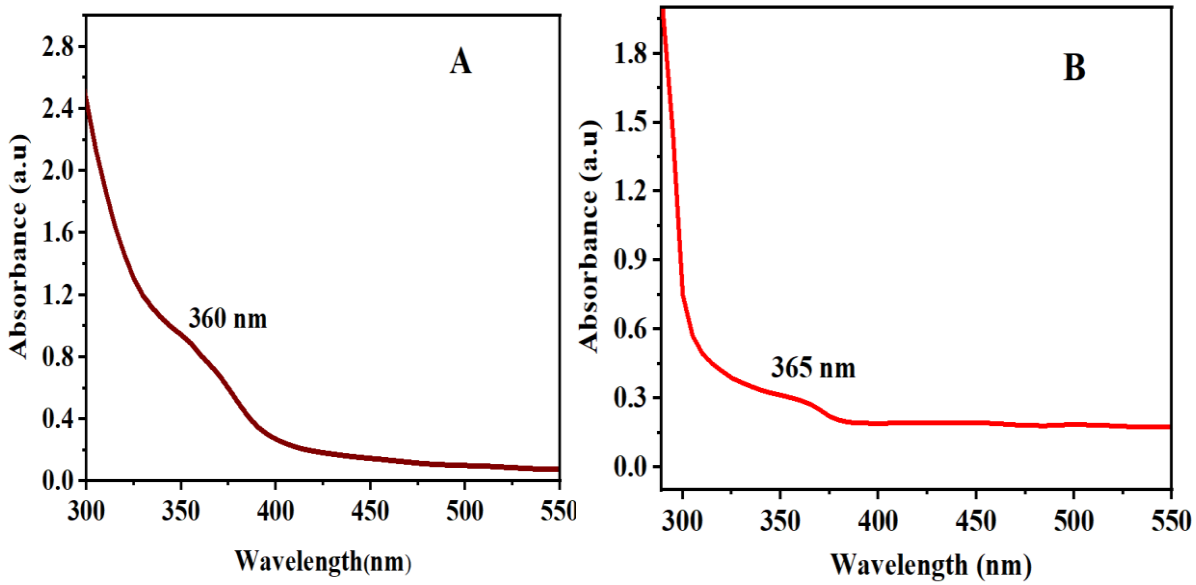

Figure 5.2: UV–vis spectra of (A) Extract and (B) TiO_2-NPs

Morphology of green synthesized TiO_2-NPs was observed using SEM, in SEM the high surface area electrode material enhances the electrochemical performance of supercapacitors. The SEM analysis was performed to determine the shape of TiO_2-NPs which was presented in Figure 5.3 revealing the agglomeration of nearly spherical-shaped particles.

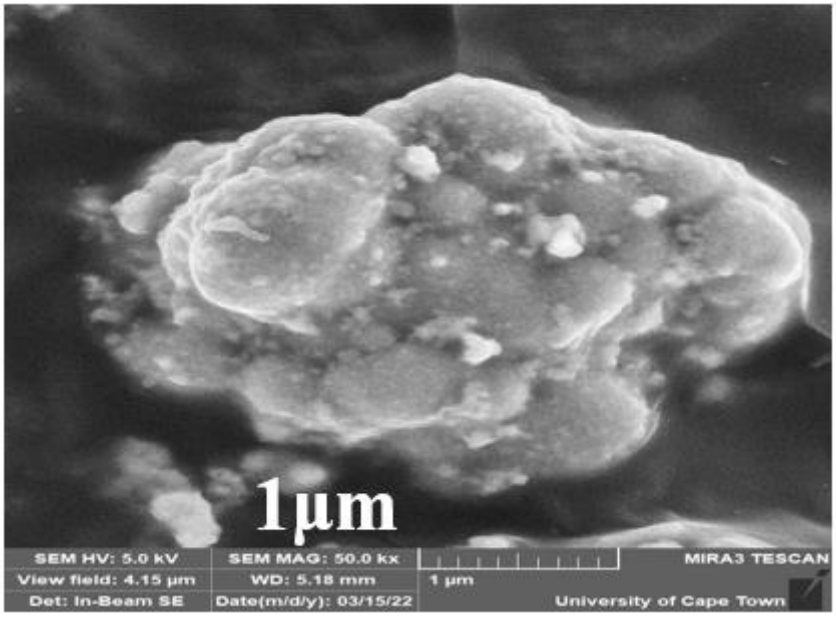

Figure 5.3: SEM image of green synthesized TiO_2-NPs

The XRD pattern of TiO_2-NPs shown in Figure 5.4 was conducted in the range of 10-80$^{\theta}$. Characteristics peaks of 29.487, 44.281, 56.427, 63.641, 64.965 and 74.270 indexed to 101, 210, 211, 204, 213 and 215 diffraction planes were recorded. The crystalline size (D) was calculated to be 5.7 nm for TiO_2-NPs and anatase from the 101 plane employing the Debye-Scherrer formula: $D = \frac{k\lambda}{\beta Cos\theta}$. The correlated D, k, λ, β and θ correspond to particle size (nm), crystallized form factor (0.94), wavelength (0.154 nm), full width at half maximum (in radian) and angle of diffraction orderly. The obtained crystalline size (5.7 nm) is within the reported range (2.3 - 8.5 nm) in the literature (Bekele *et al.* 2020; Sethy *et al.* 2020).

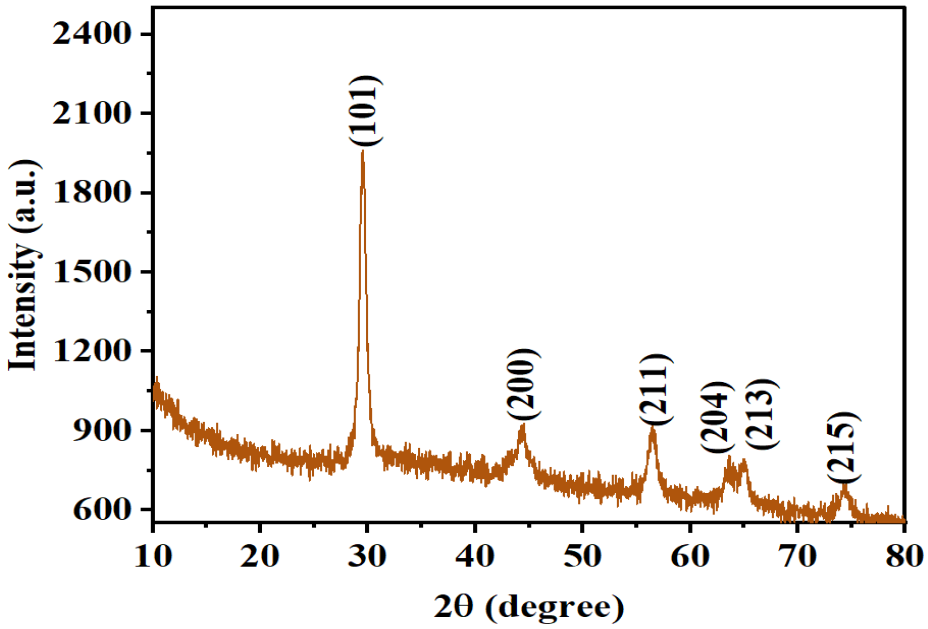

Figure 5.4: XRD pattern of green synthesized TiO_2-NPs

The EDS spectra in Figure 5.5 presents the elemental composition of TiO_2-NPs, confirming the presence of carbon (C), oxygen (O) and titanium (Ti). The emission of C in the TiO_2-NPs spectrum might have resulted from the leaf extract.

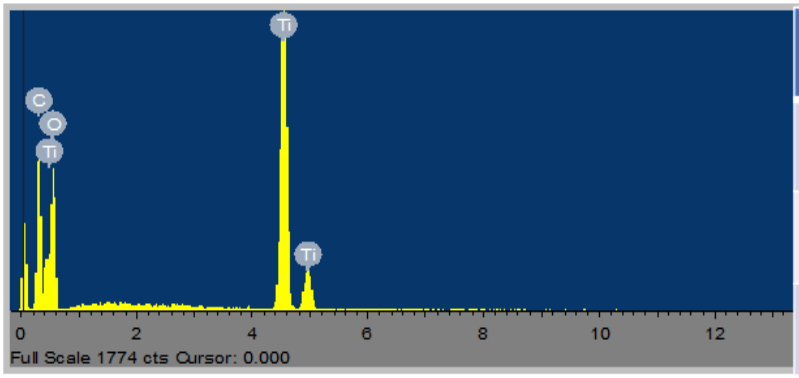

Elements	%
C	26.59
O	45.06
Ti	28.35

Figure 5.5: EDS image of green synthesized TiO_2-NPs

TEM micrograph of green synthesized TiO_2-NPs as presented in Figure 5.6 revealed the shape of TiO_2-NPs to be spherical with some agglomeration of the particles in the cluster. The agglomeration was observed, which was due to the greater influence of the leaf extract.

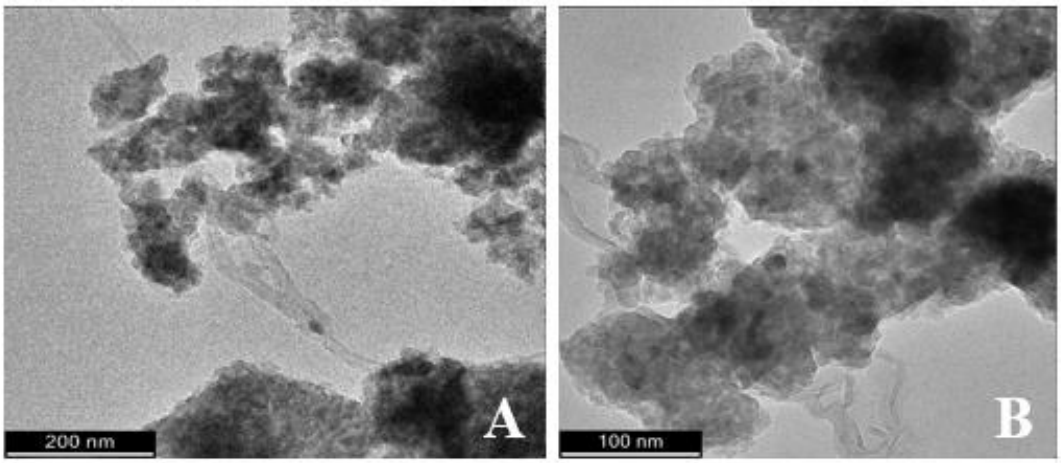

Figure 5.6: TEM images for green synthesized TiO_2-NPs

5.1.1.2 Electrochemical behaviour of Electrodes

(a) Characterization of electrodes using Cyclic voltammetry

CV was used to investigate the charge transport properties of the bare and modified electrodes (GCE, GCE/ TiO_2-NPs and GCE/TiO_2-NPs-nafion) in PBS (Figure 5.7 A) and in a redox probe solution of $[Fe(CN)_6]^{3-/4-}$ prepared in 0.1 M PBS, pH 7 shown in (Figure 5.7 B) at a scan rate of 25 mV/s. Figure 5.7 B shows the CV responses at the electrodes with a decreased peak current noticed at GCE/TiO_2-NPs-nafion in contrast to other electrodes, suggesting an electron-withdrawing effect between the electrode and the redox probe species due to the blocking of electrode surface area by nafion film (Buzid *et al.* 2018). However, based on the attractive properties of TiO_2-NPs, such as lager surface area, strong adsorptive ability, excellent catalytic activity and superior selectivity amidst interfering species, TiO_2- NPs with nafion as anchoring agent was used for the detection of EFV. (Kumaravel and Chandrasekaran 2011).

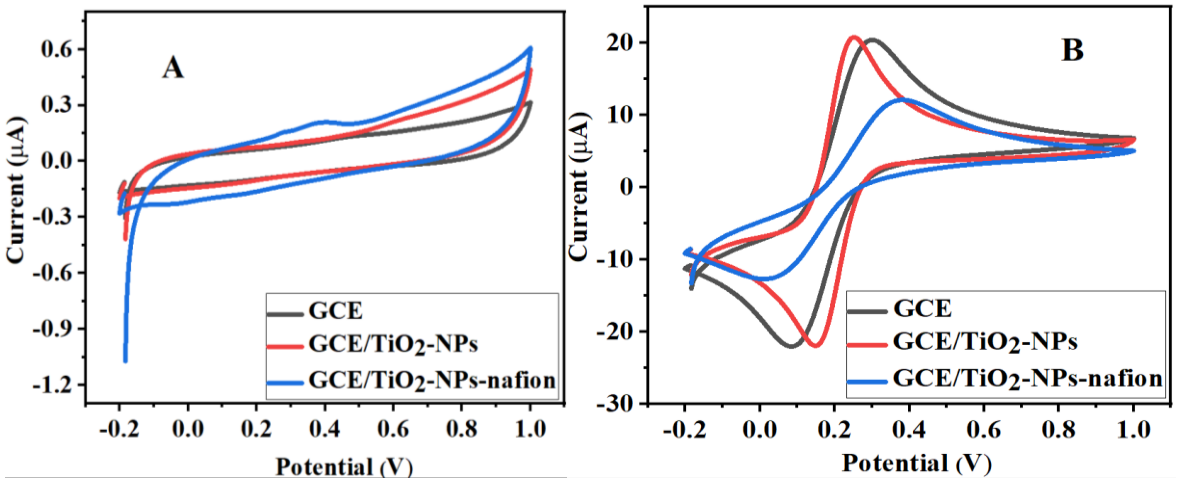

Figure 5.7: CVs obtained in (A) 0.1 M PBS and (B) in 0.1 M PBS at pH 7 containing 5 mM of [Fe $(CN)_6]^{3-/4-}$ at 25 mV/s scan rate

Table 5.1 summarizes the CV parameters including peak-to-peak separation (ΔEp), ratio of anodic and cathodic peak current (I_{pa}:I_{pc}), active surface area (A), oxidation and reduction peak potential (E_{pa} and E_{pc}) and peak currents recorded at the electrodes. The I_{pa}/I_{pc} values were approximately unity suggesting a reversible electrochemical process. The ΔEp suggests a more sluggish electron transport process at GCE/TiO_2-NPs-nafion. The active surface area values of the electrodes were estimated using Randle's Sevcik equation 5.1.

$$\boldsymbol{I_p = (2.69 \times 10^5) n^{3/2} A C D^{1/2} V^{1/2}} \qquad 5.1$$

Where, ΔE, R, and T represent the peak potential separation, gas constant and temperature accordingly while I_p, n, *A D*, *C* and *V* represent the peak current (amperes), number of electrons transferred, the surface area of the electrode in cm^2, the concentration of [Fe $(CN)_6]^{3-/4-}$ solution in mol/cm^3 and *v* is the scan rate in V/s, accordingly.

Table 5.1: Summary of CV parameters recorded for the bare and modified electrodes in 5 mM Fe $(CN)_6]^{3-/4-}$

Electrodes	E_{pa} (V)	I_{pa} (µA)	E_{pc} (V)	I_{pc} (µA)	E_{pa}-E_{pc} (Δ*E*, V)	I_{pa}/I_{pc}	*A* (cm^2)
GCE	0.2949	20.361	0.0874	-22.000	0.2075	-0.9255	0.0017
GCE/TiO_2-NPs	0.2510	20.770	0.1387	-21.697	0.1123	-0.9572	0.0018
GCE/TiO_2-NPs-nafion	0.3511	11.749	0.0288	-12.5823	0.3223	-0.9337	0.0010

(b) Characterization of electrodes using EIS

The interfacial charge transfer properties of the electrode materials were measured using EIS in $[Fe(CN)_6]^{3-/4-}$ redox probe solution prepared in 0.1 M PBS, pH 7. Nyquist plots achieved for the different electrodes at a fixed potential of 0.2 V in the frequency range of 0.1 Hz to 100 kHz are depicted in (Figure 5.8 A) while (Figure 5.8 B) is the equivalent circuit applied in the fitting of EIS data. R_s, R_{ct}, W and Q represent the solution resistance, charge transfer resistance, which is reflected by the semi-circle, Warburg, represented by the semi-infinite straight line and assigned to the diffusion pathway of the electrodes, and constant phase element accordingly. A high R_{ct} value was recorded at GCE/TiO_2-NPs-nafion electrode, suggesting a resistance to charge electron transport property at the electrode.

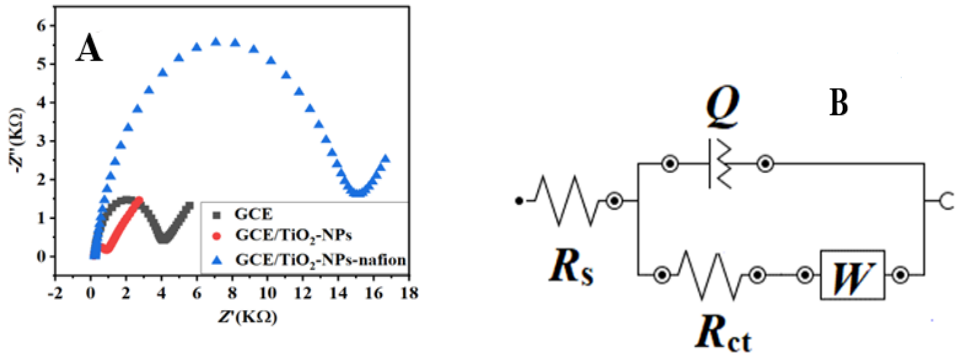

Figure 5.8: (A) Nyquist plots in 5 mM redox probe at the unmodified and modified electrodes, (B) Electrical equivalent circuit for the electrodes ([R(Q[RW)]).

Table 5.2 summarises the parameters of impedimetric data with Y^o connoting the magnitude of Q and n as the deviation. The values of n indicate the behaviour of electrodes as a capacitor, inductor or insulator when n is 1, −1 or 0 properly, depending on the homogeneity of the surface of the electrode (Uwaya, Wen and Bisetty 2022). The n values at all the electrodes are less than one, indicating a pseudo capacitive behaviour of the electrodes.

Table 5.2: EIS data obtained on different electrodes in 5 mM $[Fe(CN)_6]^{3-/4-}$ solution at +0.2 V fixed potential.

Electrode	R_s (Ω)	R_{ct} (Ω)	Y^0 (μΩ*S^n)	N	χ^2
GCE	172.31 (2.74)	3765 (2.26)	0.94 (11.29)	0.85 (1.54)	0.3610
GCE/TiO_2-NPs	176.64 (2.04)	1279 (2.23)	1.50 (13.67)	0.85 (1.86)	0.2244
GCE/TiO_2-NPs-nafion	217 (1.22)	14179 (1.25)	1.04 (3.74)	0.840 (0.57)	0.0896

(c) Effect of scan rate variation

To understand the type of electrode reaction the effect of scan rate variation on the peak potential and current of the redox probe at the GCE/TiO_2-NPs-nafion electrode was studied to understand the type of electrode reaction. Figure 5.9 A shows the recorded CV results at different scan rates in the range of 25 to 200 mV/s. An increase in the scan rate with a redox peak current and shifting of peak potentials of the redox probe was noticed. The relationship between peak current versus square root of scan rate ($v^{1/2}$), and log of peak current versus log of scan rate (v) (Figure 5.9 B-C) displayed an acceptable linear plot with a 0.999 correlation coefficient (R^2) value, suggesting a diffusion-controlled electrode reaction (Hareesha and Manjunatha 2021). Figure 5.9 C shows the slope of an ideal diffusion-controlled electrode process with a value that is close to 0.5.

The plot of peak current (I_{pa} and I_{pc}) versus scan rate (v) depicted in Figure 5.9 D revealed a linear pattern with a regression coefficient of 0.99. based on the slope value of Figure 5.9 D, the electrochemical surface coverage concentration (Γ) of the redox probe was estimated to be 1.49×10^{-3} mol/cm^2 on applying equation 5.2.

$$\boldsymbol{I_p = \frac{n^2F^2\Gamma Av}{4RT}} \qquad 5.2$$

The investigation of the apparent number of electrons (n) involved and the charge transfer coefficient (α) of the GCE/TiO_2-NPs-nafion electrode was conducted using the congruent changes in the redox peak potential (anodic and cathodic peak potentials) of Figure 5.9 A as a function of the logarithm of scan rate. Figure 5.9 E parades the plot of peak potentials versus the logarithm of scan rates represented with two resulting linear slopes equal to $\frac{-2.3RT}{\alpha nF}$ and $\frac{2.3RT}{(1-\alpha)nF}$, corresponding to cathodic and anodic peaks according to (Laviron 1979). Based on the slope and employing the simultaneous equation, n and α were found to be 0.819

and 0.51, respectively. The obtained value of α was adjacent to 0.50 for an ideal diffusion-controlled reaction.

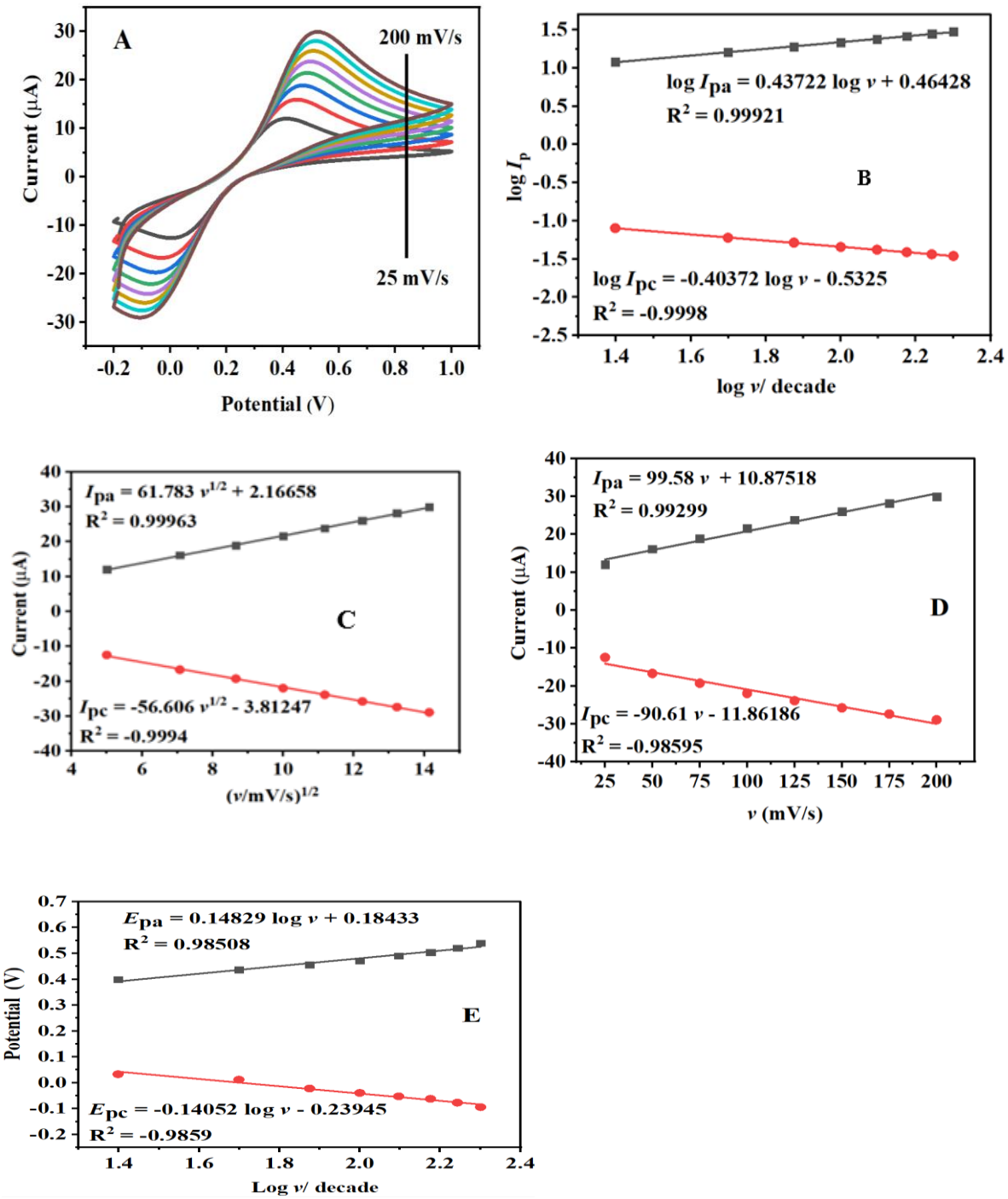

Figure 5.9: (A) Cyclic voltammograms in 5 mM $[Fe(CN)_6]^{3-/4-}$ solution at various scan rate (25–200 mV/s) on GCE/TiO_2-NPs-nafion electrode. linear plots of (B) log Ip versus log v (C) *I*p versus $v^{1/2}$ (D) Ip versus scan rate versus and (E) Ep versus log of v.

(d) Effect of pH solution optimization on EFV

The effect of supporting electrolyte pH solution on the sensitivity of the GCE/TiO_2-NPs- nafion electrode to 47.6 µM EFV was examined using CV, at 25 mV/s within a potential window of -0.2 to 1.4 V in pH ranging from 5 – 8.5 Figure 5.10 A. The choice of the pH range was based on the physiological pH (7.35 -7.45). The optimal current was obtained at pH 7 Thus, pH 7 was used all through the study. Figure 5.10 B presents the CV response in PBS alone at a scan rate of 25 mV/s at GCE/TiO_2-NPs- nafion electrode.

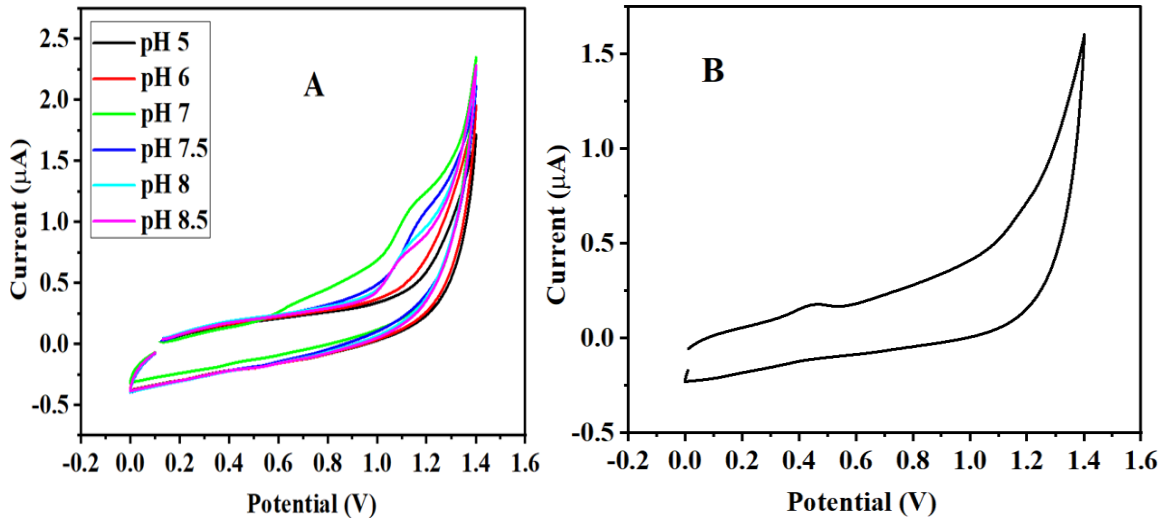

Figure 5.10: (A) Cyclic voltammograms in 0.1 M PBS at pH ranging from 5 – 8.5 containing 47.6 µM EFV and (B) in PBS only on at GCE/TiO_2-NPs-nafion at 25 mV/s

(e) Cyclic voltammetric detection of EFV bare and modified electrodes

The electrochemical behaviour of 47.6 µM EFV on the GCE, GCE/TiO_2-NPs and GCE/TiO_2-NPs-nafion electrode surfaces were examined using CVs TiO_2-NPs modified electrode was coated with nafion to prevent electrode fouling and improve the catalytic activity of the TiO_2-NPs towards EFV. The CVs of 47.6 µM EFV in 0.1 M PBS at 25 mV/s with a peak potential of 1.2 V on GCE and GCE/TiO_2-NPs-nafion, and 1.1 V on GCE/TiO_2-NPs are shown Figure 5.11. The result suggests the electrocatalysis of EFV to be an irreversible oxidation reaction which is similar to the previous literature report (Thapliyal *et al.* 2015). The amplified peak current observed at GCE/TiO_2-NPs-nafion electrode indicates an improved electrocatalytic

capability of TiO_2-NPs nafion for oxidation of EFV in the presence of nafion with a rapid rate of electron transport and high current sensitivity.

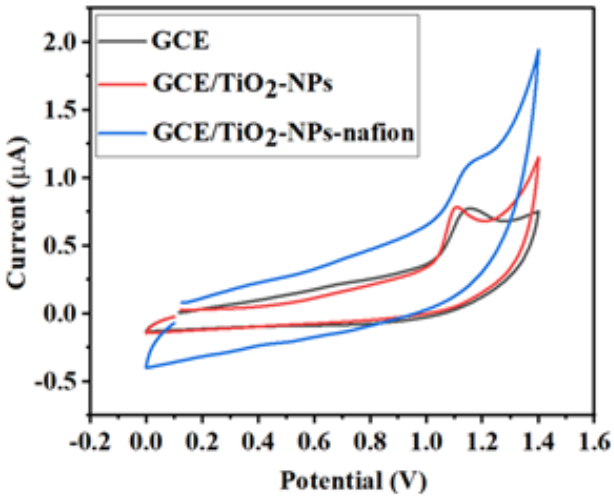

Figure 5.11: Cyclic voltammograms at 25 mV/s obtained at the bare and modified GCEs in 0.1 M PBS at pH 7 containing 47.6 µM EFV

(f) Electrochemical impedimetric detection of EFV bare and modified electrodes

To gain an insight into the electron transfer mechanism and the behaviour of the electrode-electrolyte interface during the oxidation of 47.6 µM EFV. Figure 5.12 A shows the Nyquist plots acquired at the electrodes while (Figure 5.12 B) denotes the Randle's circuits ([R(QR)]) used in the fitting of EIS data after several iterations of the circuits. The parameter obtained on fitting the EIS Nyquist plots are presented in Table 5.3, the EIS fitting confirmed the successful values in parenthesis and the chi square values (χ^2). The lowest R_{ct} value was achieved at GCE/TiO_2-NPs-nafion, which agrees with the CV measurements. The summary of EIS data of the electrode is presented in Table 5.3. The n values at all the electrodes are less than one, indicating a near capacitive behaviour of the electrode-electrolyte interface towards electro-oxidation of EFV.

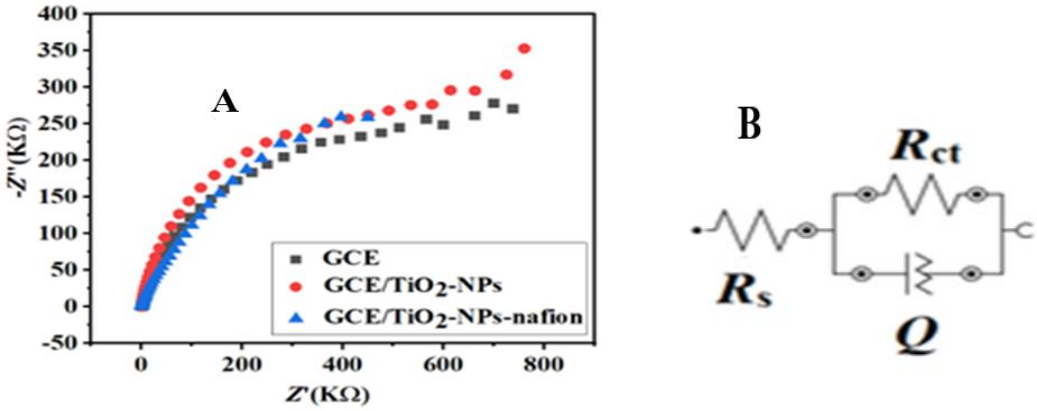

Figure 5.12: (A) Nyquist plots obtained at the bare and modified GCEs in 0.1 M PBS at pH 7 containing 47.6 µM EFV. (B) is the equivalent circuit-[R(RQ)] for the electrodes.

Table 5.3: Impedance data obtained for electrodes in 47.6 µM EFV at a fixed potential of 1.2 V (vs Ag/AgCl, standard KCl). Results are represented in parenthesis percentage errors of the data fitting.

Electrodes	Rs (Ω)	Rct (KΩ)	Y (µΩ*S^n)	N	χ^2
GCE	263(4.41)	712 (3.37)	0.36 (3.56)	0.76 (0.61)	0.42927
GCE/TiO_2-NPs	257(4.32)	671 (4.31)	0.27(5.10)	0.86 (0.81)	0.8977
GCE/TiO_2-NPs-nafion	222(5.22)	593 (7.17)	1.14 (4.58)	0.73 (0.92)	0.9142

Literature reports that the oxidation reaction of EFV involved one electron transfer (n), thus the number of protons that are involved in the reaction is one (Thapliyal *et al.* 2015). The electrooxidation of EFV at GCE/TiO_2-NPs-nafion is a one-electron and one-proton process. Based on the literature report and the DFT calculations performed, a possible reaction mechanism for the oxidation of EFV is proposed in Scheme 2.

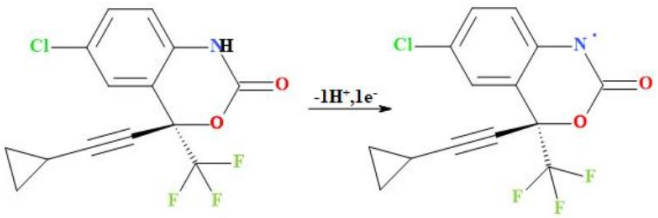

Scheme 2: Proposed reaction mechanism for EFV oxidation on GCE/TiO_2-NPs-nafion electrode

(g) Analytical performance of GCE/TiO_2-NPs-nafion electrode

The DPV for different concentrations of EFV measured within a 0.8 and 1.4 V potential window is shown in Figure 5.13. The oxidation peak current for EFV decreased with an increase in concentration from 4.54 – 18.7 µM. The detection limit (LOD) and quantification (LOQ) were estimated based on the relationship $\mathrm{LOD} = \frac{3\mathrm{SD}}{\mathrm{m}}$; $\mathrm{LOQ} = \frac{10\mathrm{SD}}{\mathrm{m}}$, where SD is the standard deviation of the intercept of y coordinates from the line of best fits and m is the slope of the same line. The calculated values of LOD and LOQ of GCE/TiO_2-NPs-nafion in EFV were found to be 0.01 and 0.03 µM, respectively. Table 5.4 shows the comparison of the LOD obtained with other EFV sensors.

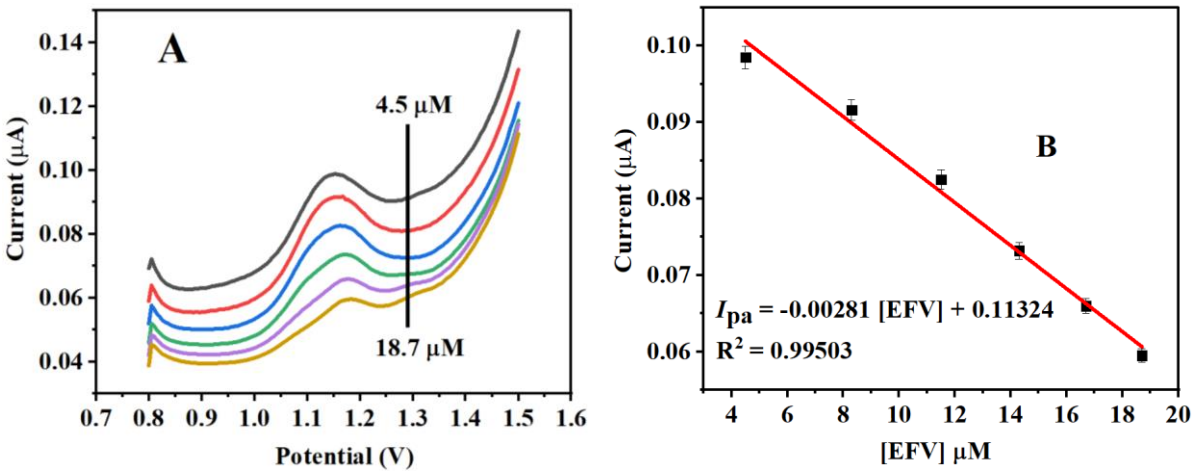

Figure 5.13: (A) GCE/TiO_2-NPs-nafion response to increasing EFV concentrations measured by DPV. (B) Linear plot of Ipa against concentrations (4.54 – 18.7 µM) in PBS.

Table 5.4: Comparison with other sensors

Electrodes	Methods	Supporting electrolyte	Peak Potential mV	Linearity (µM)	LOD (µM)	Ref
PGE[a]/dsDNA[b]	AdSV	pH 7.2 PBS	1001	6.33 –7.60	1.9	(Dogan-Topal, Uslu and Ozkan 2009)
Thin Hg[c]-Film	AdSV	2.0×10^{-3} NaOH	-280		0.03	(Castro *et al.* 2011)
ErGO[d]-Pt[e]/Nafion/EPPG[f]	SWV	PBS pH 7.2	1160	0.05 –150	1.8×10^{-3}	(Raj *et al.* 2017)
NiO[g]–ZrO_2[h]/GCE	DPV	PBS 7.2	1200	0.01 – 10	1.36×10^{-3}	(Thapliyal *et al.* 2015)
GCE/TiO_2-NPs-nafion	DPV	0.1 M PBS, pH 7	1010	4.5 – 18.7	0.01	This work A developed sensor consists of green synthesised TiO_2-NPs with linear dynamic range of 4.5 to 18.7 µM with 0.01 µM limit of detection recorded on the electrode using DPV

Note a =Pencil graphite electrode, b = anti-double strande, c = Mercury film, d = Reduced graphene oxide, e = Platnium, f =Edg plane pyrolytic, g = Nickel oxide, h= Zirconia

(h) Real sample analysis

The practical utility of the designed sensor for the determination of EFV in real samples was evaluated with a pharmaceutical sample (Cipla efavirenz tablet) by the standard addition method using DPV. The developed sensor displayed satisfactory recovery from the range of 97 – 106% with RSDs in the range of 9.9 – 10.3%. The summary of the obtained results is presented in Table 5.5.

Table 5.5: Recovery and RSD of EFV on GCE/TiO_2-NPs-nafion in Cipla EFV sample

Serial number	Amount added	Amount found	Recovery (%)	RSD n = 3
1	8.3	8.8	106	9.9
2	11.5	11.2	97	10

(i) Interference and reproducibility study

In order to test the selectivity of the developed sensor, the influence of several typical interfering species on the determination of 47.6 µM EFV in PBS pH 7.0 was evaluated using DPV and chronoamperometry. Figure 5.14 A shows the DPV recorded in 0.1 M PBS

containing mixtures of EFV, ascorbic acid (AA) and uric acid (UA) of the same concentrations (47.6 µM) for the first voltammogram, and 90 µM for AA in the second voltammogram in red on GCE/TiO_2-NPs-nafion electrode. Two prominent peaks for UA, 0.55 V and EFV, 1.19 V and a suppressed signal for AA were noticed for the first voltammogram in black. The second DPV voltammogram displayed three

distinct peaks with peak potentials for AA, UA and EFV found at 0.31, 0.59 and 1.22 V accordingly. The peak potential separation between AA and UA, UA and EFV and AA and EFV were estimated to be 0.28, 0.63 and 0.91 V respectively. The results suggest the possibility of detecting EFV in the presence of possible interfering species. Figure 5.14 B shows the chronoamperometric current signals of EFV, AA and UA at a working potential of 1.0 V and interval of 40 s. EFV (47.6 µM) signal was determined before and after adding 1 mL of AA (90.9 µM) and 0.5 mL UA (47.6 µM) into 10 mL PBS. The result shows non-interference of EFV signal after successive injection of AA and UA, indicating selectivity of the electrode.

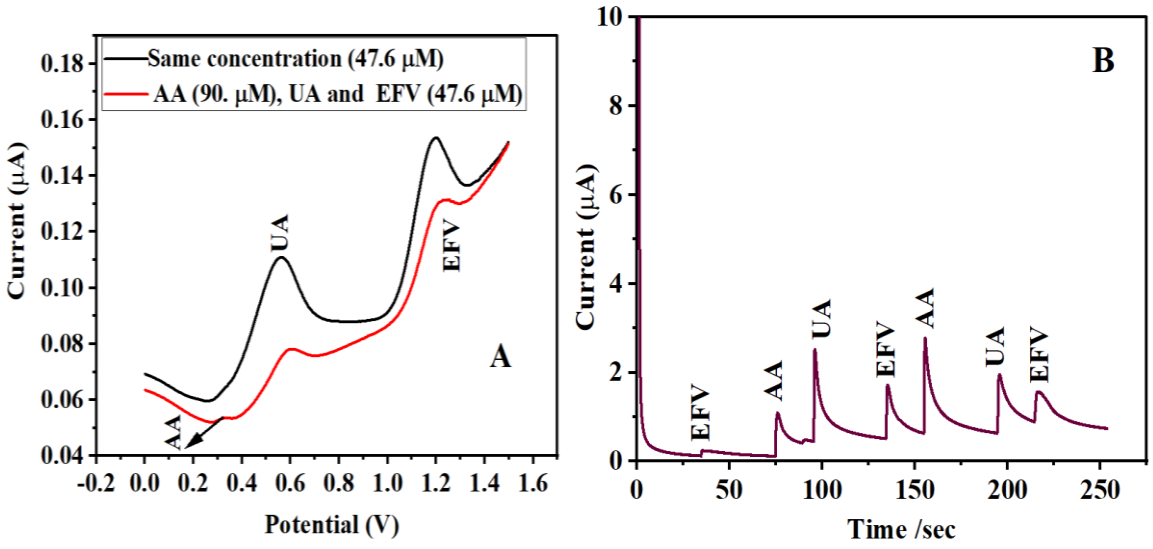

Figure 5.14: (A) The simultaneous determination of 47.6 µM EFV, AA and UA on GCE/TiO_2-NPs-nafion by DPV, (B) Chronoamperometric curve of GCE/TiO_2-NPs-nafion in pH 7 PBS containing EFV, AA and UA

(j) Repeatability, reproducibility and storage stability of the result

The reproducibility of GCE/TiO_2-NPs-nafion was examined by analysing the DPV responses of three independent electrodes in the 47.6 µM EFV and the RSD was found to be 5.4% demonstrating acceptable reproducibility of the designed sensor for EFV detection. The

electrochemical sensor for 6 repetitive cyclic voltammetry was investigated for repeatability in 47.6 µM EFV (Figure 5.15) An approximate 14.8% decrease in the oxidation current was observed. Using DPV in 47.6 µM EFV This could be ascribed to saturation of electrode, and possibly electrode fouling. The electrode was studied for storage stability using DPV in 47.6 µM EFV for 7 days with the electrode stored in the refrigerator when not in use at 4 °C. After 7 days 29.25% of current was recorded using an electrode stored in the refrigerator at 4 °C. Results indicating that the constructed sensor has demonstrated satisfactory storage stability.

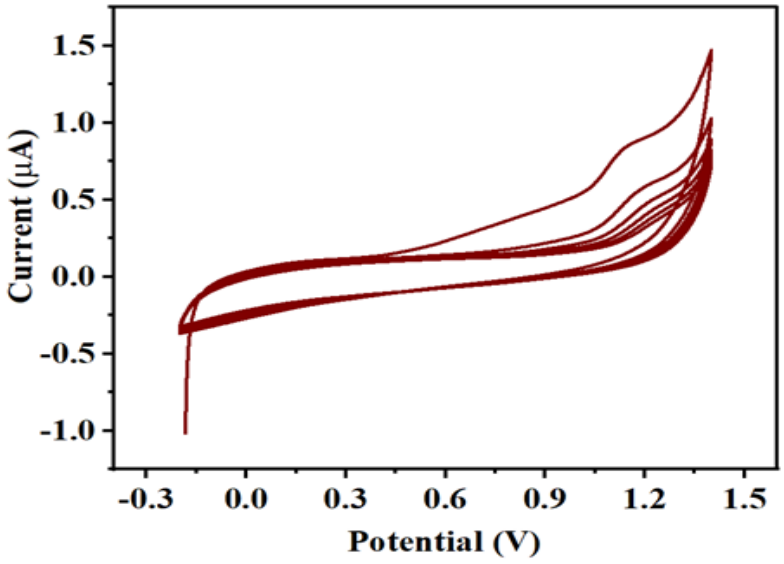

Figure 5.15: The repeatability of GCE/TiO_2-NPs-nafion towards 47.6 µM EFV

5.1.2 COMPUTATIONAL SECTION

5.1.2.1 HOMO-LUMO band gap energy

The frontier molecular orbital calculation helps to determine the significant atom or part of a molecule for reduction, oxidation or redox reaction (Pamuk *et al.* 2013). Therefore, to support the oxidation mechanism of EFV in a more accurate way and to evaluate the chemical reactivity of EFV, the HOMO-LUMO of EFV was computed from the DFT calculation. It can be seen from Figure 5.16, that both the HOMO and LUMO electron density is distributed mainly on the benzoxazine ring with the lowest energy gap, ΔE_{gap}= 5.171 eV making it more reactive, suggesting that the benzoxazine ring as the main active site of EFV. The HOMO orbital energies describe the ability of molecules to donate electrons in general. The smaller value of Egap in our situation provides a stronger reactivity for removing an electron from the highest

occupied orbital to the lowest unoccupied orbital, implying that oxidation processes are more likely to occur because oxidation reactions tend to displace electrons from the HOMO. Therefore, less energy is required for the oxidation (loss of electrons) in comparison to the reduction (gain of electrons) reactions. Similarly, LUMO+1 exhibited almost similar distribution of electron density. In contrast, LUMO+2 and HOMO-2 illustrated electron density over the whole molecule with only a small part is localised on the oxazine ring for HOMO-2 with the highest energy gap, ΔE_{gap}= 7.325 eV. The alkyne, cyclopropyl, and carbonyl functionality of the oxazine ring were preferred locations for the HOMO+1 electron density.

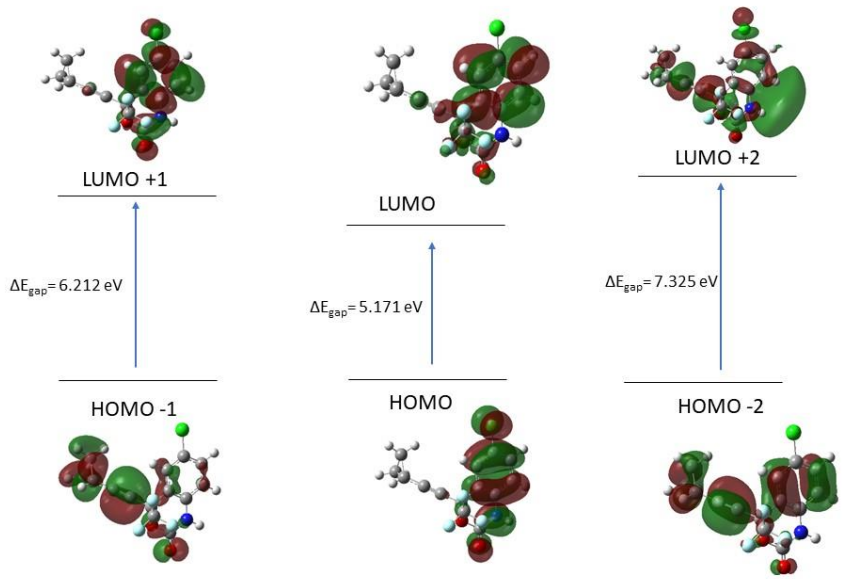

Figure 5.16: Frontier molecular orbitals on optimized molecular structure of EFV computed at B3LYP/6-311+G

5.1.2.2 Monte Carlo Simulations

In order to assess the interaction patterns of EFV, the simulated annealing job task was applied using the adsorption locator module of the Monte Carlo (MC) simulations to the substrates GCE/TiO_2-NPs and GCE/TiO_2-NPs-nafion loaded with EFV as an adsorbate molecule. For finding a low energy adsorption site, a MC-based function was utilized to find the most favourable configuration. Table 5.6 depicts the lowest adsorption energy values for the adsorbate-substrate system modelled in a systematic way under periodic boundary conditions

Table 5.6: Calculated adsorption energy for the adsorbate-substrate systems

Substrate-Adsorbate	Adsorption Energy/kcal mol
GCE/TiO_2-NPs-EFV	-20.455
GCE/TiO_2-nafion-EFV	-23.962

Clearly, the adsorption energies process is exothermic and spontaneous since all adsorbates are negative, indicated when the relaxed adsorbate components are adsorbed on the substrate, suggesting that TiO_2-NPs strongly interact with the GCE substrate. The presence of nafion in GCE/ TiO_2-NPs-nafion-EFV interaction is supported by more highly negative adsorption energy (-23.962 kcal/mol) in contrast to a higher value (-20.455 kcal/mol) in the absence of nafion.

As illustrated in (Figure 5.17 A-D), a comparison of the electrode systems was performed to examine the adsorption behaviour and energy differences in relation to electrode modification phases. The effect of intramolecular and intermolecular energies on the behaviour of nafion adsorption was investigated using these models.

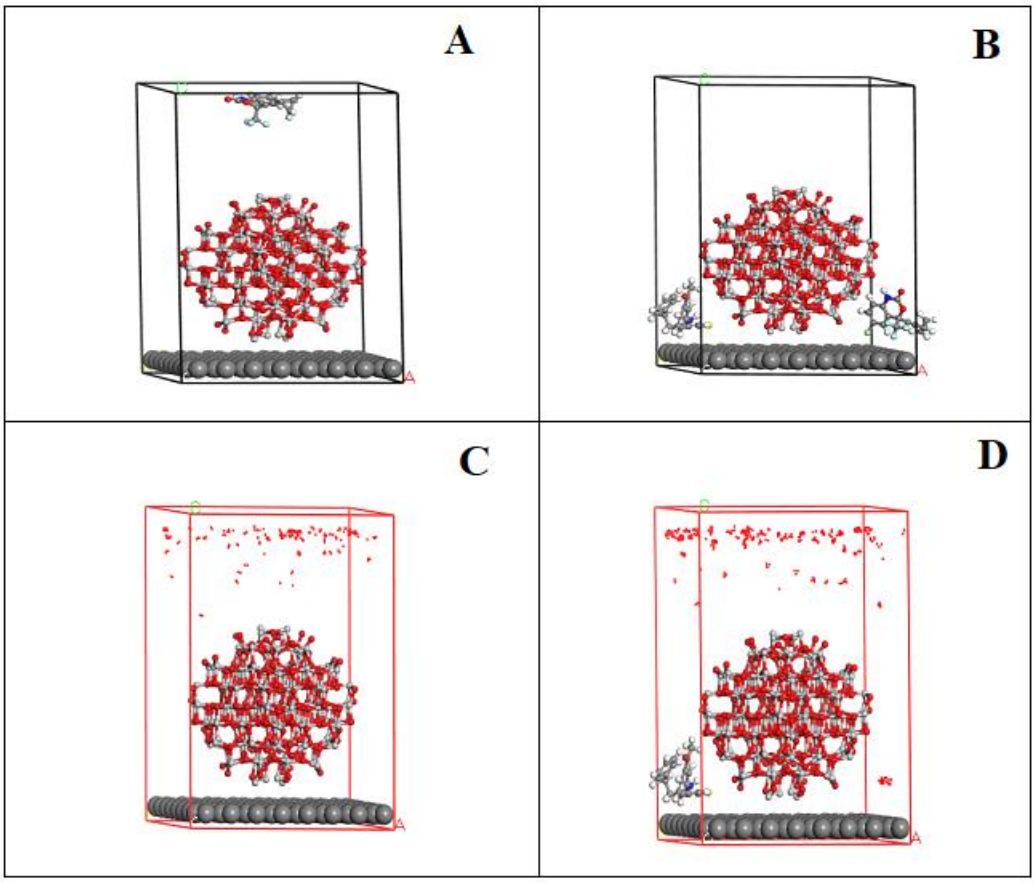

Figure 5.17: System conformations for (A) GCE/TiO_2-NPs-EFV and (B) GCE/TiO_2-NPs-nafion-EFV together with their respective distribution field maps (C) and (D) in a periodic cell.

In Figure 5.17 A, the EFV is located above the TiO_2-NPs surface in a planar fashion. This is attributed to the weaker van der Waals forces of interaction between EFV and the TiO_2-NPs surface. In contrast, nafion binds more strongly with the TiO_2-NPs (Figure 5.17 B), this interaction accounts for the lowering of the adsorption energy (-29.050 kcal/mol) and supports stronger adsorption of EFV with the GCE/TiO_2-NPs-nafion substrate. The verification has been confirmed by the favourable iso-surfaces or heat field maps depicted in (Figure 5.17 C and D), with the more likely adsorption areas revealed in red. Here, the "observed clouds" indicate the level of distribution fields of the adsorbed molecule/s location corresponding to the GCE surface.

5.1.3 CONCLUSION

A bioinspired green synthesised TiO_2-NPs modified electrode with nafion as an anchor agent was used to study the electrochemical conductivity of EFV. We demonstrated that the enhanced performance of the modified sensor can be attributed to nafion. According to the MC simulations, EFV interacts strongly with the GCE/TiO_2-NPs-nafion electrode, supporting the CV and EIS results. Based on the DFT calculations, the active sites of EFV could be predicted, leading to the proposed mechanism. In addition to its good selectivity and sensitivity, we observed a low detection limit for this sensor. A GCE/TiO_2-NPs-nafion electrode was successfully used to determine EFV in pharmaceutical samples with satisfactory recovery. It presents a new and convenient electroanalytical method for the detection of EFV in the absence of enzymes. This motivated us to investigate the photocatalytic activity of TiO_2-NPs on EFV, which is presented in the second case study.

5.2 CASE STUDY II

THE PHOTOCATALYTIC DEGRADATION OF EFV

In this study, spectroscopic and computational approaches were used to investigate the photocatalysis of EFV using TiO_2-NPs. Accordingly, the spectroscopic analysis of the EFV-TiO_2-NPs interactions were investigated using UV-visible spectrophotometry and TD-DFT calculations with the self-consistent reaction field (SCRF) model to account for the effect of the polarizable solvent (methanol) on the quantum system.

5.2.1 EXPERIMENTAL SECTION

5.2.1.1 UV-visible characterization

The UV-vis absorption spectrum of TiO_2-NPs, EFV and EFV-TiO_2-NPs were examined in the range of 200-800 nm as shown in (Figure 5.18 A-C). As discussed earlier, the observed band for TiO_2-NPs (Figure 5.18A) at 365 nm, similar to those reported in literature (Sethy *et al.* 2020). The experimental spectrum in (Figure 5.18 B) shows the presence of absorbance peaks at 250 and 294 nm which is expected for EFV. The 250 nm band is assigned to the carbonyl aromatics which are characterized by π-π^* transitions, while the band around 294 nm corresponds to a n-π^* transition state (Abou-Zied and Al-Shihi 2008; Shown, Ujihara and Imae 2010). According to literature the benzene ring is responsible for the π-π* electronic transitions and the auxochromic electron- donating amino and electron-accepting carbonyl moieties are responsible for the n-π* electronic transitions (Jordaan and Shapi 2017).

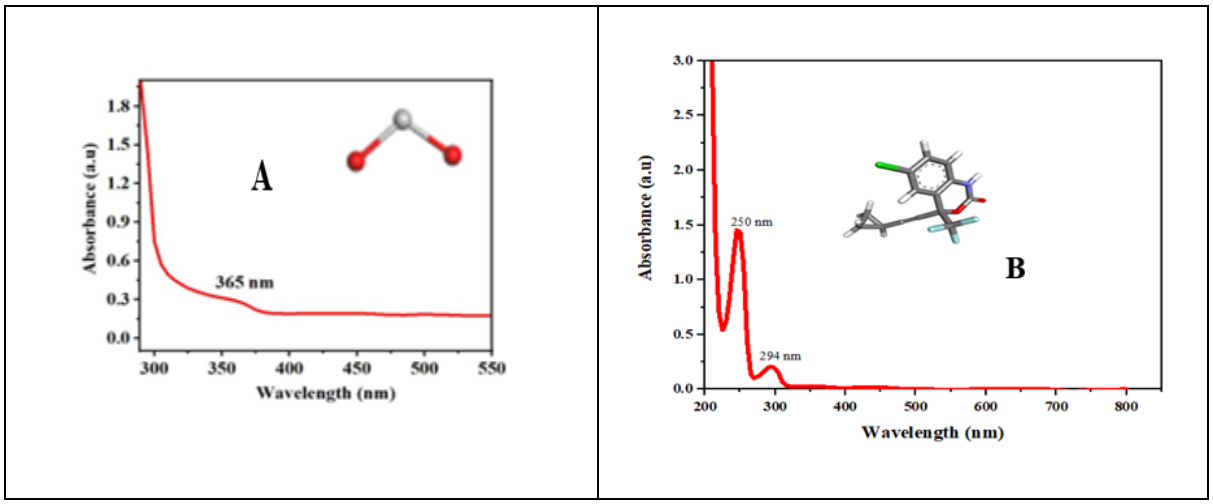

Figure 5.18: UV–vis spectra of (A) TiO_2-NPs (B) EFV in methanol

5.2.1.2 Optical band gap

The average band gap, E_g of EFV, TiO_2-NPs and EFV-TiO_2-NPs were evaluated from the absorption spectrum using the Tauc relation in equation 5.3:

$$\alpha h\nu = k(h\nu - E_g)^m \qquad 5.3$$

where α is the absorption coefficient, h is the Plank's constant, ν is the frequency of incident light, k is the optical constant and m is a constant. For m = ½, E_g in equation 5.3 is the direct allowed band gap (Fakhri and Ahmed 2019; Jawad and Ahmed 2020). The average band gap, E_g estimated from the intercept of the linear portion of the $(\alpha h\nu)^2$ vs hν plots as shown in Figure 5.19 are 3.43, 3.88 and 3.20 e*V* for EFV, TiO_2-NPs and EFV-TiO_2-NPs respectively. The slight disparity in the E_g values suggests the occurrence of probable interaction between EFV and TiO_2-NPs. The Eg value "3.88 eV of TiO_2-NPs is close to 3.75 eV of previous work (Mandal *et al.* 2019) and higher than the bulk TiO_2-NPs (3.2 e*V*), which could be linked to quantum confinement.

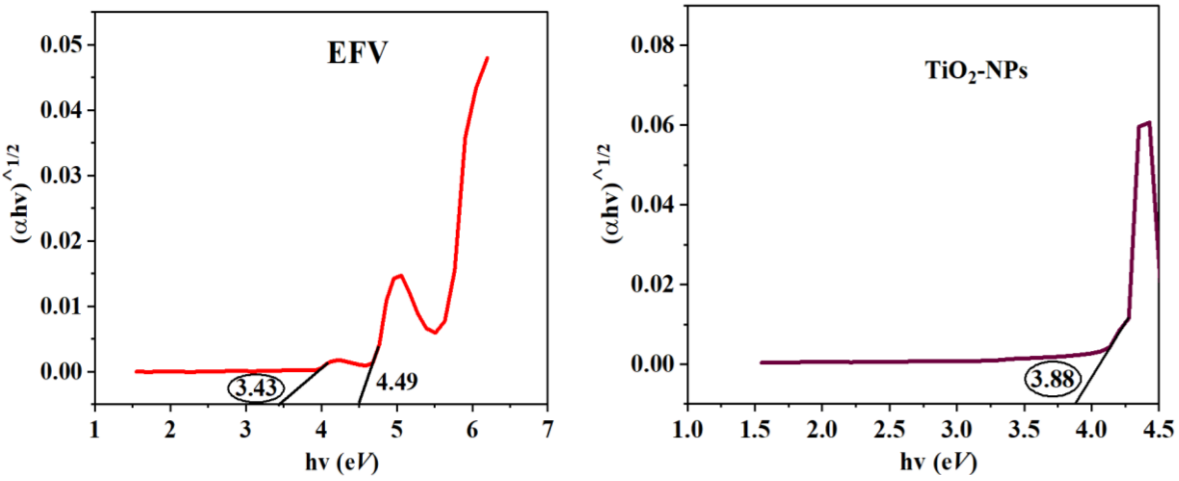

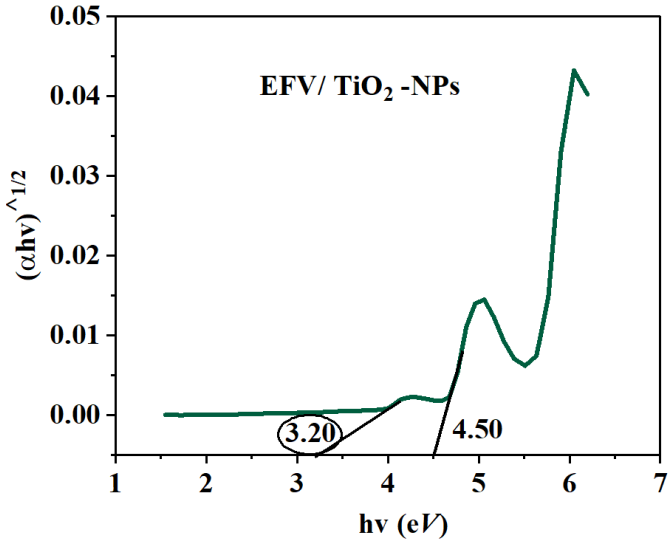

Figure 5.19: Tauc's plot for EFV, TiO_2-NPs and EFV-TiO_2-NPs

5.2.1.3 Photodegradation performance

Next, we used UV-vis spectrophotometry to investigate the effect of the biosynthesized TiO_2-NPs on EFV in the presence of methanol as a solvent, at a wavelength ranging from 200-800 nm as shown in (Figure 5.20 A). The main purpose of study was not to identify the degradation products, but to demonstrate the effects of TiO_2-NPs on EFV over time. Figure 5.20 A shows the absorbance spectra obtained for EFV-TiO_2-NPs at regular time intervals from 0 – 5 h. The noticeable shift in absorbance peaks in comparison with (Figure 5.18 A) demonstrates the interaction between EFV and TiO_2-NPs. Also, a significant decrease in the absorbance peaks with a corresponding increase in treatment times is evident (Figure 5.20 A), suggesting the degradation of EFV by TiO_2-NPs

We then analysed the degradation efficiency of EFV by measuring the concentration of EFV as a function of time and calculated using equation 5.4.

$$\% \textbf{ degradation} = \mathbf{1} + \frac{C_o - C_t}{C_o} \times \mathbf{100} \qquad 5.4$$

where C_o represents the initial concentration of EFV solution and C_t signifies concentration of EFV solution during irradiation. Figure 5.20 B indicate the increase in photodegradation

efficiency of EFV with increasing UV- visible exposure time, suggesting that longer exposure time is necessary for complete degradation. According to literature report, photocatalytic activity is dependent on availability of active species/sites also called holes (Mogomotsi *et al.* 2020). The mechanism of photodegradation involves the excitation of energized electrons when UV lights is incident on the photocatalysts resulting to the formation of holes or active sites. The holes interact with water molecules to give active radicals ·OH, which serve as redox agents while the excited electrons react with oxygen to form super peroxide radicals, $\cdot O_2$. The greater the availability of active sites the better the degradation efficiency. Therefore, it is presumed that more active sites were present at 5 h irradiation time, hence the highest degradation efficiency was recorded.

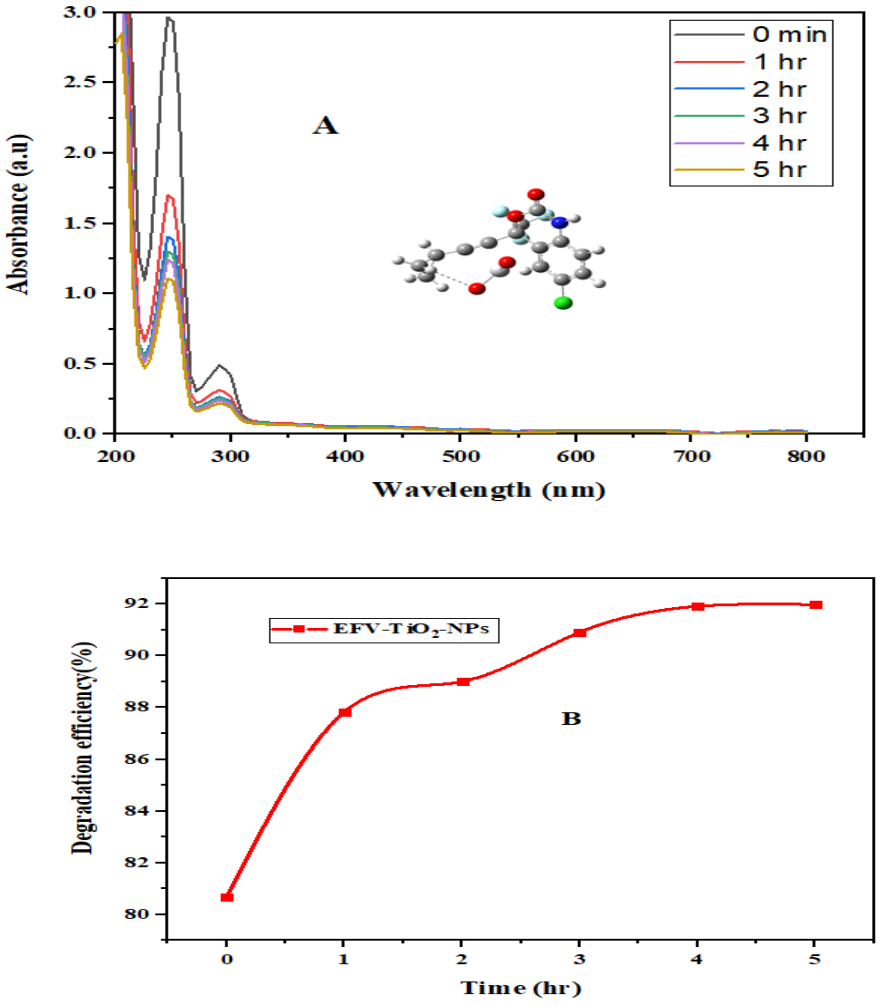

Figure 5.20: (A) UV–vis spectra interaction of EFV-TiO_2-NPs and (B) degradation efficiency of EFV-TiO_2-NPs.

5.2.2 COMPUTATIONAL SECTION

5.2.2.1 UV-visible characterization

TD-DFT was used to obtain the UV spectra (Safrany *et al.* 1999) calculations in gas phase and in methanol to explain some of the measured UV data for EFV and EFV-TiO_2-NPs. Density of state (DOS) diagrams were obtained using the GaussSum program (O'boyle, Tenderholt and Langner 2008) to compute the contributions of the molecular orbitals. The TD-DFT calculations in gas phase and in methanol were carried out using the B3LYP basis set and the 6-31+G* level of theory. The results showed that there are two main transitions for EFV as in Figure 5.20, which correlates with the experimental results. EFV was recorded in methanol showing a strong absorption band at approximately 270 nm and low intensity compared to gas phase.

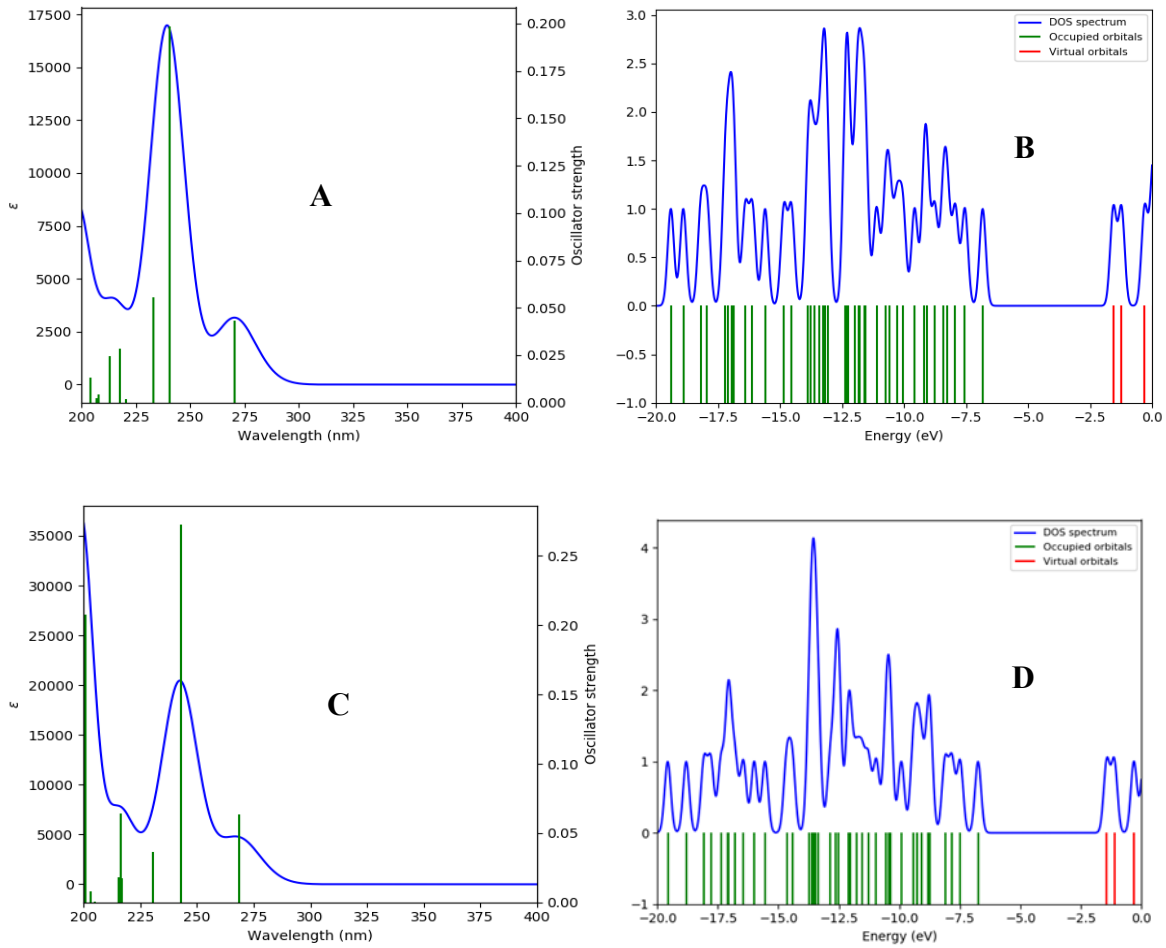

Figure 5.21: Calculated TD-DFT UV Spectra (A) and (B) DOS for EFV in gas phase; Calculated TD-DFT UV Spectra (C) and (D) DOS for EFV in methanol

The interaction for EFV and TiO_2-NPs were investigated the with comparison of gas phase interaction with that of methanol (Figure 5.21) shows that the excitation of EFV adsorbed on TiO_2-NPs, should lead to charge transfer from EFV to the CB of the semiconductor, which would cause light absorption from the UV towards the visible range 245-275 nm approximately while intensity remains the same.

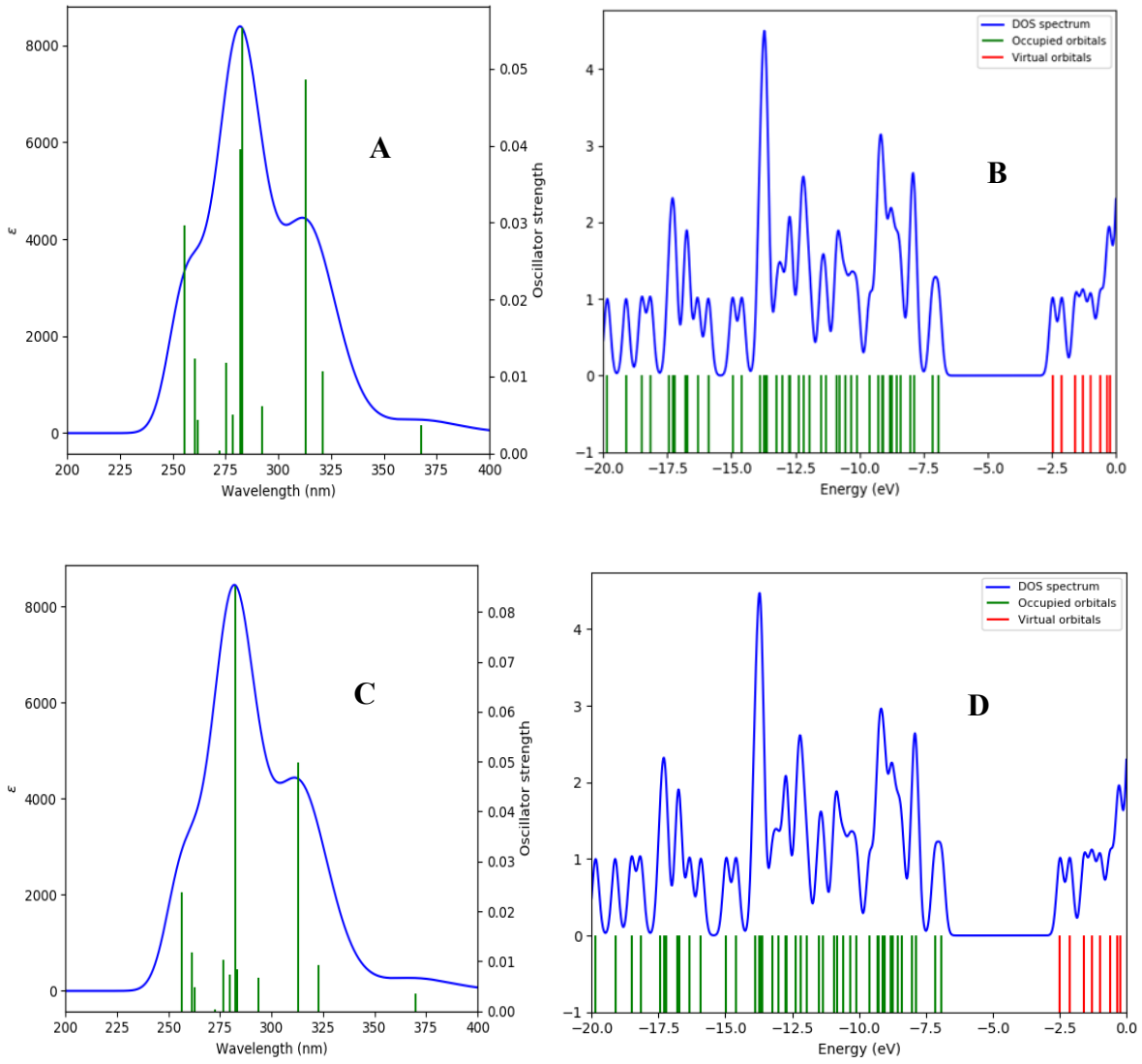

Figure 5.22: Calculated TD-DFT UV Spectra (A) and (B) DOS for EFV-TiO_2-NPs in gas phase; Calculated TD-DFT UV Spectra (C) and (D) DOS for EFV-TiO_2-NPs in methanol

TiO_2-NPs consists of the valence electronic configuration of Ti [$3d^2$; $4s^2$] and O [$2s^2$; $2p^4$], as shown Figure 5.21, TiO_2-NPs has a redshift and thus appears at longer wavelength due to the

highest occupied molecular orbital (HOMO) in the valence band formed by the hybridization of the 3d orbitals of Ti and 2p orbital of the oxygen. Furthermore, the bonding molecular orbital was mainly distributed between two oxygen of TiO_2-NPs, resulting in the nucleophilic property of TiO_2-NPs (Saha *et al.* 2013).

5.2.2.2 Interactions of EFV and TiO_2-NPs

The 3D optimized structure showing the interaction of EFV-TiO_2-NPs is shown below.

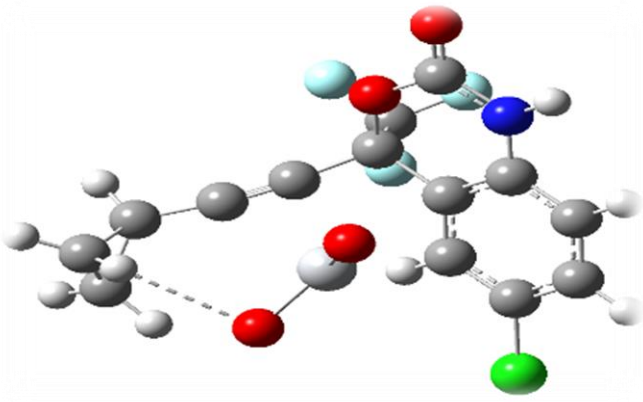

Figure 5.23: The geometry optimized EFV-TiO_2-NPs computed at B3LYP/6-31+G* level of theory (red, green, dark blue, pale blue, white, and grey, denotes the oxygen, chlorine, nitrogen, fluorine, hydrogen and carbon respectively).

A strong hydrogen bond formation is observed by the dotted lines (Figure 5.22) between the first oxygen atom (O1) of TiO_2-NPs and the hydrogen (H1) of the cyclopropane ring (O1---H1). This stabilizes the overall structure of EFV-TiO_2-NPs. TiO_2-NPs have under coordinated Ti atoms and a peculiar surface chemistry. These undercoordinated sites have a high reactivity towards oxygen-rich ligands due to their ability to fill the octahedral coordination sites. Functionalization with organic molecules provides TiO_2-NPs with specific binding sites.

Next, we obtained the HOMO-LUMO band gap energies of the EFV-TiO_2-NP complex shown in (Figure 5.23) with band gaps of -3.6049 to -5.7086 eV, which are sensitive to the DFT functional and basis set used. For that reason, the band gaps presented here have slight deviations from those reported. According to the results the distribution of molecular orbitals of HOMO, HOMO-1, HOMO-2, LUMO, LUMO+1, LUMO+2 and their energy gaps

computed with B3LYP/6-31+G* level of theory shed more light on the nature of EFV interaction with TiO_2-NPs by looking at the charge transfer interactions (Figure 5.23).

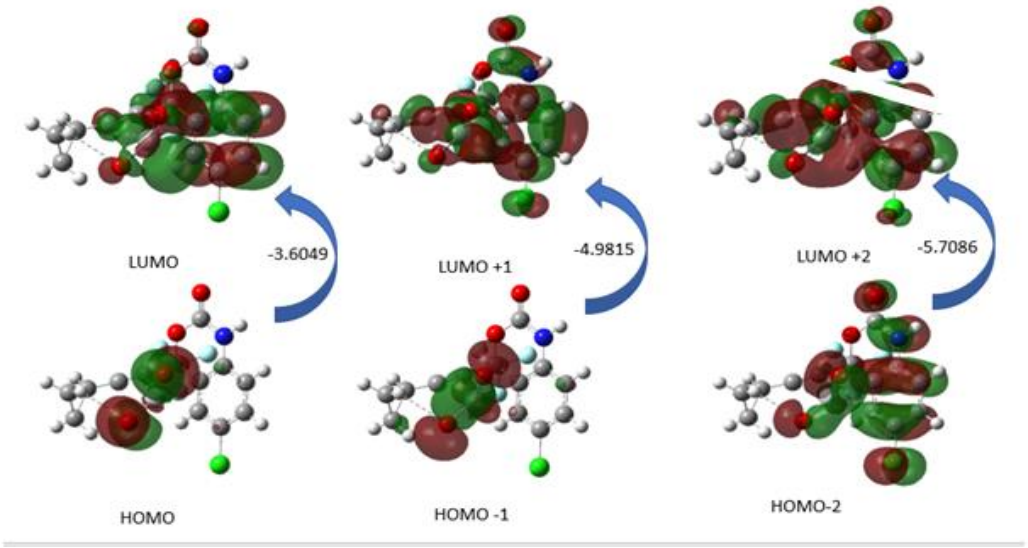

Figure 5.24: The atomic orbital compositions of the frontier molecular of the Interaction of EFV and TiO_2-NPs at B3LYP/6-31+G* level of theory

The HOMO-LUMO ($\Delta_{HOMO\text{-}LUMO}$) gaps values for the electronic band is ΔE_{gap}. The ΔHOMO-LUMO gap for the optimized TiO_2-NPs molecule is HOMO and LUMO ΔE_{gap} = -3.6049 eV; LUMO+1 and HOMO-1 ΔE_{gap} = -4.9815 eV and LUMO+2 and HOMO-2 ΔE_{gap} = -5.7086 eV. The HOMO and HOMO-1 is completely localized on the trifluoromethyl and two oxygen groups of Ti-O atoms, indicating a delocalized orbital within the benzene ring. whereas HOMO-2, LUMO, LUMO+1, LUMO+2 is completely localised on the trifluoromethyl and the benzene ring except on the cyclopropyl. EFV is described by a chromophoric benzoxazinone with hydrogen bonding (H-bonds) that undergoes a proton transfer process (van de Werken *et al.* 2014). EFV is also known to be surrounded by many positive regions rather than the negative regions, which makes it electrophilic reactive as opposed to nucleophilic reactive (Xu *et al.* 2018b). This indicates that EFV molecules are more prone to be adsorbed on the negative charge surface and can also undergo a possible proton transfer from the surface of the N-H group which interacts with the O atoms of a neighbouring band gap of the metal oxide, through a red shift of the adsorption band from the UV to the visible range.

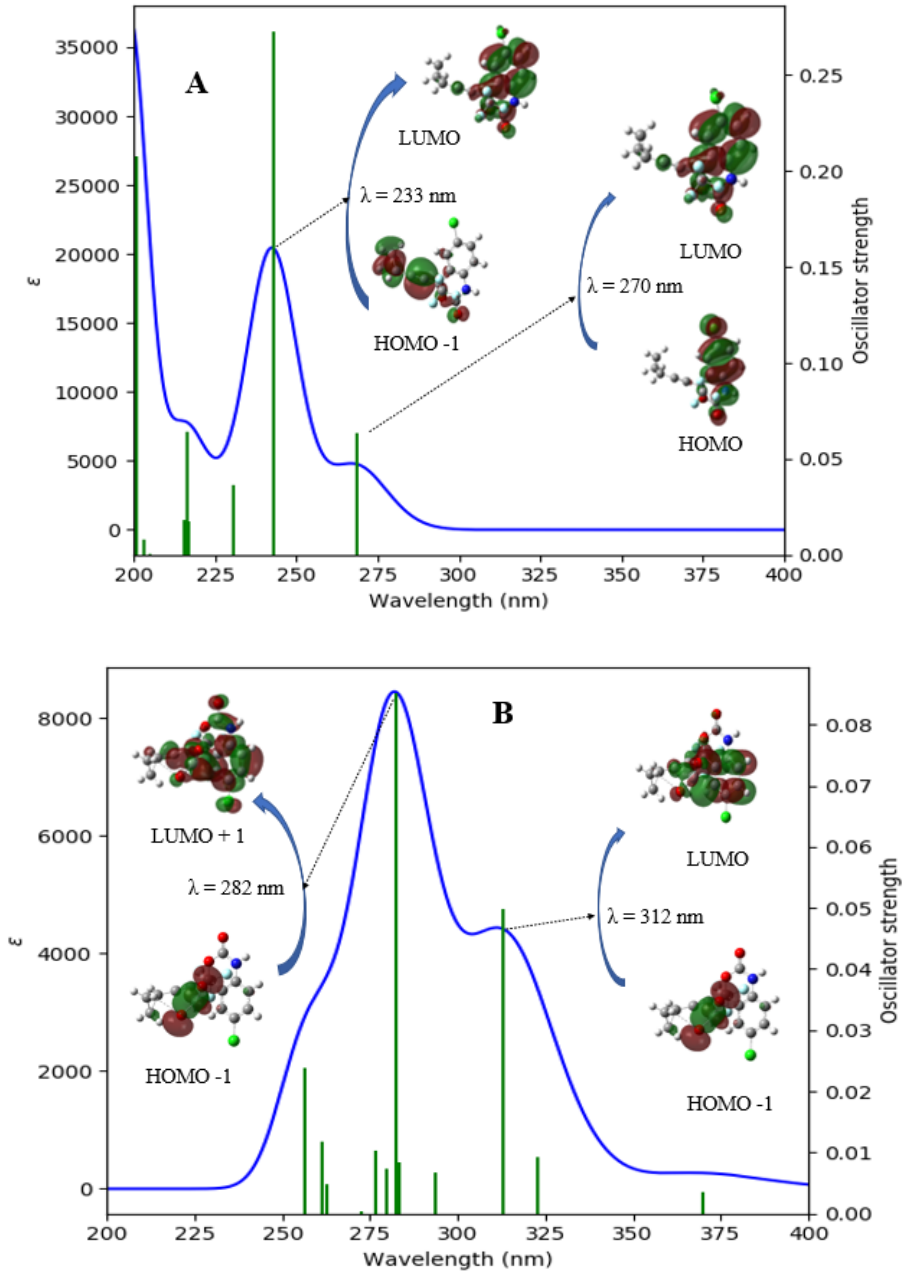

Figure 5.25: Calculated UV spectra for (A) EFV and (B) EFV-TiO_2-NPs in methanol using TD-DFT/B3LYP/6-31G* basis set. The inset shows the HOMO-LUMO plots at the calculated wavelengths.

In case of EFV in methanol, the inset in (Figure 5.24 A) shows the HOMO to LUMO electronic transition induced at a calculated value at 270 nm with 86% contribution. The electronic transition is due to non- bonding to anti-bonding (η to π*) and may be attributed to the carbonyl group. The other major electronic contribution of 76% is observed at a calculated value at 240 nm for the HOMO-LUMO +1 transition as shown in table 5.7. The electronic transitions are

due to bonding to anti-bonding (π-π*) and may be attributed to the benzene group. Figure 5.24 B shows a reduced peak absorbance for EFV-TiO_2-NPs as confirmed by a smaller corresponding oscillator strength. Table 5.8 shows the calculated adsorption to be 83% and 69% at 312 nm and 282 nm respectively for the major electronic contributions. Each corresponding to HOMO-1→LUMO and HOMO-1→LUMO-1 transitions respectively. The electronic transition is due to η to π* and may be attributed to the trifluoromethyl and the benzene ring group.

Next, the Gauss-Sum program was used to calculate the group contributions of the molecular orbitals and to prepare the density of states (DOS) spectrum in (Figure 5.25 A-B). The DOS spectrum provides a visual understanding of the HOMO – LUMO plots for EFV and EFV-TiO_2-NPs in the presence of methanol. It is well known that the electronic transport properties of a molecule are governed by the energy difference between HOMO-LUMO, often referred to as band gap energy (ΔE). The red colour represents the positive phase of the orbital (virtual orbital), while the green colour represents the negative phase of the orbital (occupied orbital). Figure 5.25 A-B shows the variation of the calculated ΔE values for EFV and EFV-TiO_2-NPs as 5.23 eV and 4.28 eV respectively. This demonstrates the interaction to strongly absorbed between EFV-TiO_2-NPs.

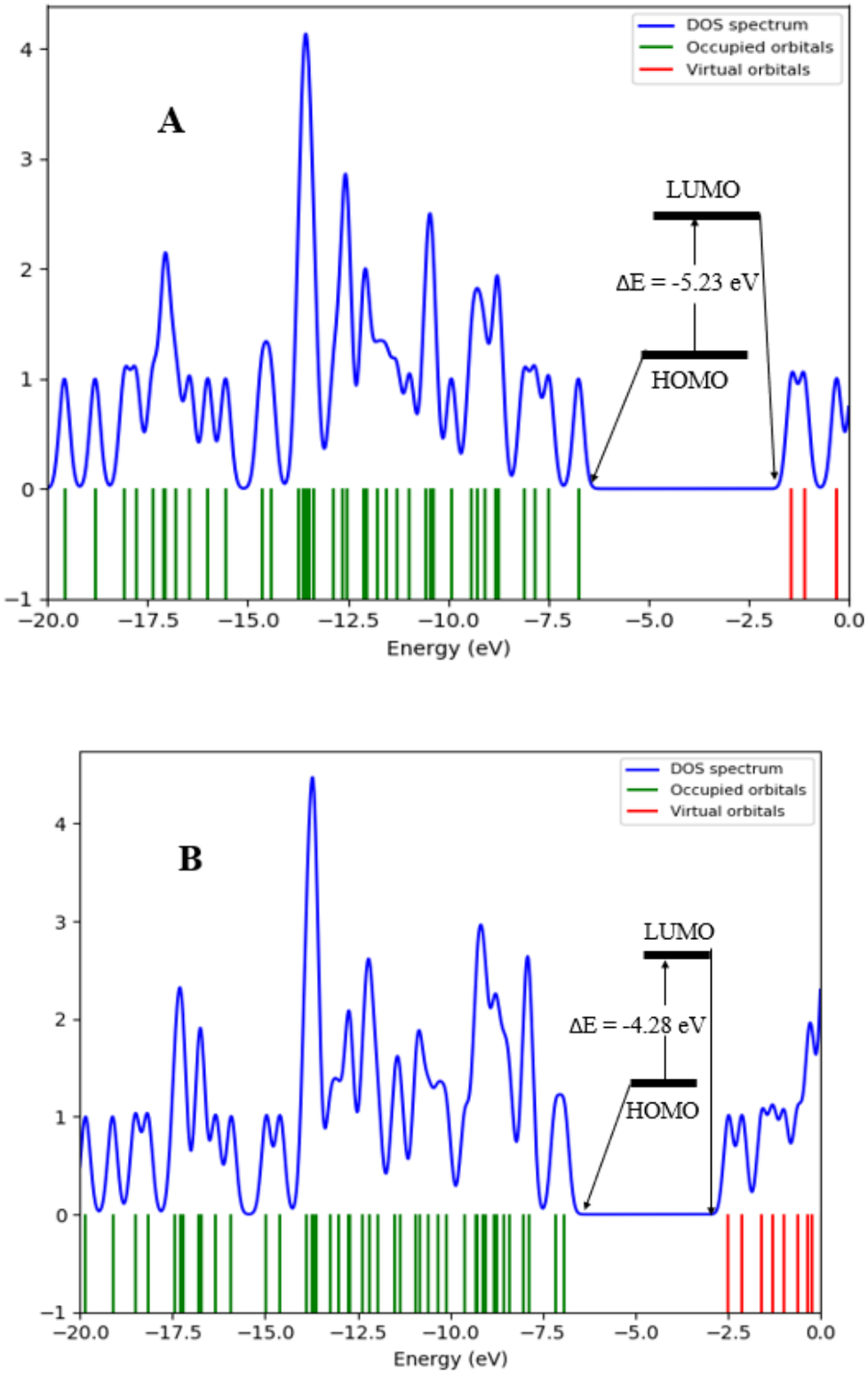

Figure 5.26: Calculated Density of States (DOS) for (A) EFV and (B) EFV-TiO_2-NPs in methanol using TD-DFT/B3LYP/6-31G* basis set.

Table 5.7: Calculated adsorption wavelengths for (a) EFV gas; (c) EFV methanol using TD-DFT/B3LYP/6-31G* basis set

Wavelength	**270.613/268.45 nm**		**240.59/242.79 nm**	
	Major contributions	Minor contributions	Major contributions	Minor contributions
EFV gas	HOMO->LUMO (88%)	H-3->L+1 (5%)	HOMO->L+1 (73%)	HOMO->LUMO (3%)
EFV methanol	HOMO->LUMO (86%)	H-3->L+1 (3%)	HOMO->L+1 (76%)	HOMO->LUMO (7%)

Table 5.8: Calculated adsorption wavelengths for (a) EFV-TiO_2-NPs gas; (c) EFV-TiO_2-NPs methanol using TD-DFT/B3LYP/6-31G* basis set

Wavelength	**312.78/369.73 nm**		**312.78/312.89 nm**	
	Major contributions	Minor contributions	Major contributions	Minor contributions
EFV-TiO_2-NPs gas	HOMO->LUMO (69%)	HOMO->L+1 (7%)		HOMO->L+1 (7%)
EFV-TiO_2-NPs methanol	HOMO->LUMO (71%)	HOMO->L+1 (7%)	H-1->LUMO (83%)	HOMO->L+1 (5%)

5.2.3 CONCLUSION

This study demonstrates that green synthesized TiO_2-NPs can be an effective photocatalyst for the degradation of EFV in aqueous solution under UV-light. The results obtained shows that the complete degradation efficiency of EFV can be attained at 91.77% over the period of 5 h. As predicted by the band gap differences between EFV, TiO_2-NPs and EFV-TiO_2-NPs a slight shift has been observed for the interaction of EFV-TiO_2-NPs predominantly suggesting the photodegradation of EFV. Supporting the experimental results, the UV-vis spectra was studied at TD-DFT level to explore the interaction between EFV and TiO_2-NPs. Based on the results, the charge transfer from EFV to the CB of the semiconductor TiO_2-NPs resulted from the UV towards the visible range, while the calculated ΔE values for EFV and EFV-TiO_2-NPs was 5.23 eV and 4.28 eV demonstrating that there was a interaction between EFV-TiO_2-NPs.

CHAPTER SIX: CONCLUDING REMARKS AND RECOMMENDATIONS

6.1 CONCLUDING REMARKS

The green synthesized TiO_2-NPs was successfully used as applications in sensing and preliminary studies on the photodegradation of EFV.

The first case study was based on the synthesis of TiO_2-NPs using *Eucalyptus globulus* leaf extract and its implementation as an electrochemical sensor. A successful synthesis was confirmed by characterization using ultraviolet–visible spectroscopy (UV–vis), scanning electron microscopy (SEM), X-ray diffraction (XRD), and energy-dispersive spectroscopy (EDS). An electrochemical sensor for EFV was designed by doping the green synthesized TiO_2-NPs onto a glassy carbon electrode (GCE) with nafion as an anchor agent (GCE/TiO_2-NPs-nafion). A low detection limit (LOD) of 0.01 µM with a linear dynamic concentration range from 4.5 to 18.7 µM was recorded on the electrode using DPV. The electrochemical sensor demonstrated good positive selectivity with excellent recoveries ranging from 92.0–103.9%. MC simulations revealed a strong electrostatic interaction on the GCE/TiO_2-NPs-nafion-EFV (substrate-adsorbate) system. While the DFT based calculations represented the chemical reactivity for EFV, suggesting the benzoxazine ring as the active site. In summary, the results obtained for this case study showed good agreement between the MC computed adsorption energies and the experimental CV results for EFV. The presence of nafion contributed to the signal amplification sensing of EFV.

The second case study involved spectroscopic and computational approaches in investigating the photodegradation of EFV as a preliminary study for future work. The experimental results revealed that there are two main transitions of EFV in a methanol, which correlates with the TD-DFT calculated UV spectrum. Further, the UV spectrum recorded for TiO_2-NPs and its band gap energy confirmed it as a semiconductor, which played a role in the photodegradation study. The noticeable shift in absorbance peaks for EFV, TiO_2-NPs, EFV-TiO_2-NPs and the differences in their band gap energies demonstrates the interaction between EFV and TiO_2-NPs. Additionally, the degradation efficiency of 91.77 % over 5 h was recorded with decreasing absorbance, suggesting the capability of TiO_2-NPs as potential photocatalyst. This was supported by the computational results, which demonstrated that EFV seems to be strongly

adsorbed on TiO_2-NPs, which leads to charge transfer from EFV to the CB of the semiconductor. Furthermore, the results from the DOS spectrum provides a visual understanding of the HOMO – LUMO plots for EFV and EFV-TiO_2-NPs in the presence of methanol.

In summary, this work demonstrated the use of biosynthesized TiO_2-NPs for the development of sensor for the detection of EFV and its photocatalytic properties. The experimental results were supported by computational studies involving the calculation of the HOMO-LUMO band gap energies using DFT and TD-DFT for the UV-visible spectra, while the adsorption energies were calculated by MC simulations.

6.2 RECOMMENDATIONS FOR FUTURE WORK

Based on the findings of the work, we recommend the following to be implemented as future work

- The electrochemical kinetics of EFV involving the prediction of number of electrons, charge transfer and diffusion coefficient and electron rate constant could be evaluated using alternate metal oxide nanoparticles to overcome the challenges in the present study.
- Photocatalysis of EFV using other metal oxide nanoparticles
- Investigate the performance of anatase, brookite and rutile instead of a single molecular form of TiO_2-NPs in the computational study.
- Molecular dynamics simulations with extended times to monitor the conformational profile of the complexes, and to compute the binding energies.

REFERENCES

Abou-Zied, O. K. and Al-Shihi, O. I. 2008. Characterization of subdomain IIA binding site of human serum albumin in its native, unfolded, and refolded states using small molecular probes. *Journal of the American Chemical Society*, 130 (32): 10793-10801.

Adebayo, E. A., Azeez, M. A., Alao, M. B., Oke, A. M. and Aina, D. A. 2021. Fungi as veritable tool in current advances in nanobiotechnology. *Heliyon*, 7 (11): e08480.

Adelere, I. A. and Lateef, A. 2016. A novel approach to the green synthesis of metallic nanoparticles: the use of agro-wastes, enzymes, and pigments. *Nanotechnology Reviews*, 5 (6): 567-587.

Agarwal, N. and Brem, A. 2017. Frugal innovation-past, present, and future. *IEEE Engineering Management Review*, 45 (3): 37-41.

Aguiar Castro, A., Queiroz Aucelio, R., Adrian Rey, N., Monsores Miguel, E. and Augusto Mardini Farias, P. 2011. Determination of the antiretroviral drug nevirapine in diluted alkaline electrolyte by adsorptive stripping voltammetry at the mercury film electrode. *Combinatorial Chemistry & High Throughput Screening*, 14 (1): 22-27.

Ahmad, W., Jaiswal, K. K. and Soni, S. 2020. Green synthesis of titanium dioxide (TiO2) nanoparticles by using Mentha arvensis leaves extract and its antimicrobial properties. *Inorganic and Nano-Metal Chemistry*, 50 (10): 1032-1038.

Ahmed, H. M., Roy, A., Wahab, M., Ahmed, M., Othman-Qadir, G., Elesawy, B. H., Khandaker, M. U., Islam, M. N. and Emran, T. B. 2021. Applications of nanomaterials in agrifood and pharmaceutical industry. *Journal of Nanomaterials*, 2021

Akbari Shorgoli, A. and Shokri, M. 2017. Photocatalytic degradation of imidacloprid pesticide in aqueous solution by TiO2 nanoparticles immobilized on the glass plate. *Chemical Engineering Communications*, 204 (9): 1061-1069.

Ali, A. S. 2020. Application of nanomaterials in environmental improvement. In: *Nanotechnology and the Environment*. IntechOpen.

Allam, N. G., Ismail, G. A., El-Gemizy, W. M. and Salem, M. A. 2019. Biosynthesis of silver nanoparticles by cell-free extracts from some bacteria species for dye removal from wastewater. *Biotechnology letters*, 41 (3): 379-389.

Amanulla, A. M. and Sundaram, R. 2019. Green synthesis of TiO2 nanoparticles using orange peel extract for antibacterial, cytotoxicity and humidity sensor applications. *Materials Today: Proceedings*, 8: 323-331.

Aminuzzaman, M., Ying, L. P., Goh, W.-S. and Watanabe, A. 2018. Green synthesis of zinc oxide nanoparticles using aqueous extract of Garcinia mangostana fruit pericarp and their photocatalytic activity. *Bulletin of Materials Science*, 41 (2): 1-10.

Applerot, G., Lellouche, J., Perkas, N., Nitzan, Y., Gedanken, A. and Banin, E. 2012. ZnO nanoparticle-coated surfaces inhibit bacterial biofilm formation and increase antibiotic susceptibility. *Rsc Advances*, 2 (6): 2314-2321.

Aravind, M., Amalanathan, M. and Mary, M. 2021. Synthesis of TiO2 nanoparticles by chemical and green synthesis methods and their multifaceted properties. *SN Applied Sciences*, 3 (4): 1-10.

Arnaldo Aguiar, C., Ricardo Queiroz, A., Nicolas Adrian, R., Eliane Monsores, M. and Percio Augusto Mardini, F. 2011. Determination of the Antiretroviral Drug Nevirapine in Diluted Alkaline Electrolyte by Adsorptive Stripping Voltammetry at the Mercury Film Electrode. *Combinatorial Chemistry & High Throughput Screening*, 14 (1): 22-27.

Aslam, M., Abdullah, A. Z. and Rafatullah, M. 2021. Recent development in the green synthesis of titanium dioxide nanoparticles using plant-based biomolecules for environmental and antimicrobial applications. *Journal of Industrial and Engineering Chemistry*, 98: 1-16.

Aslıhan Avan, A., Aydar, S. and Filik, H. 2015. Voltammetric sensing of bilirubin based on nafion/electrochemically reduced graphene oxide composite modified glassy carbon electrode. *Current Analytical Chemistry*, 11 (2): 96-103.

Aslışen, B. and Koçak, S. 2022. Preparation of mixed-valent manganese-vanadium oxide and Au nanoparticle modified graphene oxide nanosheets electrodes for the simultaneous determination of hydrazine and nitrite. *Journal of Electroanalytical Chemistry*, 904: 115875.

Asrami, P. N., Mozaffari, S. A., Tehrani, M. S. and Azar, P. A. 2018. A novel impedimetric glucose biosensor based on immobilized glucose oxidase on a CuO-Chitosan nanobiocomposite modified FTO electrode. *International journal of biological macromolecules*, 118: 649-660.

Barua, A. and Paul, A. 2020. Unravelling the role of temperature in a redox supercapacitor composed of multifarious nanoporous carbon@ hydroquinone. *RSC Advances*, 10 (3): 1799-1810.

Batchelor-McAuley, C., Wildgoose, G. G., Compton, R. G., Shao, L. and Green, M. L. 2008. Copper oxide nanoparticle impurities are responsible for the electroanalytical detection of glucose seen using multiwalled carbon nanotubes. *Sensors and Actuators B: Chemical*, 132 (1): 356-360.

Becke, A. D. 1993. A new mixing of Hartree–Fock and local density-functional theories. *The Journal of chemical physics*, 98 (2): 1372-1377.

Bekele, E. T., Gonfa, B. A., Zelekew, O. A., Belay, H. H. and Sabir, F. K. 2020. Synthesis of titanium oxide nanoparticles using root extract of Kniphofia foliosa as a template, characterization, and its application on drug resistance bacteria. *Journal of Nanomaterials*, 2020

Betancourt-Galindo, R., Reyes-Rodriguez, P., Puente-Urbina, B., Avila-Orta, C., Rodríguez-Fernández, O., Cadenas-Pliego, G., Lira-Saldivar, R. and García-Cerda, L. 2014. Synthesis of copper nanoparticles by thermal decomposition and their antimicrobial properties. *Journal of Nanomaterials*, 2014

Bhavani, A. G. and Wani, T. A. 2021. Synthesis of single phase LaMn1− XNiXO3 perovskite material. *Materials Letters: X*, 12: 100107.

Bhullar, S., Goyal, N. and Gupta, S. 2021. Rapid green-synthesis of TiO 2 nanoparticles for therapeutic applications. *RSC Advances*, 11 (48): 30343-30352.

Biovia, D. 2016. Material Studio modelling. v. 16.1. 0. *San Diego: Dassault Systemes*,

Brooms, T. J., Otieno, B., Onyango, M. S. and Ochieng, A. 2018. Photocatalytic degradation of P-Cresol using TiO2/ZnO hybrid surface capped with polyaniline. *Journal of Environmental Science and Health, Part*

Buzid, A., McGlacken, G. P., Glennon, J. D. and Luong, J. H. 2018. Electrochemical sensing of biotin using Nafion-modified boron-doped diamond electrode. *ACS omega*, 3 (7): 7776-7782.

Calzolai, L., Gilliland, D. and Rossi, F. 2012. Measuring nanoparticles size distribution in food and consumer products: a review. *Food Additives & Contaminants: Part A*, 29 (8): 1183-1193.

Cano-Casanova, L., Amorós-Pérez, A., Ouzzine, M., Lillo-Rodenas, M. A. and Román-Martínez, M. C. 2018. One step hydrothermal synthesis of TiO2 with variable HCl concentration: Detailed characterization and photocatalytic activity in propene oxidation. *Applied Catalysis B: Environmental*, 220: 645-653.

Castro, A. A., de Souza, M. V., Rey, N. A. and Farias, P. A. 2011. Determination of efavirenz in diluted alkaline electrolyte by cathodic adsorptive stripping voltammetry at the mercury film electrode. *Journal of the Brazilian Chemical Society*, 22 (9): 1662-1668.

Chaba, J. M. 2018. *Synthesis of Metal Oxides Coated Carbon Nanofibers and Their Application for Removal of Selected Antibiotics in Environmental Matrices*. University of Johannesburg (South Africa).

Cheeseman, S., Shaw, Z., Vongsvivut, J., Crawford, R. J., Dupont, M. F., Boyce, K. J., Gangadoo, S., Bryant, S. J., Bryant, G. and Cozzolino, D. 2021. Analysis of Pathogenic Bacterial and Yeast Biofilms Using the Combination of Synchrotron ATR-FTIR Microspectroscopy and Chemometric Approaches. *Molecules*, 26 (13): 3890.

Chen, D., Cheng, Y., Zhou, N., Chen, P., Wang, Y., Li, K., Huo, S., Cheng, P., Peng, P. and Zhang, R. 2020. Photocatalytic degradation of organic pollutants using TiO2-based photocatalysts: A review. *Journal of Cleaner Production*, 268: 121725.

Chen, G., Sun, H. and Hou, S. 2016. Electrochemistry and electrocatalysis of myoglobin immobilized in sulfonated graphene oxide and Nafion films. *Analytical Biochemistry*, 502: 43-49.

Chen, J., Zhang, Z., Zhu, W., Zhang, L., Zhao, B., Ji, Y., Li, G. and An, T. 2021. Superoxide radical enhanced photocatalytic performance of styrene alters its degradation mechanism and intermediate health risk on TiO2/graphene surface. *Environmental Research*, 195: 110747.

Chen, Q., Yao, Y., Li, X., Lu, J., Zhou, J. and Huang, Z. 2018. Comparison of heavy metal removals from aqueous solutions by chemical precipitation and characteristics of precipitates. *Journal of water process engineering*, 26: 289-300.

Chen, S., Zhang, Q., Hou, Y., Zhang, J. and Liang, X.-J. 2013. Nanomaterials in medicine and pharmaceuticals: nanoscale materials developed with less toxicity and more efficacy. *European Journal of Nanomedicine*, 5 (2): 61-79.

Cheng, D.-B., Qiao, Z.-Y., Xuan, L. and Wang, H. 2020. Recent advances of morphology adaptive nanomaterials for anti-cancer drug delivery. *Progress in Natural Science: Materials International*, 30 (5): 555-566.

Choi, B. G., Im, J., Kim, H. S. and Park, H. 2011. Flow-injection amperometric glucose biosensors based on graphene/Nafion hybrid electrodes. *Electrochimica Acta*, 56 (27): 9721-9726.

Cicchi, S., Cordero, F. M. and Giomi, D. 2011. Five-Membered Ring Systems with O & N Atoms. In: *Progress in Heterocyclic Chemistry*. Elsevier, 321-347.

Dastjerdi, R. and Montazer, M. 2010. A review on the application of inorganic nano-structured materials in the modification of textiles: focus on anti-microbial properties. *Colloids and surfaces B: Biointerfaces*, 79 (1): 5-18.

de Kruijff, G. H., Goschler, T., Beiser, N., Stenglein, A., Türk, O. M. and Waldvogel, S. R. 2019. Sustainable access to biobased biphenol epoxy resins by electrochemical dehydrogenative dimerization of eugenol. *Green Chemistry*, 21 (17): 4815-4823.

Del Ángel-Gómez, E. J., Gallardo-Rivas, N. V., Paramo-García, U., Díaz-Zavala, N. P., Banda-Cruz, E. E., Martínez-Orozco, R. D. and García-Alamilla, R. 2022. Ionic liquids as demulsifies for crude oil. Synthesis, characterization, and evaluation. *Petroleum Science and Technology*: 1-16.

Devi, H. S., Boda, M. A., Shah, M. A., Parveen, S. and Wani, A. H. 2019. Green synthesis of iron oxide nanoparticles using Platanus orientalis leaf extract for antifungal activity. *Green Processing and Synthesis*, 8 (1): 38-45.

Dhinakaran, V., Vigneswari, K., Lavanya, M. and Shree, M. V. 2020. Point-of-care applications with graphene in human life. In: *Comprehensive Analytical Chemistry*. Elsevier, 235-262.

Dhungana, R. K., Kc, S., Basnet, P. and Giri, R. 2018. Transition Metal-Catalyzed Dicarbofunctionalization of Unactivated Olefins. *The Chemical Record*, 18 (9): 1314-1340.

Długosz, O., Matysik, J., Matyjasik, W. and Banach, M. 2021. Catalytic and antimicrobial properties of α-amylase immobilised on the surface of metal oxide nanoparticles. *Journal of Cluster Science*, 32 (6): 1609-1622.

Dogan-Topal, B., Ozkan, S. and Uslu, B. 2007. Simultaneous determination of abacavir, efavirenz and valganciclovir in human serum samples by isocratic HPLC-DAD detection. *Chromatographia*, 66 (1): 25-30.

Dogan-Topal, B., Uslu, B. and Ozkan, S. A. 2009. Voltammetric studies on the HIV-1 inhibitory drug Efavirenz: The interaction between dsDNA and drug using electrochemical DNA biosensor and adsorptive stripping voltammetric determination on disposable pencil graphite electrode. *Biosensors and Bioelectronics*, 24 (8): 2358-2364.

dos Santos Martins, E., Oliveira, J. A., Franchin, T. B., Silva, B. C. U., Cândido, C. D. and Peccinini, R. G. 2019. Simple and rapid method by ultra high-performance liquid chromatography (UHPLC) with ultraviolet detection for determination of efavirenz in plasma: application in a preclinical pharmacokinetic study. *Journal of Chromatographic Science*, 57 (10): 874-880.

Dreizler, R. M. and da Providência, J. 2013. *Density functional methods in physics*. Springer Science & Business Media.

Dunlap, R. A. 2018. X-ray diffraction techniques. *Novel Microstructures for Solids; Morgan & Claypool Publishers: Halifax, NS, Canada*,

Eggeman, A. S. 2019. Scanning transmission electron diffraction methods. *Acta Crystallographica Section B: Structural Science, Crystal Engineering and Materials*, 75 (4): 475-484.

Eggleton, J. S. and Nagalli, S. 2020. Highly active antiretroviral therapy (HAART).

Elhag, S. 2017. *Chemically Modified Metal Oxide Nanostructures Electrodes for Sensing and Energy Conversion*. Linköping University Electronic Press.

Falzon, D., Jaramillo, E., Schünemann, H., Arentz, M., Bauer, M., Bayona, J., Blanc, L., Caminero, J., Daley, C. and Duncombe, C. 2011. *WHO guidelines for the programmatic management of drug-resistant tuberculosis: 2011 update*: Eur Respiratory Soc.

Fan, Y., Lu, H.-T., Liu, J.-H., Yang, C.-P., Jing, Q.-S., Zhang, Y.-X., Yang, X.-K. and Huang, K.-J. 2011. Hydrothermal preparation and electrochemical sensing properties of TiO2–graphene nanocomposite. *Colloids and Surfaces B: Biointerfaces*, 83 (1): 78-82.

Fon Sing, S., Isdepsky, A., Borowitzka, M. A. and Moheimani, N. R. 2013. Production of biofuels from microalgae. *Mitigation and adaptation strategies for global change*, 18 (1): 47-72.

Friston, K. J., Harrison, L. and Penny, W. 2003. Dynamic causal modelling. *Neuroimage*, 19 (4): 1273-1302.

G.W.T. M. J. Frisch, H. B. S., G. E. Scuseria, M. A. Robb, J. R. Cheeseman, G. Scalmani, V. Barone, G. A. Petersson, H. Nakatsuji, X. Li, M. Caricato, A. V. Marenich, J. Bloino, B. G. Janesko, R. Gomperts, B. Mennucci, H. P. Hratchian, J. V. Ortiz, A. F. Izmaylov, J. L. Sonnenberg, D. Y. Williams, F. Ding, F. Lipparini, F. Egidi, J. Goings, B. Peng, A. Petrone, T. Henderson, D. Ranasinghe, V. G. Zakrzewski, J. Gao, N. Rega, G. Zheng, W. Liang, M. Hada, M. Ehara, K. Toyota, R. Fukuda, J. Hasegawa, M. Ishida, T. Nakajima, Y. Honda, O. Kitao, H. Nakai, T. Vreven, K. Throssell, J. A. Montgomery Jr., J. E. Peralta, F. Ogliaro, M. J. Bearpark, J. J. Heyd, E. N. Brothers, K. N. Kudin, V. N. Staroverov, T. A. Keith, R. Kobayashi, J. Normand, K. Raghavachari, A. P. Rendell, J. C. Burant, S. S. Iyengar, J. Tomasi, M. Cossi, J. M. Millam, M. Klene, C. Adamo, R. Cammi, J. W. Ochterski, R. L. Martin, K. Morokuma, O. Farkas, J. B. Foresman, D. J. Fox, , . 2016.

Gadkari, T., Chandrachood, P., Ruikar, A., Tele, S., Deshpande, N., Salvekar, J. and Sonawane, S. 2010. Validated stability indicating LC-PDA-MS method to investigate pH rate profile and degradation kinetics of efavirenz and identification of hydrolysis product by LCMS. *International journal of pharmacy and pharmaceutical sciences*, 2 (1): 169-176.

Gentile, L., Mateos, H., Mallardi, A., Dell'Aglio, M., De Giacomo, A., Cioffi, N. and Palazzo, G. 2021. Gold nanoparticles obtained by ns-pulsed laser ablation in liquids (ns-PLAL) are arranged in the form of fractal clusters. *Journal of Nanoparticle Research*, 23 (2): 1-12.

Gilbert, A. 2017. Vibrational, Rotational and Raman Spectroscopy, Historical Perspective.

Gillet, M., Lemire, C., Gillet, E. and Aguir, K. 2003. The role of surface oxygen vacancies upon WO3 conductivity. *Surface Science*, 532: 519-525.

Gong, Q., Wang, Y. and Yang, H. 2017. A sensitive impedimetric DNA biosensor for the determination of the HIV gene based on graphene-Nafion composite film. *Biosensors and Bioelectronics*, 89: 565-569.

Gribat, L. C., Babauta, J. T., Beyenal, H. and Wall, N. A. 2017. New rotating disk hematite film electrode for riboflavin detection. *Journal of Electroanalytical Chemistry*, 798: 42-50.

Griffiths, P. R. and James, A. 2007. *De Haseth. Fourier transform infrared spectrometry. Vol. 171*: John Wiley & Sons.

Gu, S., Wang, H., Wu, C., Bai, Y., Li, H. and Wu, F. 2017. Confirming reversible Al3+ storage mechanism through intercalation of Al3+ into V2O5 nanowires in a rechargeable aluminum battery. *Energy Storage Materials*, 6: 9-17.

Guan, Z., Ying, S., Ofoegbu, P. C., Clubb, P., Rico, C., He, F. and Hong, J. 2022. Green synthesis of nanoparticles: Current developments and limitations. *Environmental Technology & Innovation*: 102336.

Guichard, N., Tobolkina, E., El Morabit, L., Bonnabry, P., Vernaz, N. and Rudaz, S. 2021. Determination of antiretroviral drugs for buyers' club in Switzerland using capillary electrophoresis methods. *Electrophoresis*, 42 (6): 708-718.

Guy, O. J. and Walker, K.-A. D. 2016. Graphene functionalization for biosensor applications. *Silicon Carbide Biotechnology*: 85-141.

Hamrapurkar, P. D., Patil, P. S., Phale, M. D., Shah, N. and Pawar, S. B. 2010. Optimization and validation of RP-HPLC stability-indicating method for determination of efavirenz and its degradation products. *International Journal of Applied Science and Engineering*, 8 (2): 155-165.

Hany, R. A. 2022. Tools used for dental materials characterization. *Biomaterials Journal*, 1 (3): 9-16.

Hareesha, N. and Manjunatha, J. 2021. Electro-oxidation of formoterol fumarate on the surface of novel poly (thiazole yellow-G) layered multi-walled carbon nanotube paste electrode. *Scientific Reports*, 11 (1): 1-14.

Hareesha, N., Manjunatha, J., Amrutha, B., Sreeharsha, N., Asdaq, S. B. and Anwer, M. K. 2021. A fast and selective electrochemical detection of vanillin in food samples on the surface of poly (glutamic acid) functionalized multiwalled carbon nanotubes and graphite composite paste sensor. *Colloids and Surfaces A: Physicochemical and Engineering Aspects*, 626: 127042.

He, T., Ma, Y., Cao, Y., Hu, X., Liu, H., Zhang, G., Yang, W. and Yao, J. 2002. Photochromism of WO3 colloids combined with TiO2 nanoparticles. *The Journal of Physical Chemistry B*, 106 (49): 12670-12676.

Hecht, M., Harrer, T., Büttner, M., Schwegler, M., Erber, S., Fietkau, R. and Distel, L. V. 2013. Cytotoxic effect of efavirenz is selective against cancer cells and associated with the cannabinoid system. *AIDS*, 27 (13): 2031-2040.

Hepel, M. and Luo, J. 2001. Photoelectrochemical mineralization of textile diazo dye pollutants using nanocrystalline WO3 electrodes. *Electrochimica Acta*, 47 (5): 729-740.

Hohenberg, P. and Kohn, W. 1964. Inhomogeneous electron gas. *Physical review*, 136 (3B): B864.

Honarmand, M. M., Mehr, M. E., Yarahmadi, M. and Siadati, M. H. 2019. Effects of different surfactants on morphology of TiO2 and Zr-doped TiO2 nanoparticles and their applications in MB dye photocatalytic degradation. *SN Applied Sciences*, 1 (5): 1-12.

Honerkamp, J. and Weese, J. 1990. Tikhonovs regularization method for ill-posed problems. *Continuum Mechanics and Thermodynamics*, 2 (1): 17-30.

Hu, X.-L., Shang, Y., Yan, K.-C., Sedgwick, A. C., Gan, H.-Q., Chen, G.-R., He, X.-P., James, T. D. and Chen, D. 2021. Low-dimensional nanomaterials for antibacterial applications. *Journal of Materials Chemistry B*, 9 (17): 3640-3661.

Hugen, P. W., Burger, D. M., Aarnoutse, R. E., Baede, P. A., Nieuwkerk, P. T., Koopmans, P. P. and Hekster, Y. A. 2002. Therapeutic drug monitoring of HIV-protease inhibitors to assess noncompliance. *Therapeutic drug monitoring*, 24 (5): 579-587.

Hussain, C. M. and Keçili, R. 2019. *Modern environmental analysis techniques for pollutants*. Elsevier.

Hussein, M., Adesina, A. Y., Kumar, A. M., Sorour, A., Ankah, N. and Al-Aqeeli, N. 2020. Mechanical, in-vitro corrosion, and tribological characteristics of TiN coating produced by cathodic arc physical vapor deposition on Ti20Nb13Zr alloy for biomedical applications. *Thin Solid Films*, 709: 138183.

Im, J. S., Kim, M. I. and Lee, Y.-S. 2008. Preparation of PAN-based electrospun nanofiber webs containing TiO2 for photocatalytic degradation. *Materials Letters*, 62 (21-22): 3652-3655.

Ishimoto, T., Miyake, K., Nandi, T., Yashiro, M., Onishi, N., Huang, K. K., Lin, S. J., Kalpana, R., Tay, S. T. and Suzuki, Y. 2017. Activation of transforming growth factor beta 1 signaling in gastric cancer-associated fibroblasts increases their motility, via expression of rhomboid 5 homolog 2, and ability to induce invasiveness of gastric cancer cells. *Gastroenterology*, 153 (1): 191-204. e116.

Izaki, M., Shinagawa, T., Mizuno, K.-T., Ida, Y., Inaba, M. and Tasaka, A. 2007. Electrochemically constructed p-Cu2O/n-ZnO heterojunction diode for photovoltaic device. *Journal of Physics D: Applied Physics*, 40 (11): 3326.

Jacob, A., Ashok, B., Alagumalai, A., Chyuan, O. H. and Le, P. T. K. 2021. Critical review on third generation micro algae biodiesel production and its feasibility as future bioenergy for IC engine applications. *Energy Conversion and Management*, 228: 113655.

Jain, A., Shin, Y. and Persson, K. A. 2016. Computational predictions of energy materials using density functional theory. *Nature Reviews Materials*, 1 (1): 1-13.

Jeevanandam, J., Barhoum, A., Chan, Y. S., Dufresne, A. and Danquah, M. K. 2018. Review on nanoparticles and nanostructured materials: history, sources, toxicity and regulations. *Beilstein journal of nanotechnology*, 9 (1): 1050-1074.

Jeevanandam, J., Chan, Y. S. and Danquah, M. K. 2016. Biosynthesis of metal and metal oxide nanoparticles. *ChemBioEng Reviews*, 3 (2): 55-67.

Jeevanandam, J., Krishnan, S., Hii, Y. S., Pan, S., Chan, Y. S., Acquah, C., Danquah, M. K. and Rodrigues, J. 2022. Synthesis approach-dependent antiviral properties of silver nanoparticles and nanocomposites. *Journal of Nanostructure in Chemistry*: 1-23.

Jeong, H., Yoo, J., Park, S., Lu, J., Park, S. and Lee, J. 2021. Non-Enzymatic Glucose Biosensor Based on Highly Pure TiO2 Nanoparticles. *Biosensors*, 11 (5): 149.

Ji, Y., Zhou, Y., Ma, C., Feng, Y., Hao, Y., Rui, Y., Wu, W., Gui, X., Han, Y. and Wang, Y. 2017. Jointed toxicity of TiO2 NPs and Cd to rice seedlings: NPs alleviated Cd toxicity and Cd promoted NPs uptake. *Plant Physiology and Biochemistry*, 110: 82-93.

Jordaan, M. A. and Shapi, M. 2017. Investigation of the solvent-dependent photolysis of a nonnucleoside reverse-transcriptase inhibitor, antiviral agent efavirenz. *Antiviral Chemistry and Chemotherapy*, 25 (3): 94-104.

Joshi, D. R. and Adhikari, N. 2019. An overview on common organic solvents and their toxicity. *J. Pharm. Res. Int*, 28 (3): 1-18.

Justh, N., Bakos, L. P., Hernádi, K., Kiss, G., Réti, B., Erdélyi, Z., Parditka, B. and Szilágyi, I. M. 2017. Photocatalytic hollow TiO2 and ZnO nanospheres prepared by atomic layer deposition. *Scientific reports*, 7 (1): 1-9.

Kalanur, S. S., Seetharamappa, J. and Prashanth, S. 2010. Voltammetric sensor for buzepide methiodide determination based on TiO2 nanoparticle-modified carbon paste electrode. *Colloids and Surfaces B: Biointerfaces*, 78 (2): 217-221.

Kalinichev, A. and Kirkpatrick, R. 2007. Molecular dynamics simulation of cationic complexation with natural organic matter. *European Journal of Soil Science*, 58 (4): 909-917.

Kamaruzaman, N. H., Noor, N. N. M., Mohamed, R. M. S. R., Al-Gheethi, A., Ponnusamy, S. K., Sharma, A. and Vo, D.-V. N. 2022. Applicability of bio-synthesized nanoparticles in fungal secondary metabolites products and plant extracts for eliminating antibiotic-resistant bacteria risks in non-clinical environments. *Environmental Research*, 209: 112831.

Kanniyappan, S., SaravanaKumar, S. and Muthukumaran, T. 2017. Analyzing the Microstructural Properties of Nanomaterial in OPC by SEM, TEM, XRD and Corrosion Rate by TAFEL Techniques. *International Research Journal of Engineering and Technology*, 4: 1497-1503.

Karimi, F., Demir, E., Aydogdu, N., Shojaei, M., Taher, M. A., Asrami, P. N., Alizadeh, M., Ghasemi, Y. and Cheraghi, S. 2022. Advancement in electrochemical strategies for quantification of Brown HT and Carmoisine (Acid Red 14) Drom Azo Dyestuff class. *Food and Chemical Toxicology*: 113075.

Kaya, H. O., Cetin, A. E., Azimzadeh, M. and Topkaya, S. N. 2021. Pathogen detection with electrochemical biosensors: Advantages, challenges and future perspectives. *Journal of Electroanalytical Chemistry*, 882: 114989.

Keçili, R. and Denizli, A. 2021. Molecular Imprinting-Based Smart Nanosensors for Pharmaceutical Applications. In: *Molecular Imprinting for Nanosensors and Other Sensing Applications*. Elsevier, 19-43.

Keskin, A., Koprulu, T. K., Bursali, A., Ozsemir, A. C., Yavuz, K. E. and Tekin, S. 2014. First record of Ixodes arboricola (Ixodida: Ixodidae) from Turkey with presence of Candidatus Rickettsia vini (Rickettsiales: Rickettsiaceae). *Journal of medical entomology*, 51 (4): 864-867.

Khan, I. U., Sajid, S., Javed, A., Sajid, S. and Shah, S. U. 2017. Comparative diagnosis of typhoid fever by polymerase chain reaction and widal test in Southern Districts (Bannu, Lakki Marwat and DI Khan) of Khyber Pakhtunkhwa, Pakistan. *Acta Sci. Malaysia*, 1 (2): 12-15.

Khare, P., Sonane, M., Pandey, R., Ali, S., Gupta, K. C. and Satish, A. 2011. Adverse effects of TiO2 and ZnO nanoparticles in soil nematode, Caenorhabditis elegans. *Journal of Biomedical Nanotechnology*, 7 (1): 116-117.

Kim, D., Lee, S. and Piao, Y. 2017. Electrochemical determination of dopamine and acetaminophen using activated graphene-Nafion modified glassy carbon electrode. *Journal of Electroanalytical Chemistry*, 794: 221-228.

Kim, K.-B., Kim, H., Jiang, F., Yeo, C.-W., Bae, S. K., Desta, Z., Shin, J.-G. and Liu, K.-H. 2011. Rapid and simultaneous determination of efavirenz, 8-hydroxyefavirenz, and 8, 14-dihydroxyefavirenz using LC–MS–MS in human plasma and application to pharmacokinetics in healthy volunteers. *Chromatographia*, 73 (3): 263-271.

Kim, M., Osone, S., Kim, T., Higashi, H. and Seto, T. 2017. Synthesis of nanoparticles by laser ablation: A review. *KONA Powder and Particle Journal*: 2017009.

Kim, T., Choi, W., Shin, H.-C., Choi, J.-Y., Kim, J. M., Park, M.-S. and Yoon, W.-S. 2020. Applications of voltammetry in lithium ion battery research. *Journal of Electrochemical Science and Technology*, 11 (1): 14-25.

Koch, C. C. and Whittenberger, J. 1996. Mechanical milling/alloying of intermetallics. *Intermetallics*, 4 (5): 339-355.

Kohn, W. and Sham, L. J. 1965. Self-consistent equations including exchange and correlation effects. *Physical review*, 140 (4A): A1133.

Korni, F. and Khalil, F. 2017. Effect of ginger and its nanoparticles on growth performance, cognition capability, immunity and prevention of motile Aeromonas septicaemia in Cyprinus carpio fingerlings. *Aquaculture Nutrition*, 23 (6): 1492-1499.

Kshetri, T., Tran, D. T., Nguyen, D. C., Kim, N. H., Lau, K.-t. and Lee, J. H. 2020. Ternary graphene-carbon nanofibers-carbon nanotubes structure for hybrid supercapacitor. *Chemical Engineering Journal*, 380: 122543.

Kumaravel, A. and Chandrasekaran, M. 2011. A biocompatible nano TiO2/nafion composite modified glassy carbon electrode for the detection of fenitrothion. *Journal of electroanalytical chemistry*, 650 (2): 163-170.

Kwiecińska, B., Pusz, S. and Valentine, B. J. 2019. Application of electron microscopy TEM and SEM for analysis of coals, organic-rich shales and carbonaceous matter. *International Journal of Coal Geology*, 211: 103203.

Laborda, F., Bolea, E. and Jimenez-Lamana, J. 2014. *Single particle inductively coupled plasma mass spectrometry: a powerful tool for nanoanalysis*: ACS Publications.

Lahiri, D., Nag, M., Sheikh, H. I., Sarkar, T., Edinur, H. A., Pati, S. and Ray, R. R. 2021. Microbiologically-synthesized nanoparticles and their role in silencing the biofilm signaling cascade. *Frontiers in microbiology*, 12: 180

Lakshmi Sailaja, A., Kishore Kumar, K., Ravi Kumar, D., Mohan Kumar, C., Yugandhar, N. and Srinubabu, G. 2007. Development and validation of a liquid chromatographic method for determination of efavirenz in human plasma. *Chromatographia*, 65 (5): 359-361.

Lalmalsawmi, J., Tiwari, D. and Kim, D. J. 2020. Role of nanocomposite materials in the development of electrochemical sensors for arsenic: past, present and future. *Journal of Electroanalytical Chemistry*, 877: 114630.

Landers, J., Gor, G. Y. and Neimark, A. V. 2013. Density functional theory methods for characterization of porous materials. *Colloids and Surfaces A: Physicochemical and Engineering Aspects*, 437: 3-32.

Lanzalaco, S. and Molina, B. G. 2020. Polymers and plastics modified electrodes for biosensors: a review. *Molecules*, 25 (10): 2446.

Laviron, E. 1979. General expression of the linear potential sweep voltammogram in the case of diffusionless electrochemical systems. *Journal of Electroanalytical Chemistry and Interfacial Electrochemistry*, 101 (1): 19-28.

Le, A., Pung, S., Chiam, S., Josoh, N. B. N., Koay, T., Lee, J. and Mustar, N. 2020. Photocatalytic performance of TiO2 particles in degradation of various organic dyes under visible and UV light irradiation. In: Proceedings of *AIP Conference Proceedings*. AIP Publishing LLC, 020017.

Leary, S. L., Underwood, W., Anthony, R., Cartner, S., Corey, D., Grandin, T., Greenacre, C., Gwaltney-Brant, S., McCrackin, M. and Meyer, R. 2013. AVMA guidelines for the euthanasia of animals: 2013 edition. In: Proceedings of. American Veterinary Medical Association Schaumburg, IL,

Lee, C., Yang, W. and Parr, R. G. 1988. Development of the Colle-Salvetti correlation-energy formula into afunctional of the electron density. *Physical review B*, 37 (2): 785.

Lee, J. 2014. Electrochemical sensing of oxygen gas in ionic liquids on screen printed electrodes. Curtin University.

Levy, M. 2010. On the simple constrained-search reformulation of the Hohenberg–Kohn theorem to include degeneracies and more (1964–1979). *International Journal of Quantum Chemistry*, 110 (15): 3140-3144.

LewisOscar, F., Vismaya, S., Arunkumar, M., Thajuddin, N., Dhanasekaran, D. and Nithya, C. 2016. Algal nanoparticles: synthesis and biotechnological potentials. *Algae-organisms for imminent biotechnology*, 7: 157-182.

Li, C., Jin, S., Guan, W., Tsang, C.-W., Chu, W.-K., Lau, W. K. and Liang, C. 2018. Chemical precipitation method for the synthesis of Nb2O5 modified bulk nickel catalysts with high specific surface area. *JoVE (Journal of Visualized Experiments)*, (132): e56987.

Li, C., Wang, D., Gu, J., Liu, Y. and Zhang, X. 2021. Promoting photoelectrochemical water oxidation on Ti-doped Fe2O3 nanowires photoanode by O2 plasma treatment. *Catalysts*, 11 (1): 82.

López-Acosta, N., Espinosa-Santiago, A., Pineda-Núñez, V., Ossa, A., Mendoza, M., Ovando-Shelley, E. and Botero, E. 2019. Performance of a test embankment on very soft clayey soil improved with drain-to-drain vacuum preloading technology. *Geotextiles and Geomembranes*, 47 (5): 618-631.

Lu, S.-y., Wu, D., Wang, Q.-l., Yan, J., Buekens, A. G. and Cen, K.-f. 2011. Photocatalytic decomposition on nano-TiO2: Destruction of chloroaromatic compounds. *Chemosphere*, 82 (9): 1215-1224.

Madhura, T. R., Devi, K. S. and Ramaraj, R. 2021. Introduction to electrochemical sensors for the detection of toxic chemicals. In: *Metal Oxides in Nanocomposite-Based Electrochemical Sensors for Toxic Chemicals*. Elsevier, 1-18.

Majidi, H. J., Mirzaee, A., Jafari, S. M., Amiri, M., Shahrousvand, M. and Babaei, A. 2020. Fabrication and characterization of graphene oxide-chitosan-zinc oxide ternary nano-hybrids for the corrosion inhibition of mild steel. *International journal of biological macromolecules*, 148: 1190-1200.

Mal, N., Mohapatra, R., Bagchi, T., Singh, S., Sharma, Y., Singh, M., Chavali, M. and Chandrasekhar, K. 2021. Green Nanotechnology: A Microalgal Approach to Remove Heavy Metals from Wastewater. In: *Phycology-Based Approaches for Wastewater Treatment and Resource Recovery*. CRC Press, 175-208.

Mandal, S., Jain, N., Pandey, M. K., Sreejakumari, S., Shukla, P., Chanda, A., Som, S., Das, S. and Singh, J. 2019. Ultra-bright emission from Sr doped TiO2 nanoparticles through r-GO conjugation. *Royal Society open science*, 6 (3): 190100.

Manivasagan, P., Nam, S. Y. and Oh, J. 2016. Marine microorganisms as potential biofactories for synthesis of metallic nanoparticles. *Critical reviews in microbiology*, 42 (6): 1007-1019.

Manns, B., Tonelli, M., Yilmaz, S., Lee, H., Laupland, K., Klarenbach, S., Radkevich, V. and Murphy, B. 2005. Establishment and maintenance of vascular access in incident hemodialysis patients: a prospective cost analysis. *Journal of the American Society of Nephrology*, 16 (1): 201-209.

Marques, M. A. and Gross, E. K. 2004. Time-dependent density functional theory. *Annu. Rev. Phys. Chem.*, 55: 427-455.

Martin, J., Deslandes, G., Dailly, E., Renaud, C., Reliquet, V., Raffi, F. and Jolliet, P. 2009. A liquid chromatography–tandem mass spectrometry assay for quantification of nevirapine, indinavir, atazanavir, amprenavir, saquinavir, ritonavir, lopinavir, efavirenz, tipranavir, darunavir and maraviroc in the plasma of patients infected with HIV. *Journal of Chromatography B*, 877 (27): 3072-3082.

Martins, R., Gaspar, D., Mendes, M. J., Pereira, L., Martins, J., Bahubalindruni, P., Barquinha, P. and Fortunato, E. 2018. Papertronics: Multigate paper transistor for multifunction applications. *Applied Materials Today*, 12: 402-414.

Marzbani, P., Afrouzi, Y. M. and Omidvar, A. 2015. The effect of nano-zinc oxide on particleboard decay resistance. *Maderas. Ciencia y tecnología*, 17 (1): 63-68.

Masenga, W., Paganotti, G. M., Seatla, K., Gaseitsiwe, S. and Sichilongo, K. 2021. A fast-screening dispersive liquid–liquid microextraction–gas chromatography–mass spectrometry method applied to the determination of efavirenz in human plasma samples. *Analytical and bioanalytical chemistry*, 413 (25): 6401-6412.

Maurer-Jones, M. A., Gunsolus, I. L., Murphy, C. J. and Haynes, C. L. 2013. Toxicity of engineered nanoparticles in the environment. *Analytical chemistry*, 85 (6): 3036-3049.

Medvids, A., Onufrijevs, P., Kaupužs, J., Eglitis, R., Padgurskas, J., Zunda, A., Mimura, H., Skadins, I. and Varnagiris, S. 2021. Anatase or rutile TiO2 nanolayer formation on Ti substrates by laser radiation: Mechanical, photocatalytic and antibacterial properties. *Optics & Laser Technology*, 138: 106898.

Milani, P. and Sowwan, M. 2020. *Cluster beam deposition of functional nanomaterials and devices*. Elsevier.

Moarrefzadeh, A. and Branch, M. 2012. Simulation and modeling of physical vapor deposition (PVD) process. *WSEAS transactions on applied and theoretical mechanics*, 7 (2): 106-111.

Mogomotsi, R. N., Akinola, S. S., Emeka, E. E. and Fayemi, O. E. 2020. Cyclic voltammetry, photocatalytic and antimicrobial comparative studies of fabrication Fe3O4 and Fe3O4/PAN nanofibers. *Materials Research Express*, 7 (5): 055001.

Mondal, K. and Sharma, A. 2016. Recent advances in the synthesis and application of photocatalytic metal–metal oxide core–shell nanoparticles for environmental remediation and their recycling process. *RSC advances*, 6 (87): 83589-83612.

More, S., Tandulwadkar, S., Nikam, A., Rathore, A., Sathiyanarayanan, L. and Mahadik, K. 2013. Separation and determination of lamivudine, tenofovir disoproxil fumarate and efavirenz in tablet dosage form by thin-layer chromatographic-densitometric method. *JPC-Journal of Planar Chromatography-Modern TLC*, 26 (1): 78-85.

Mukhopadhyay, S. C. and Nag, A. Screen printed electrode based sensor for biological and chemical species detection.

Mustafa, G., Khan, M. S., Asif, M. I., Ullah, A., Khan, I. and Ullah, I. 2021. Water pollutants and nanosensors. In: *Aquananotechnology*. Elsevier, 105-133.

Myrovali, E. 2020. Magnetic nanoparticle arrays: features, properties, applications. Αριστοτέλειο Πανεπιστήμιο Θεσσαλονίκης (ΑΠΘ). Σχολή Θετικών Επιστημών. Τμήμα ….

Nabi, G., Raza, W. and Tahir, M. 2020. Green synthesis of TiO2 nanoparticle using cinnamon powder extract and the study of optical properties. *Journal of Inorganic and Organometallic Polymers and Materials*, 30 (4): 1425-1429.

Nezamzadeh-Ejhieh, A. and Pouladsaz, P. 2014. Voltammetric determination of riboflavin based on electrocatalytic oxidation at zeolite-modified carbon paste electrodes. *Journal of Industrial and Engineering Chemistry*, 20 (4): 2146-2152.

Nigović, B., Marušić, M. and Jurić, S. 2011. A highly sensitive method for determination of β-blocker drugs using a Nafion-coated glassy carbon electrode. *Journal of electroanalytical chemistry*, 663 (2): 72-78.

Nnamchi, P. S. and Obayi, C. S. 2018. Electrochemical characterization of nanomaterials. In: *Characterization of Nanomaterials*. Elsevier, 103-127.

Northrop, P. W. and Cole, J. V. 2018. A Pulse Voltammetry Analysis Toolkit for Battery and Fuel Cell Material. *ECS Transactions*, 85 (5): 23.

Notari, S., Mancone, C., Alonzi, T., Tripodi, M., Narciso, P. and Ascenzi, P. 2008. Determination of abacavir, amprenavir, didanosine, efavirenz, nevirapine, and stavudine concentration in human plasma by MALDI-TOF/TOF. *Journal of Chromatography B*, 863 (2): 249-257.

Nwogu, J. N., Gandhi, M., Owen, A., Khoo, S. H., Taiwo, B., Olagunju, A., Berzins, B., Okochi, H., Tallerico, R. and Robertson, K. 2021. Associations between efavirenz concentrations, pharmacogenetics and neurocognitive performance in people living with HIV in Nigeria. *AIDS (London, England)*, 35 (12): 1919.

O'boyle, N. M., Tenderholt, A. L. and Langner, K. M. 2008. Cclib: a library for package-independent computational chemistry algorithms. *Journal of computational chemistry*, 29 (5): 839-845.

Ohta, R., Fukada, K., Tashiro, T., Dougakiuchi, M. and Kambara, M. 2018. Effect of PS-PVD production throughput on Si nanoparticles for negative electrode of lithium ion batteries. *Journal of Physics D: Applied Physics*, 51 (10): 105501.

Oliveira, T. M. and Morais, S. 2018. New generation of electrochemical sensors based on multi-walled carbon nanotubes. *Applied Sciences*, 8 (10): 1925.

Organization, W. H. 2019. *Policy brief: update of recommendations on first-and second-line antiretroviral regimens*. World Health Organization.

Padmanabhan, P. 2019. Lasers and its Application in Periodontology: A Review. *Indian Journal of Public Health Research & Development*, 10 (11)

Pamuk, D., Taşdemir, İ. H., Ece, A., Canel, E. and Kılıç, E. 2013. Redox pathways of aliskiren based on experimental and computational approach and its voltammetric determination. *Journal of the Brazilian Chemical Society*, 24 (8): 1276-1286.

Pang, P., Yan, F., Li, H., Li, H., Zhang, Y., Wang, H., Wu, Z. and Yang, W. 2016. Graphene quantum dots and Nafion composite as an ultrasensitive electrochemical sensor for the detection of dopamine. *Analytical Methods*, 8 (24): 4912-4918.

Pantidos, N. and Horsfall, L. E. 2014. Biological synthesis of metallic nanoparticles by bacteria, fungi and plants. *Journal of Nanomedicine & Nanotechnology*, 5 (5): 1.

Parashar, M., Shukla, V. K. and Singh, R. 2020. Metal oxides nanoparticles via sol–gel method: a review on synthesis, characterization and applications. *Journal of Materials Science: Materials in Electronics*, 31 (5): 3729-3749.

Pathakoti, K., Morrow, S., Han, C., Pelaez, M., He, X., Dionysiou, D. D. and Hwang, H.-M. 2013. Photoinactivation of Escherichia coli by sulfur-doped and nitrogen–fluorine-codoped TiO2 nanoparticles under solar simulated light and visible light irradiation. *Environmental science & technology*, 47 (17): 9988-9996.

Paul, D. and Sinha, S. N. 2014. Extracellular Synthesis of Silver Nanoparticles Using Pseudomonas aeruginosa KUPSB12 and Its Antibacterial Activity. *Jordan Journal of Biological Sciences*, 7 (4)

Paumo, H. K., Dalhatou, S., Katata-Seru, L. M., Kamdem, B. P., Tijani, J. O., Vishwanathan, V., Kane, A. and Bahadur, I. 2021. TiO2 assisted photocatalysts for degradation of emerging organic pollutants in water and wastewater. *Journal of Molecular Liquids*, 331: 115458.

Peng, H., Wang, J., Zhang, X., Ma, J., Shen, T., Li, S. and Dong, B. 2021. A review on synthesis, characterization and application of nanoencapsulated phase change materials for thermal energy storage systems. *Applied Thermal Engineering*, 185: 116326.

Pereira, E. A., Micke, G. A. and Tavares, M. F. 2005. Determination of antiretroviral agents in human serum by capillary electrophoresis. *Journal of Chromatography A*, 1091 (1-2): 169-176.

Pratiwi, R. A. and Nandiyanto, A. B. D. 2022. How to Read and Interpret UV-VIS Spectrophotometric Results in Determining the Structure of Chemical Compounds. *Indonesian Journal of Educational Research and Technology*, 2 (1): 1-20.

Putra, B. R., Aoki, K. J., Chen, J. and Marken, F. 2019. Cationic rectifier based on a graphene oxide-covered microhole: theory and experiment. *Langmuir*, 35 (6): 2055-2065.

Raccichini, R., Amores, M. and Hinds, G. 2019. Critical review of the use of reference electrodes in Li-ion batteries: a diagnostic perspective. *Batteries*, 5 (1): 12.

Raj, M., Gupta, P., Thapliyal, N. and Goyal, R. N. 2017. A Novel Hybrid Nano-composite Grafted Electrochemically Reduced Graphene Oxide Based Sensor for Sensitive Determination of Efavirenz. *Electroanalysis*, 29 (2): 456-465.

Rajeshkumar, S. and Bharath, L. 2017. Mechanism of plant-mediated synthesis of silver nanoparticles–a review on biomolecules involved, characterisation and antibacterial activity. *Chemico-biological interactions*, 273: 219-227.

Ramachandran, G., Kumar, A. H., Swaminathan, S., Venkatesan, P., Kumaraswami, V. and Greenblatt, D. J. 2006. Simple and rapid liquid chromatography method for determination of efavirenz in plasma. *Journal of chromatography B*, 835 (1-2): 131-135.

Ramachandran, K., Deepa, G. and Namboori, K. 2008. *Computational chemistry and molecular modeling: principles and applications*. Springer Science & Business Media.

Randviir, E. P. and Banks, C. E. 2013. Electrochemical impedance spectroscopy: an overview of bioanalytical applications. *Analytical methods*, 5 (5): 1098-1115.

Rane, A. V., Kanny, K., Abitha, V. and Thomas, S. 2018. Methods for synthesis of nanoparticles and fabrication of nanocomposites. In: *Synthesis of inorganic nanomaterials*. Elsevier, 121-139.

Raychaudhuri, S. 2008. Introduction to monte carlo simulation. In: Proceedings of *2008 Winter simulation conference*. IEEE, 91-100.

Rennhofer, H. and Zanghellini, B. 2021. Dispersion state and damage of carbon nanotubes and carbon nanofibers by ultrasonic dispersion: a review. *Nanomaterials*, 11 (6): 1469.

Reverberi, A., Vocciante, M., Lunghi, E., Pietrelli, L. and Fabiano, B. 2017. New trends in the synthesis of nanoparticles by green methods. *Chemical Engineering Transactions*, 61: 667-672.

Revin, S. B. and John, S. A. 2012. Simultaneous determination of vitamins B2, B9 and C using a heterocyclic conducting polymer modified electrode. *Electrochimica acta*, 75: 35-41.

Rifkin-Graboi, A., Bai, J., Chen, H., Hameed, W. B. r., Sim, L. W., Tint, M. T., Leutscher-Broekman, B., Chong, Y.-S., Gluckman, P. D. and Fortier, M. V. 2013. Prenatal maternal depression associates with microstructure of right amygdala in neonates at birth. *Biological psychiatry*, 74 (11): 837-844.

Sadrolhosseini, A. R., Abdul Rashid, S., Shafie, S. and Soleimani, H. 2019. Laser ablation synthesis of Ag nanoparticles in graphene quantum dots aqueous solution and optical properties of nanocomposite. *Applied Physics A*, 125 (2): 1-9.

Saeidi, M., Yourdkhani, A., Ebrahimi, S. A. S. and Poursalehi, R. 2020. Candle flame-treatment as an effective strategy to enhance the photoelectrochemical properties of Ti-doped hematite thin films. *Journal of Materials Chemistry C*, 8 (34): 11950-11961.

Safrany, S. T., Ingram, S. W., Cartwright, J. L., Falck, J., McLennan, A. G., Barnes, L. D. and Shears, S. B. 1999. The Diadenosine Hexaphosphate Hydrolases fromSchizosaccharomyces pombe and Saccharomyces cerevisiae Are Homologues of the Human Diphosphoinositol Polyphosphate Phosphohydrolase: OVERLAPPING SUBSTRATE SPECIFICITIES IN A MutT-TYPE PROTEIN. *Journal of Biological Chemistry*, 274 (31): 21735-21740.

Saha, S., Dey, B., Chakrabotry, S. and Choudhury, T. 2013. Development of reverse phase high performance liquid chromatographic method and method validation of paracetamol by using economical single mobile phase. *Journal of Applied Pharmaceutical Research*, 1 (1): 36-41.

Saiduzzaman, M. 2019. Synthesis and characterization of cerium doped copper oxide nanoparticles by solution combustion technique.

Santhoshkumar, T., Rahuman, A. A., Jayaseelan, C., Rajakumar, G., Marimuthu, S., Kirthi, A. V., Velayutham, K., Thomas, J., Venkatesan, J. and Kim, S.-K. 2014. Green synthesis of titanium dioxide nanoparticles using Psidium guajava extract and its antibacterial and antioxidant properties. *Asian Pacific journal of tropical medicine*, 7 (12): 968-976.

Saupe, A., Gordon, K. C. and Rades, T. 2006. Structural investigations on nanoemulsions, solid lipid nanoparticles and nanostructured lipid carriers by cryo-field emission scanning electron microscopy and Raman spectroscopy. *International journal of pharmaceutics*, 314 (1): 56-62.

Schoeman, C., Dlamini, M. and Okonkwo, O. 2017. The impact of a wastewater treatment works in Southern Gauteng, South Africa on efavirenz and nevirapine discharges into the aquatic environment. *Emerging Contaminants*, 3 (2): 95-106.

Scholz, F. 2015. Voltammetric techniques of analysis: the essentials. *ChemTexts*, 1 (4): 1-24.

Sethy, N. K., Arif, Z., Mishra, P. K. and Kumar, P. 2020. Green synthesis of TiO2 nanoparticles from Syzygium cumini extract for photo-catalytic removal of lead (Pb) in explosive industrial wastewater. *Green Processing and Synthesis*, 9 (1): 171-181.

Sharifi, E., Steinacker, R. and Saghafian, B. 2016. Assessment of GPM-IMERG and other precipitation products against gauge data under different topographic and climatic conditions in Iran: Preliminary results. *Remote Sensing*, 8 (2): 135.

Sharma, A., Sharma, S., Sharma, K., Chetri, S. P., Vashishtha, A., Singh, P., Kumar, R., Rathi, B. and Agrawal, V. 2016. Algae as crucial organisms in advancing nanotechnology: a systematic review. *Journal of applied phycology*, 28 (3): 1759-1774.

Sharma, B. and Sharma, A. 2022. Recent Advances in Gas Sensors for Device Applications. *Materials for Devices*: 71-104.

Sharma, D. and Hussain, C. M. 2020. Smart nanomaterials in pharmaceutical analysis. *Arabian Journal of Chemistry*, 13 (1): 3319-3343.

Sharma, D., Kanchi, S. and Bisetty, K. 2019. Biogenic synthesis of nanoparticles: A review. *Arabian Journal of Chemistry*, 12 (8): 3576-3600.

Shen, Y., Yang, X., Wang, Y., Zhang, Y., Zhu, H., Gao, L. and Jia, M. 2008. The states of gold species in CeO2 supported gold catalyst for formaldehyde oxidation. *Applied Catalysis B: Environmental*, 79 (2): 142-148

Shende, S. S., RAJPUT, V. D., GOROVTSOV, A. V., MINKINA, T. M. and SUSHKOVA, S. N. 2021. *Microbial Synthesis of Nanomaterials*. Nova Science Publishers.

Sheng, Z.-H., Zheng, X.-Q., Xu, J.-Y., Bao, W.-J., Wang, F.-B. and Xia, X.-H. 2012. Electrochemical sensor based on nitrogen doped graphene: simultaneous determination of ascorbic acid, dopamine and uric acid. *Biosensors and Bioelectronics*, 34 (1): 125-131.

Shervedani, R. K. and Lasia, A. 1999. Evaluation of the surface roughness of microporous Ni–Zn–P electrodes by in situ methods. *Journal of applied electrochemistry*, 29 (8): 979-986.

Shetti, N. P., Bukkitgar, S. D., Reddy, K. R., Reddy, C. V. and Aminabhavi, T. M. 2019a. ZnO-based nanostructured electrodes for electrochemical sensors and biosensors in biomedical applications. *Biosensors and Bioelectronics*, 141: 111417.

Shetti, N. P., Nayak, D. S., Malode, S. J. and Kulkarni, R. M. 2018. Fabrication of MWCNTs and Ru doped TiO2 nanoparticles composite carbon sensor for biomedical application. *ECS Journal of Solid State Science and Technology*, 7 (7): Q3070.

Shetti, N. P., Nayak, D. S., Reddy, K. R. and Aminabhvi, T. M. 2019b. Graphene–clay-based hybrid nanostructures for electrochemical sensors and biosensors. In: *Graphene-Based Electrochemical Sensors for Biomolecules*. Elsevier, 235-274.

Shown, I., Ujihara, M. and Imae, T. 2010. Sensitizing of pyrene fluorescence by β-cyclodextrin-modified TiO2 nanoparticles. *Journal of colloid and interface science*, 352 (2): 232-237.

Siddiquah, A., Hashmi, S. S., Mushtaq, S., Renouard, S., Blondeau, J. P., Abbasi, R., Hano, C. and Abbasi, B. H. 2018. Exploiting in vitro potential and characterization of surface modified Zinc oxide nanoparticles of Isodon rugosus extract: Their clinical potential towards HepG2 cell line and human pathogenic bacteria. *EXCLI journal*, 17: 671.

Simon, N., Guichard, N., Odou, P., Decaudin, B., Bonnabry, P. and Fleury-Souverain, S. 2020. Efficiency of four solutions in removing 23 conventional antineoplastic drugs from contaminated surfaces. *Plos one*, 15 (6): e0235131.

Singh, R. K., Kunimatsu, K., Miyatake, K. and Tsuneda, T. 2016. Experimental and theoretical infrared spectroscopic study on hydrated Nafion membrane. *Macromolecules*, 49 (17): 6621-6629.

Singh, S., Kumar, N., Kumar, M., Agarwal, A. and Mizaikoff, B. 2017. Electrochemical sensing and remediation of 4-nitrophenol using bio-synthesized copper oxide nanoparticles. *Chemical engineering journal*, 313: 283-292.

Slabiak, O. 2016. Development and validation of UV-spectrophotometric methods of efavirenz quan-titative determination in urine.

Slabiak, O. I., Ivanchuk, I. M., Tokaryk, G. V., Klimenko, L. and Kolisnyk, I. S. 2018. Development and validation of UV-spectrophotometric procedures for efavirenz quantitative determination. *International Journal of Pharmaceutical Quality Assurance*, 9 (3): 231-240.

Sommer, L. 2012. *Analytical absorption spectrophotometry in the visible and ultraviolet: the principles*. Elsevier.

Sorbiun, M., Shayegan Mehr, E., Ramazani, A. and Taghavi Fardood, S. 2018. Green synthesis of zinc oxide and copper oxide nanoparticles using aqueous extract of oak fruit hull (jaft) and comparing their photocatalytic degradation of basic violet 3. *International Journal of Environmental Research*, 12 (1): 29-37.

Sousa, S. F., Fernandes, P. A. and Ramos, M. J. 2007. General performance of density functionals. *The Journal of Physical Chemistry A*, 111 (42): 10439-10452.

Srivastava, P., Moorthy, G. S., Gross, R. and Barrett, J. S. 2013. A Sensitive and Selective Liquid Chromatography/Tandem Mass Spectrometry Method for Quantitative Analysis of Efavirenz in Human Plasma. *PLOS ONE*, 8 (6): e63305.

Stankic, S., Suman, S., Haque, F. and Vidic, J. 2016. Pure and multi metal oxide nanoparticles: synthesis, antibacterial and cytotoxic properties. *Journal of nanobiotechnology*, 14 (1): 1-20.

Sundrarajan, M. and Gowri, S. 2011. Green synthesis of titanium dioxide nanoparticles by Nyctanthes arbor-tristis leaves extract. *Chalcogenide Lett*, 8 (8): 447-451.

Swathi, N., Sandhiya, D., Rajeshkumar, S. and Lakshmi, T. 2019. Green synthesis of titanium dioxide nanoparticles using Cassia fistula and its antibacterial activity. *Int. J. Res. Pharm. Sci*, 10 (2): 856-860.

Tamilselvi, N., Arivukkarasu, R., Sasikala, R. and Jayan, S. 2018. Development and Validation of HPTLC method for the Determination of Efavirenz in Tablet Dosage Form. *Research Journal of Pharmacy and Technology*, 11 (3): 885-888.

Tang, Z., Hull, C. E. and Rothenberg, S. 2012. How corporate social responsibility engagement strategy moderates the CSR–financial performance relationship. *Journal of management Studies*, 49 (7): 1274-1303.

Tarahomi, S., Rounaghi, G. H., Zavar, M. H. A. and Daneshvar, L. 2018. Electrochemical sensor based on TiO2 nanoparticles/nafion biocompatible film modified glassy carbon electrode for carbamazepine determination in pharmaceutical and urine samples. *Journal of The Electrochemical Society*, 165 (16): B946.

Thakkar, K. N., Mhatre, S. S. and Parikh, R. Y. 2010. Biological synthesis of metallic nanoparticles. *Nanomedicine: nanotechnology, biology and medicine*, 6 (2): 257-262.

Thakur, B., Kumar, A. and Kumar, D. 2019. Green synthesis of titanium dioxide nanoparticles using Azadirachta indica leaf extract and evaluation of their antibacterial activity. *South African Journal of Botany*, 124: 223-227.

Thapliyal, N., Osman, N. S., Patel, H., Karpoormath, R., Goyal, R. N., Moyo, T. and Patel, R. 2015. NiO–ZrO 2 nanocomposite modified electrode for the sensitive and selective determination of efavirenz, an anti-HIV drug. *RSC Advances*, 5 (50): 40057-40064.

Theophanides, T. 2012. Introduction to infrared spectroscopy. *Infrared Spectroscopy-Materials Science, Engineering and Technology*: 1-10.

Tittikpina, N. K., Wane, T. M., Diouf, D., Thiam, K., Diop, A., Fall, D., Diop, Y. M. and Sarr, S. O. 2020. Development and validation of a UV-Visible method for the determination of the active principle Efavirenz in tablets. *International Journal of Biological and Chemical Sciences*, 14 (1): 279-288.

Torabi, M., Shervedani, R. K. and Amini, A. 2021. Highly controlled synthesis of nanoprickly nickel@ nickel oxide formed on carbon black/reduced graphene oxide nanosheets: Charge-storage performance and electrocatalytic activity for methanol oxidation. *Journal of Alloys and Compounds*, 886: 161236.

Tosin, A. B., Slabiak, O., Ivanchuk, I. and Mykytenko, O. Y. 2016. Development of UV-spectrophotometric methods of efavirenz determination.

Tripathi, G. K. 2019. Engineered Nanomaterials and TheirProperties: A Review. *Biosci. Biotech. Res. Comm*, 12: 764-771.

Turneaure, J., Everitt, C., Parkinson, B., Bardas, D., Buchman, S., DeBra, D., Dougherty, H., Gill, D., Grammer, J. and Green, G. 2003. Development of the Gravity Probe B flight mission. *Advances in Space Research*, 32 (7): 1387-1396.

Tyagi, S., Chaudhary, M., Ambedkar, A. K., Sharma, K., Gautam, Y. K. and Singh, B. P. 2022. Metal Oxide Nanomaterials based sensors for monitoring environmental NO2 and its impact on plant ecosystem: A Review. *Sensors & Diagnostics*,

Uwaya, G. E., Wen, Y. and Bisetty, K. 2022. A combined experimental-computational approach for electrocatalytic detection of epinephrine using nanocomposite sensor based on polyaniline/nickel oxide. *Journal of Electroanalytical Chemistry*: 116204.

van de Werken, M., Booij, S. H., van der Zwan, J. E., Simons, M. J., Gordijn, M. C. and Beersma, D. G. 2014. The biological clock modulates the human cortisol response in a multiplicative fashion. *Chronobiology international*, 31 (4): 572-580.

Vasudev, H., Thakur, L. and Bansal, A. 2016. A review on performance of glass mould coated with different coating techniques. In: Proceedings of *Proceedings of 4th International Conference on Production and Industrial Engineering*. 12.

Venkateshaiah, A., Padil, V. V., Nagalakshmaiah, M., Waclawek, S., Černík, M. and Varma, R. S. 2020. Microscopic techniques for the analysis of micro and nanostructures of biopolymers and their derivatives. *Polymers*, 12 (3): 512.

Verma, S. K., Nandi, A., Sinha, A., Patel, P., Jha, E., Mohanty, S., Panda, P. K., Ahuja, R., Mishra, Y. K. and Suar, M. 2021. Zebrafish (Danio rerio) as an ecotoxicological model for Nanomaterial induced toxicity profiling. *Precis. Nanomed.*, 4 (1): 750-781.

Verma, V., Al-Dossari, M., Singh, J., Rawat, M., Kordy, M. G. and Shaban, M. 2022. A Review on Green Synthesis of TiO2 NPs: Photocatalysis and Antimicrobial Applications. *Polymers*, 14 (7): 1444.

Vijayaraghavan, K. and Ashokkumar, T. 2017. Plant-mediated biosynthesis of metallic nanoparticles: a review of literature, factors affecting synthesis, characterization techniques and applications. *Journal of environmental chemical engineering*, 5 (5): 4866-4883.

Vilasó-Cadre, J. E., Arada-Pérez, M. d. l. Á., Arce-Castro, J. and Baeza-Reyes, D. C. 2020. Study of the potential sweeps in the manual staircase voltammetry. *Revista Cubana de Química*, 32 (2): 287-298.

Wang, S. Y. and Jiao, H. 2000. Scavenging capacity of berry crops on superoxide radicals, hydrogen peroxide, hydroxyl radicals, and singlet oxygen. *Journal of agricultural and food chemistry*, 48 (11): 5677-5684.

Wang, Z. and Dai, Z. 2015. Carbon nanomaterial-based electrochemical biosensors: an overview. *Nanoscale*, 7 (15): 6420-6431.

Wu, K.-W., Sweeney, C., Dudhipala, N., Lakhani, P., Chaurasiya, N. D., Tekwani, B. L. and Majumdar, S. 2021. Primaquine loaded solid lipid nanoparticles (SLN), nanostructured lipid carriers (NLC), and nanoemulsion (NE): effect of lipid matrix and surfactant on drug entrapment, in vitro release, and ex vivo hemolysis. *AAPS PharmSciTech*, 22 (7): 1-12.

Wu, S., He, Q., Tan, C., Wang, Y. and Zhang, H. 2013. Graphene-based electrochemical sensors. *small*, 9 (8): 1160-1172.

Wu, Y., Pang, H., Liu, Y., Wang, X., Yu, S., Fu, D., Chen, J. and Wang, X. 2019. Environmental remediation of heavy metal ions by novel-nanomaterials: a review. *Environmental pollution*, 246: 608-620.

Xu, D., Li, L., He, R., Qi, L., Zhang, L. and Cheng, B. 2018a. Noble metal-free RGO/TiO2 composite nanofiber with enhanced photocatalytic H2-production performance. *Applied Surface Science*, 434: 620-625.

Xu, H., Li, L., Fan, G. and Chu, X. 2018b. DFT study of nanotubes as the drug delivery vehicles of Efavirenz. *Computational and Theoretical Chemistry*, 1131: 57-68.

Xu, X. 2021. Intelligent composite materials for use as sensors and actuators. In: *Composite Materials*. Elsevier, 465-487.

Yadav, A., Mandal, M. K. and Dubey, K. K. 2020. Nanomaterial Biosynthesis and Enzyme Immobilization: Methods and Applications. *Green Synthesis of Nanomaterials for Bioenergy Applications*: 191-209.

Yadav, T. P., Yadav, R. M. and Singh, D. P. 2012. Mechanical milling: a top down approach for the synthesis of nanomaterials and nanocomposites. *Nanoscience and Nanotechnology*, 2 (3): 22-48.

Yanenko, O., Shevchenko, K. and Golovchanska, O. 2018. Modulation optical radiometry in medical and biological research. *Вісник Київського політехнічного інституту. Серія Приладобудування*, (55 (1)): 125-133.

Yang, J., Hou, B., Wang, J., Tian, B., Bi, J., Wang, N., Li, X. and Huang, X. 2019a. Nanomaterials for the removal of heavy metals from wastewater. *Nanomaterials*, 9 (3): 424.

Yang, M., Wang, Y., Dong, L., Xu, Z., Liu, Y., Hu, N., Kong, E. S.-W., Zhao, J. and Peng, C. 2019b. Gas sensors based on chemically reduced holey graphene oxide thin films. *Nanoscale research letters*, 14 (1): 1-8.

Yang, W. 1991. Direct calculation of electron density in density-functional theory. *Physical review letters*, 66 (11): 1438.

Yusoff, N., Pandikumar, A., Huang, N. M. and Lim, H. N. 2015a. Facile synthesis of nanosized graphene/Nafion hybrid materials and their application in electrochemical sensing of nitric oxide. *Analytical Methods*, 7 (8): 3537-3544.

Yusoff, N., Pandikumar, A., Marlinda, A., Huang, N. and Lim, H. 2015b. Nanosized graphene/Nafion hybrid modified electrode for electrochemical detection of dopamine. *Science of Advanced Materials*, 7 (12): 2692-2703.

Zaleska-Medynska, A. 2018. *Metal oxide-based photocatalysis: fundamentals and prospects for application*. Elsevier.

Zanolli Filho, L. A., Galdez, C. R., Silva, C. A., Tavares, M. F., Costa, D. M. and Aurora-Prado, M. S. 2011. Development and validation of a simple and rapid capillary zone electrophoresis method for determination of nnrti nevirapine in pharmaceutical formulations. *Journal of the Brazilian Chemical Society*, 22 (10): 2005-2012.

Zaporotskova, I. V., Boroznina, N. P., Parkhomenko, Y. N. and Kozhitov, L. V. 2016. Carbon nanotubes: Sensor properties. A review. *Modern Electronic Materials*, 2 (4): 95-105.

Zappa, D., Bertuna, A., Comini, E., Kaur, N., Poli, N., Sberveglieri, V. and Sberveglieri, G. 2017. Metal oxide nanostructures: preparation, characterization and functional applications as chemical sensors. *Beilstein journal of nanotechnology*, 8 (1): 1205-1217.

Zhang, F., Liu, J., Ivanov, I., Hatzell, M. C., Yang, W., Ahn, Y. and Logan, B. E. 2014. Reference and counter electrode positions affect electrochemical characterization of bioanodes in different bioelectrochemical systems. *Biotechnology and bioengineering*, 111 (10): 1931-1939.

Zhang, Y.-f., Lin, W., Li, Y., Ding, K.-n. and Li, J.-q. 2005. A Theoretical Study on the Electronic Structures of TiO2: Effect of Hartree− Fock Exchange. *The Journal of Physical Chemistry B*, 109 (41): 19270-19277.

Zhao, X., Guo, H., Xue, R., Wang, M., Guan, Q., Fan, T., Yang, W. and Yang, W. 2021. Electrochemical sensing and simultaneous determination of guanine and adenine based on covalent organic frameworks/NH2-rG/MoS2 modified glassy carbon electrode. *Microchemical Journal*, 160: 105759.

Zhu, Y., Liu, X., Hu, Y., Wang, R., Chen, M., Wu, J., Wang, Y., Kang, S., Sun, Y. and Zhu, M. 2019. Behavior, remediation effect and toxicity of nanomaterials in water environments. *Environmental research*, 174: 54-60.